Active Nanophotonics

for Quantum- and Classical-Optics Applications

by

Lei Zhu

Presented to the Faculty of the Graduate School of

The University of Texas at Arlington in Partial Fulfillment

of the Requirements

for the Degree of

DOCTOR OF PHILOSOPHY

THE UNIVERSITY OF TEXAS AT ARLINGTON

August 2012

ACKNOWLEDGEMENTS

First of all, I would like to thank my advisor Dr. Michael Vasilyev, who provided me the opportunity to work in his outstanding group and also encouraged and challenged me throughout my academic program. In 2008, I joined his group. Before I do not have much background in electrical engineer, he patiently brought me to this exciting research field. After every discussion I did with Dr. Vasilyev, I was impressed by his deep understanding and vision about our research field-nanophotonics. Doing things is important and the ways to do thing are even more important. As a supervisor, he will not only ask me to finish some projects, but also inspire me how to think. Financially, Dr. Vasilyev supported my study through the Ph.D. student's days. Also He supported me to attend several academic conferences to present my research results. Dr. Vasilyev is the best supervisor who I can expect.

I would like to thank Dr. Nikolai Stelmakh, who was my co-advisor. He is more than an advisor, also a friend and life mentor for me.

During my Ph.D. study, my family gave me a lot of supports financially and mentally. Life is not always easy. When my project did not go smooth and I felt frustrated, they always gave me support to help to go through the hard time. Here my special thanks go to my grandmother. I believe you are so happy to see your grandson get the Ph.D. degree wherever you are. I miss you!

I also would like to thank my committee members: Prof. Jung-Chih Chiao, Prof. Zeynep Celik-Butler, Prof. Seong Jin Koh, Prof. Robert Magnusson and Prof. Weidong Zhou. I really appreciate your help and good advices for my dissertation.

After I join this group, I really enjoyed the atmosphere and obtained a lot of helps from my lab mates: Muthiah Annamalai, Sarath Chandra. S, Li Lu, K. Young, Gokulkrishn Srinivasan, Pallavi, Steven. I would like to thank Muthiah Annamalai who helped me finish the simulation part of the project. Also I really enjoyed the conferences that we attended together. I want to thank Sarath Chandra who helped me finish the measurement of the project. We also spent a lot time together in the cleanroom and FIB room.

Friendship is so important for every human being. Here I want to thank all friends. No matter where you are, you gave me happiness and confidence to help finish my Ph.D.

Finally, I would like to thank Feiying Chen. I really appreciate your support and help.

July 16th 2012

ABSTRACT

Active Nanophotonics

for Quantum- and Classical-Optics Applications

Lei Zhu, PhD

The University of Texas at Arlington, 2012

Supervising Professor: Michael Vasilyev

This thesis presents theoretical and experimental development of the interaction enhancement between the photon and matter.

We propose one single photon emitter by integrating a single CdSe / ZnS quantum dot into a plasmonic nano-cavity. We experimentally observe directional spontaneous emission with angular half-width of about 10 degrees from a single CdSe/ZnS quantum dot positioned in a slit nanoaperture surrounded by periodic corrugations.

Aware of the intrinsic loss limitation of single-photon emitter based on plasmonic nano-cavity, we go on to exploit the relationship between the fluorescence decay times of CdSe/ZnS core-shell quantum dots and the refractive index of the surrounding medium. We report measurements of the fluorescence decay times of

CdSe/ZnS core-shell quantum dots at the air-dielectric interface for several dielectrics with different refractive indices. The results are in agreement with a simple theory that accounts for the impact of the refractive index on the density of states and magnitude of the vacuum field, as well as for the local-field correction inside the quantum dot. The results suggest that, by embedding the quantum dots into a high-index dielectric material, one can reduce the spontaneous decay time to sub-nanosecond scale while preserving high quantum efficiency.

In order to manipulate the nanoparticle, we propose and demonstrate plasmonic optical tweezers fabricated at the tip of a single mode optical fiber. We trap sub-micron-size particles in 3 dimensions by this simple tool.

TABLE OF CONTENTS

LIST OF ILLUSTRATIONS

Figure Page

LIST OF TABLES

CHAPTER 1

INTRODUCTION

Optics is an ancient yet full of vigor branch of physics. Back to 700 BC, people from ancient Egypt, Greece and Babylon have already tried to use polished crystal to make lenses to control the optical path of light. Coming to the Renaissance, optics also stepped into a rapid developing time. Geometrical optics has been built during this period. Following the “rebirth” of physics, optics also stepped into the new age – quantum optics in the beginning of twentieth century. From last decade in twentieth century until now, with the development of semiconductor industry and modern fabrication technology, quantum optics has become a subject with real applications in the world and a thriving field with ever broadening horizons.

Quantum optics considers light to be composed of particles (photons), and these particles also have wave behaviors. Each particle carries the energy equal to $h\upsilon$, where h is Planck's constant and υ is the frequency of the light. The word ‘photon’ was coined by Gilbert Lewis in 1926 [1]. Right now quantum information processing is the practical use of quantum optics. This subject includes three main sub-branches: Quantum cryptograph, Quantum computing and Quantum teleportation. In the 1980s, scientists have developed the fundamental concepts of quantum cryptography which is the use of quantum mechanical effects to perform cryptographic tasks or to break

cryptographic systems [2] and in 1992 C. H. Bennet first experimentally proved this principle [3]. The concept of quantum key distribution is the most important part of quantum cryptography, which forms the basis for secure data transmission. Quantum computing is to use the quantum mechanics to enhance the computational power of a computer. Quantum teleportation is to use the quantum mechanics to transfer the quantum state of one particle to another. Single photon emitter which is the source emits exactly one photon in response to a trigger pulse, is one of the most important tools for quantum information processing.

To date, single-photon sources are still notoriously difficult to make. The method to build it is either heavily attenuating a laser or exciting single atoms. The drawback is that these schemes are often too complex and do not produce one photon deterministically in every pulse. The source should consist of a single emissive species, e.g., atom, and an extra trigger pulse excites the electron of the emissive species to an upper excited state. After emitting a photon, the atom relaxes to the ground state. Single photon is an idea carrier for the quantum-information science. Photonic qubits, where information is encoded in the quantum state of the photon using polarization, momentum and energy, are an ideal choice for many applications, because photons travel at the speed of light and will not interact strongly with their environment over long distances, which results in lower noise and loss and photons can be manipulated with linear optics. Several systems have been investigated for single photon source. Currently the popular single photon systems are made by semiconductor quantum dots

[1-4], mesoscopic quantum wells [5], single molecules [6-8], single atoms [9], single ions [10] and color centers [11, 12]. An ideal single photon source would be: a single photon can be emitted at any arbitrary time defined by the user (i.e., the source is deterministic, or "on-demand"), the probability of emitting a single photon is 100%, the probability of multiple-photon emission is 0%, subsequent emitted photons are indistinguishable, and the repetition rate is arbitrarily fast (limited only by the temporal duration of the single-photon pulses, perhaps) [13]. Many benefits of quantum dot such as high quantum efficiency, environmental stability and easy integration into larger fabricated structures such as microcavities [14-16] make the Quantum dot one of the best candidates to make a single-photon emitter. Semiconductor quantum dot is usually referred as "artifact atom", which has a discrete energy structure for the electrons and holes [2-4, 17, 18]. In the weak excitation and coupling regime, an exciton (electron-hole pair) can be produced by a trigger pulse. The rate of spontaneous emission of a quantum dot can be significantly modified due to the Purcell effect [19], when the dot is placed into a resonant cavity. In order to control the spontaneous emission rate of a quantum dot, a lot of different microcavities have been made including these using distributed-Bragg-reflection (DBR) mirrors, micro-pillar, microdisk, microsphere, micro-toroid or photonic crystal cavities [3, 14, 20, 21-23].

The Purcell factor is proportional to the Q-factor of the cavity divided by the volume of the cavity. The above micro-cavities have volumes exceeding $(\lambda/n)^3$. Another drawback of these cavities is that it is very hard to control the emission direction of the

light that couples out of the cavity. Surface Plasmon (SP) is a surface electromagnetic wave propagating along the interface between any two materials where the real part of the dielectric function changes sign across the interface, and is generated by the coherent electron oscillations. Research on SPs has become a major part of the fascinating field of nanophotonics and is of interest to a wide spectrum of scientists, from physicistsm chemists and materials scientists to biologists. The two main ingredients of plasmonics – surface Plasmon polaritons and localized surface plasmons. These two concepts were clearly described as early as 1900. However, surface Plasmon polaritons have been rediscovered in a variety of different contexts at the end of 20th century. This “second birth” of SPs and recent rapid development of research in this area [24-26] occurred after scientists realized that SP modes in metallic nanostructures may lead to the localization of light signals far beyond the diffraction limit for electromagnetic wave in dielectric media. The limits of the SPs waves are only decided by the atomic structure of matter, dissipation and the spatial dispersion of light [27, 28]. Therefore, we can use this advantage of the surface plasmon to make an extremely small cavity. Another important application of SPs is plasmonic nano-antennas, which can provide efficient coupling between the localized and free-space propagating light modes [29]. In chapter 2 of this dissertation, we propose a surface plasmonic single photon emitter. A CdSe / ZnS semiconductor quantum dot has been integrated into surface-plasmonic nano-slit cavity, and then a surface-plasmonic nano-antenna has been fabricated on one end of the cavity [30, 31]. With this nano-structure, we can control

both the spontaneous emission rate and the far-field radiation pattern of the quantum dot.

However, everything has two sides. One of the drawbacks of this single photon emitter is low efficiency. Because of the surface plasmonic structure, a lot of loss of the radiation of the quantum dot is introduced. Hence, we re-study the microcavity-based single-photon sources; the emission rate increase originates from both resonant enhancement of the local density of states and from the dielectric properties of the material surrounding the quantum dot [32]. Thus, it is hard to separate and compare the impacts of these two contributions on the total emission rate. While the influence of the nearby metal on the quantum-dot emission has received a lot of attention recently [33, 34], the studies of the role of the surrounding dielectric in quantum-dot fluorescence have been rather limited. Damped-oscillator-like dependence of the fluorescence decay time on the distance between the quantum dot and silicon substrate was demonstrated in [35]. In [36], the reduction of the decay time on a glass surface compared to the decay time in free space was shown. The impact of the interaction within an ensemble of quantum dots on the emission spectra was studied in [37] for several surface types. In Chapter 3, we report measurements of the fluorescence decay times of CdSe / ZnS core-shell quantum dots at the air-dielectric interface for several dielectrics with different refractive indices [38]. The results are in agreement with a simple theory that accounts for the impact of the refractive index on the density of states and magnitude of the vacuum field, as well as for the local-field correction inside the quantum dot.

One important characteristics of single photon emitter is that only one photon is emitted, i.e., the probability of multiple-photon emission is 0%. To satisfy this rule, only one quantum dot should reside in the cavity. However, manipulating one quantum dot and placing it to one location within nanometer-scale accuracy are very challenging. Chapter 4 we introduces a new type optical tweezers based on optical fiber, which is very easy to operate.

The thesis focuses generally on the development of semiconductor quantum dot based single photon emitter and related work. It contains three parts. Chapter 2 proposes a single-photon emitter by integrating one CdSe / ZnS quantum dot into surface plasmonic cavity and demonstrates collimated spontaneous emission beam from such a cavity with plasmonic antenna. Chapter 3 introduces a simple theory that accounts for the impact of the refractive index on the density of states and magnitude of the vacuum field, as well as for the local-field correction inside the quantum dot, and reports measurements of the fluorescence decay times of CdSe/ZnS core-shell quantum dots at the air-dielectric interface for several dielectrics with different refractive indices that are in good agreement with the theoretical results. Chapter 4 descries a single mode fiber-based plasmonic optical tweezers and demonstrates optical trapping of micron- and sub-micron-sized particles. This optical tweezers is proposed to manipulate a single quantum dot. Chapter 5 summaries all the work and discusses the future research directions.

CHAPTER 2

SHAPING SPONTANEOUS EMISSION PATERN BY PLASMONIC NANOCAVITY

2.1 Quantum Optics

Quantum optics is the field of research in physics that deal with optical phenomena that can only be explained by treating light as a stream of photons rather than as electromagnetic waves.

2.1.1 History of Quantum Optics

In 1899, by assuming light radiation is quantized, Max Planck correctly modeled blackbody radiation. By doing this, he also solved the ultraviolet catastrophe problem that had been puzzling physicists for many years. Six years later in 1905, Einstein applied Planck's quantum theory to explain the photoelectric effect [39]. These pioneering ideas laid the foundations for the quantum theories of light and atoms, but in themselves did not give direct experimental evidence of the quantum nature of the light. In 1926, the word 'photon' was coined by Gilbert Lewis. [40] In the following years, although the understanding of the interaction between light and matter following these developments was crucial for the development of quantum mechanics as a whole, little effort was invested in looking for quantum effects directly associated with the light itself.

Until 1956, Hanbury Brown and Twiss brought people's attention back to quantum optics. Their experiments on correlations between the starlight intensities recorded on two separated detectors provoked a storm of controversy [41]. Their experiments have been considered a landmark in this field, because they opened the door to more sophisticated experiments on photon statistics that would eventually lead to the observation of optical phenomena with no classical explanation. In the year of 1960, there was one of the most important inventions in the history of optics – laser, which gave people a lot of hopes to this field. Glauber described new states of light which have different statistical properties from those of classical light in 1963 [42]. Fourteen years later, Kimble, Dagenais, and Mandel's experiment confirmed these non-classical properties and demonstrated photon antibunching for the first time [43]. In 1985, Slusher, Hollberg, Yurke, Mertz, and Valley observed squeezed states by four-wave mixing in an optical cavity [44].

In recent years, single-photon interference, Bell's inequality violation, quantum cryptography, quantum phase gate and Bose–Einstein condensation of atoms have been done [45-49].

2.1.2 What is Quantum Optics

So far, people divide optics into three distinct areas: Geometrical optics, Physical optics and Quantum optics. Geometrical optical is also called ray optics, which means the wavelength of the light can be neglected. Physical optics is the second stage of optics, which is based on the fact that light is an electromagnetic wave. The behavior of

light can be solved by Maxwell's equations for physical optics. In quantum optics, light is composed of particles (photon) and these particles also have wave behaviors. Each particle carries one quantum of energy equal to $h\upsilon$, where h is Planck's constant and υ is the frequency of the light. Statistical mechanics is the fundament of most concepts of quantum optics: light is described in terms of field operators for creation and annihilation of photons—i.e. in the language of quantum electrodynamics. Coherent state is frequently used to approximately describe the output of a single frequency laser above the laser threshold, and exhibits poissonian photon number statistics. By means of nonlinear optics, a coherent state can be transformed into a squeezed coherent state, which can exhibit super- or sub- Poissonean photon statistics. The interaction between light and atom is also an important part of quantum optics. In quantum optics, atom is considered as quantum mechanical system with a discrete energy spectrum with the transitions between the energy eigenstates being driven by the absorption or emission of light quanta. Quantum information processing is the potential application of quantum optics. This subject includes three main sub-branches: Quantum cryptograph, Quantum computing and Quantum teleportation. The fundamental concepts of quantum cryptography were developed in the 1980s [2] and the first experimental proof of principle was given in 1992 [3]. The concept of quantum key distribution is the most important part of quantum cryptography, which forms the basis for secure data transmission. Quantum computing uses the quantum mechanics to enhance the

computational power of a computer. Quantum teleportation uses the quantum mechanics to transfer the quantum state of one particle to another.

2.2 Single -Photon Emitter

A photon is an elementary excitation of a single mode of electromagnetic field [50]. The basic idea of the single-photon source is that the source should emit exactly one photon in response to a trigger pulse. The source should consist of a single emissive species – an atom and a trigger pulse excites the electron of the emissive species to an upper excited state. After emitting a photon, the atom relaxes to the ground state.

2.2.1 Motivation

A major driver of the research into single photon sources is the explosive growth of the field of quantum-information science [51, 52]. Quantum-information involves the encoding, communication, manipulation and measurement of information by using quantum objects. Photonic information is encoded in the quantum state of the photon using degrees of freedom such as polarization, momentum and energy, which are called “photonic qubits”. Since photons travel at the speed of light and interact weakly with their environment over long distances, which results in lower noise and loss and photons can be manipulated with linear optics, they are an ideal choice for many of these applications.

2.2.2 Characteristics of an ideal single-photon source

The ideal single-photon source [13] should be the one with high quantum efficiency – the source is "on demand", low noise – a single photon is 100% and the probability of multiple photon emission is 0%, and high speed – the repetition rate is arbitrarily fast. The quantum efficiency and speed of a single-photon emitter is not hard to check. The statistics of the single-photon sources can be characterized by the second-order correlation function [42, 53].

$$g^{(2)}(\vec{r}_{1,}\vec{r}_{2,}t_2 - t_1) = \frac{\langle : \hat{n}(\vec{r}_{1,}t_1)\hat{n}(\vec{r}_{2,}t_2) : \rangle}{\langle \hat{n}(\vec{r}_{1,}t_1)\rangle\langle \hat{n}(\vec{r}_{2,}t_2)\rangle} \tag{2.1}$$

Where $\hat{n}$ denotes the photon-number operators and :: denotes operator normal ordering. For an ideal single-photon emitter, the cross-correlation function for the two outputs of the beamsplitter is $g^{(2)}(0) = 0$ with $g^{(2)}(\tau) > g^{(2)}(0)$. Since after emission of a single photon, the emitter must be excited again before a second photon can be emitted; it can never emit two photons at the same time. The properties of the second-order correlation function are listed in table 2.1 [54].

Table 2.1 Properties of the second-order correlation function for classical light [54].

Light source	Property	Comment
All classical light	$g^{(2)}(0) \geq 1$	$g^{(2)}(0) = 1$ when power is constant
	$g^{(2)}(0) \geq g^{(2)}(\tau)$	
Perfectly coherent light	$g^{(2)}(\tau) = 1$	Applies for all τ
Gaussian chaotic light	$g^{(2)}(\tau) = 1 + \exp[-\pi(\tau/\tau_c)^2]$	τ_c = coherence time
Lorentzian chaotic light	$g^{(2)}(\tau) = 1 + \exp[-2\lvert\tau\rvert/\tau_0]$	τ_0 = lifetime

2.3 Quantum Dot

There are several systems that have been investigated as candidates for single photon source. Currently the popular single photon systems are made by semiconductor quantum dots [1-4], mesoscopic quantum wells [5], single molecules [6-8], single atoms [9], single ions [10] and color centers [11, 12]. Many the benefits of quantum dots, such as high quantum efficiency, environmental stability and easy integration into larger fabricated structures make a quantum dot one of the best candidates to make a single-photon emitter.

Quantum dots are tiny particles of a semiconductor material whose excitons are confined in all three spatial dimensions. They are created with methods such as molecular beam epitaxy, where the process of self-assembled (Stranski-Krastanov) growth forms tiny islands of smaller-band-gap semiconductor embedded in a larger-

band-gap semiconductor [55]. Chemical synthesis is another popular method to use to produce colloidal quantum dots for single-photon source applications [56].

The usefulness of quantum dots stems from the inherent properties of bulk semiconductor crystals. Direct gap semiconductors can absorb a photon to excite an electron promoted directly from the valence band into the conduction band. In this process, an electron-hole pair (excitons) is created in the material as shown in Fig. 2.1 (a) [57]. However, as the size of the structure becomes comparable to or even smaller than the natural length scale of the electron-hole pairs, the carriers are confined by the boundaries of the structure. This phenomenon which is called “quantum size effect”, leads to atomic optical behavior in nanocrystals as the bulk bands become quantized as shown in Fig. 2.1 (b).

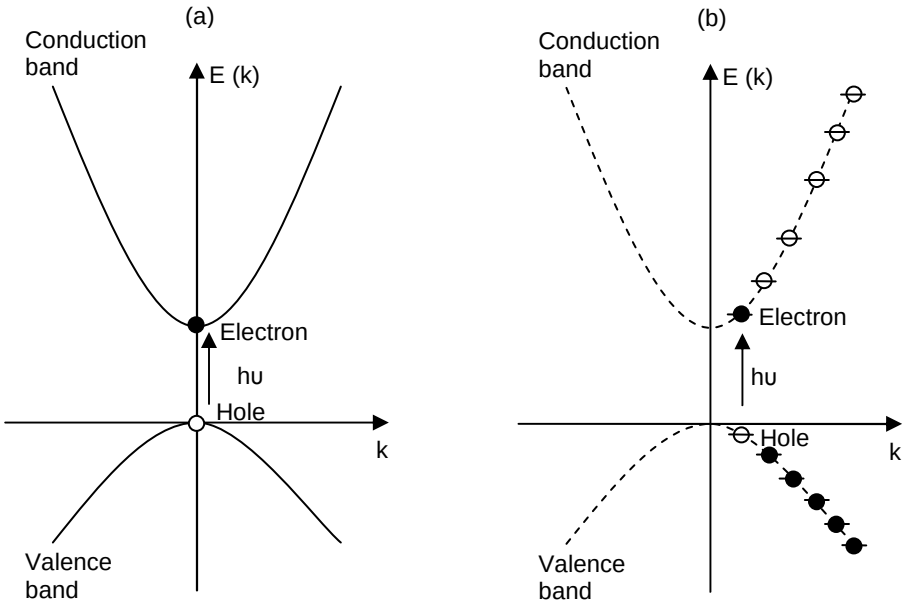

Figure 2.1. (a) Band diagram of a two band model for direct gap semiconductor. (b) Optical transitions in finite size semiconductor nanocrystals [57].

Colloidal quantum dots follow the same effect. The basic physics underlying it could be explained by locating photoexcited carriers in a three-dimensional potential well shown in Fig. 2.2 (b). The confinement causes the valence and conduction bands to be quantized into a ladder of hole and electron levels. Therefore the spectra from a quantum dot exhibit a series of discrete electronic transitions between these quantized levels. Sometimes, quantum dots are refereed to as “artificial atoms”.

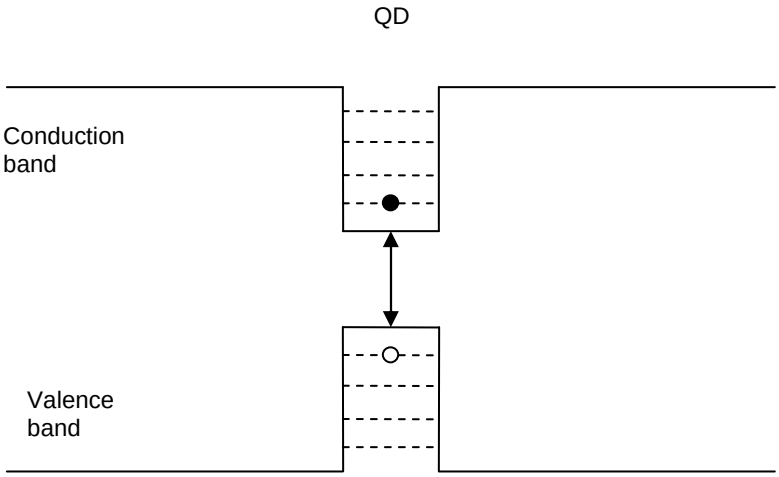

Figure 2.2. Potential well formed in the conduction and valence bands of a quantum dot.

Since the electron and hole energy levels are sensitive to the amount of confinement, the energy gap of excitons in QDs is strongly size dependent. The smaller QDs have stronger confinement making the energy gap larger. Similarly, a larger size gives a smaller energy gap. Hence, quantum dots made from the same material can achieve different emission colors by changing their size [58]. For larger (small) size quantum dots, the emission is more towards the red (blue). Colloidal QDs make it

possible to have the desired particle size which makes it easy to find QDs with the energy spectrum we need and high quantum efficiency even at room temperature. Currently, CdSe QDs with a ZnS shell (see Figure 2.3) are commonly used and studied. The Core/Shell structure diminishes chemical damage to the fluorescence core. ZnS is optically transparent to the emission range; therefore there are no photon losses for visible light emission due to the shell [58].

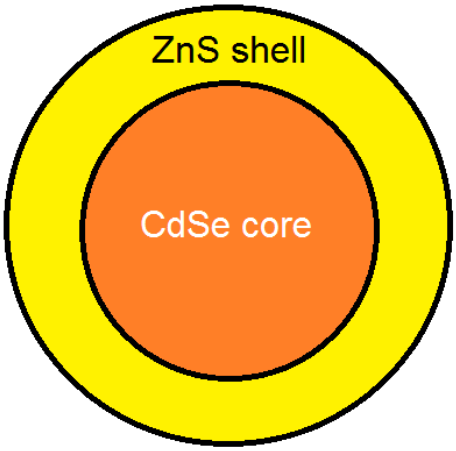

Figure 2.3. Core/Shell structure of CdSe/ZnS Quantum Dots.

2.4 Cavity Quantum Electrodynamics and Purcell Effect

2.4.1 Interaction between Light and Atoms in Free Space

First of all, let us take a look at the interaction between light and atoms. The quantum treatment of the interaction between light and atoms is usually developed in terms of the two-level atom approximation. The principle behind this phenomenon is depicted in Fig. 2.4. In Fig. 2.4 (a), it shows the absorption process. The atom is initially in the lower level, and a light beam of frequency υ is illuminated on the atom and

makes it jump to the excited state, at the same time a photon is absorbed from the light beam. Similarly, in the emission process shown in Fig. 2.4 (b), the atom is initially in the excited state. After a time (the radiative lifetime of the excited state), a photon of frequency υ is emitted. These two processes (absorption and emission) together are called a transition.

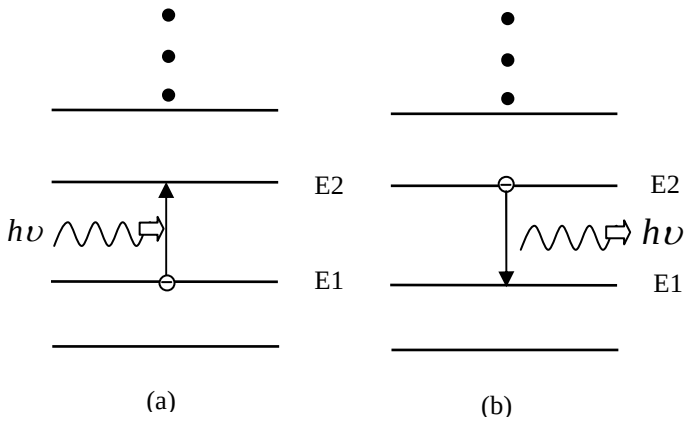

Figure 2.4. Optical transitions between the quantized energy levels: (a) absorption (b) spontaneous emission.

To understand the transition process, we need to start from Schrödinger equation:

$$\hat{H}\Psi = i\eta\frac{\partial\Psi}{\partial t} \quad , \tag{2.2}$$

$$\hat{H} = \hat{H}_0(r) + \hat{V}(t) \quad , \tag{2.3}$$

$$\hat{V}(t) = e\vec{r}\cdot\vec{\varepsilon}(t) \, , \tag{2.4}$$

Where $\hat{H}$ is the Hamiltonian operator, Ψ is the wave function of the quantum system, $\hat{V}(t)$ is potential energy, $\hat{H}_0(r)$ is the Hamiltonian operator in free space, $e\vec{r}$ is the dipole moment of the electron and $\vec{\mathcal{E}}(t)$ is the electrical field of the light.

$$\Psi(\vec{r},t) = c_1(t)\Psi_1(r)e^{-iE_1t/\eta} + c_2(t)\Psi_2(r)e^{-iE_2t/\eta} \tag{2.5}$$

where c_1 and c_2 are the wavefunction amplitude coefficients for the state 1 and state 2 of the atoms, E_1 and E_2 are the two energy levels. Suppose the polarization of the light is x-direction. Then from equation (2.4), we can get the perturbation matrix elements:

$$V_{12}(t) = \frac{e\mathcal{E}_0}{2}\left(e^{i\omega t} + e^{-i\omega t}\right)\langle 1|x|2\rangle \tag{2.6}$$

Now the dipole matrix element is given by:

$$\mu_{12} = -e\langle 2|x|1\rangle \tag{2.7}$$

Let us introduce a concept- Rabi frequency:

$$\Omega_R = |\mu_{12}\mathcal{E}_0/\eta| \tag{2.8}$$

Eventually, we obtain:

$$\dot{c}_1 = \frac{i}{2}\Omega_R(e^{i(\omega-\omega_0)t} + e^{-i(\omega+\omega_0)t})c_2(t) \quad , \tag{2.9}$$

$$\dot{c}_2 = \frac{i}{2}\Omega_R(e^{-i(\omega-\omega_0)t} + e^{i(\omega+\omega_0)t})c_1(t) \quad , \tag{2.10}$$

In order to understand the behavior of the atom interacting with the light, the two above equations need to be solved. To solve these two equations (2.9) and (2.10), we need to consider two cases (basically two different boundary conditions): weak field limit and strong field limit.

The weak field limit is for the low-power light source. In weak field limit, the atom is initially in the lower level and the electric field amplitude is small. Therefore, the perturbation is weak and the transitions number is small. We can get the boundary conditions for equations (2.9) and (2.10):

$$c_1^{(0)} = 1,\ \dot{c}_1^{(0)} = 0\ , \tag{2.11}$$

$$\dot{c}_2 = \frac{i}{2}\Omega_R (e^{-i(\omega-\omega_0)t} + e^{i(\omega+\omega_0)t})c_1 \tag{2.12}$$

We can finally obtain:

$$\left|c_2(t)\right|^2 = \frac{\pi}{\varepsilon_0 \eta^2}\mu_{12}^2 u(\omega_0)t \tag{2.13}$$

where $u(\omega_0)$ is the spectral energy density.

For the strong coupling, the intensity of the light source is strong and the population of the excited state is significant. If we now consider the case of exact resonance with $\delta\omega = 0$, then we can simplify equations (2.9) and (2.10):

$$\dot{c}_1 = \frac{i}{2}\Omega_R c_2(t) \tag{2.14}$$

$$\dot{c}_2 = \frac{i}{2}\Omega_R c_1(t) \tag{2.15}$$

Solving equations (2.14) and (2.15), we can obtain:

$$c_1(t) = \cos(\Omega_R t/2) \tag{2.16}$$

$$c_2(t) = \sin(\Omega_R t/2) \tag{2.17}$$

From equations (2.16) and (2.17), we can see the electrons oscillate back and forth between the two levels at the Rabi angular frequency. This oscillatory behavior in response to the strong-field is called Rabi oscillation or Rabi flopping.

2.4.2 Cavity Quantum Electrodynamics and Purcell Effect

In 2.4.1, we briefly introduce the interaction between photons and atom in free space. Now let us explore the special case - the interaction between photons and an atom inside a cavity, and then introduce Purcell effect.

There are a lot of different types of cavities. The simplest one consists of two plane mirrors. The fundamental principle behind these cavities is Fabry-Perot interference. Assume the reflectivities of the two mirrors are R_1 and R_2, no absorption or scattering losses, and then the transmission Γ is given by [54]:

$$\Gamma = \frac{1}{1+(4F^2/\pi^2)\sin^2(\varphi/2)}, \tag{2.18}$$

where

$$\varphi = \frac{4\pi n L_{cav}}{\lambda} \tag{2.19}$$

is the round-trip phase shift, and

$$F = \frac{\pi(R_1R_2)^{1/4}}{1-\sqrt{R_1R_2}} \tag{2.20}$$

is the finesse of the cavity.

For the quality of a cavity, the quality factor (Q factor) is very important to know. Before we come to the Q factor, we need to consider the photon lifetime. For a

light source at the center of a symmetric and high finesse cavity with $R_1 = R_2 = R \approx 1$, the photon lifetime:

$$\tau_{cav} = \frac{nL_{cav}}{c(1-R)} \tag{2.21}$$

The photon decay rate:

$$\kappa = 1/\tau_{cav} \tag{2.22}$$

The quality factor of the cavity is:

$$Q = \frac{\omega}{\Delta\omega} \tag{2.23}$$

where ω is the angular frequency of the light and $\Delta\omega$ is the resonant mode width in the cavity.

Now, we know the properties of the cavity and the transition process of an atom in free space. Next step is about analyzing: what will happen if an atom is inside a cavity? At resonance, the strength of the atom-cavity interaction is determined by three parameters:

1) the photon decay rate of the cavity κ
2) the free-space atom decay rate γ
3) the coupling parameter g_0

The electric dipole interaction energy is given by:

$$\Delta E = \left|\mu_{12}\varepsilon_{vac}\right| \tag{2.24}$$

The coupling parameter g_0:

$$g_0 = \left(\frac{\mu_{12}^2 \omega}{2\varepsilon_0 \eta V_0} \right)^{1/2} \tag{2.25}$$

where V_0 is the volume of the cavity.

From equation (2.25), we can understand that the coupling parameter is determined by the dipole moment, the angular frequency and the volume. The same as the coupling between the atom in free space and the light, the coupling strength between the atom and the cavity can be classified as either strong or weak. Single-photon emitter can be classified as weak coupling. In this chapter, we only introduce a single photon emitter, so we only describe the weak coupling here.

Weak coupling happens if the coupling parameter g_0 is smaller than the loss rate, which means the photons are lost from the cavity faster than the interaction time between the atom and the cavity. The most important effect that the cavity imposes on the atom is the change of the spontaneous emission rate of the atom. From the Fermi's golden rule, we obtain the transition rate for spontaneous emission:

$$W = \frac{2\pi}{\eta^2} |M_{12}|^2 g(\omega) \tag{2.26}$$

where $g(\omega)$ is the density of states:

$$g(\omega) = \frac{\omega^2 V_0}{\pi^2 c^3} \tag{2.27}$$

M_{12} is the matrix element of the electric dipole interaction between the state 1 and 2:

$$M_{12} = \frac{\mu_{12} \eta \omega}{6\varepsilon_0 V_0} \tag{2.28}$$

From equation (2.26), we can obtain that the spontaneous emission rate is dependent on the density of states $g(\omega)$ and electric dipole interaction M_{12}. From the normalized Lorentzian function, we can know:

$$g(\omega_0) = \frac{2}{\pi\Delta\omega_c} \frac{\Delta\omega_c^2}{4(\omega_0 - \omega_c)^2 + \Delta\omega_c^2} \tag{2.29}$$

where ω is the angular frequency of the atom transition, and w_c is the resonance frequency of the cavity.

When $\omega_0 = \omega_c$:

$$g(\omega_0) = \frac{2}{\pi\Delta\omega_c} = \frac{2Q}{\pi\omega_0} \tag{2.30}$$

We now introduce one of the most important concepts for single photon emitter - the Purcell factor F_P which is defined by:

$$F_P = \frac{W^{cav}}{W^{free}} \tag{2.31}$$

By putting equation (2.27), (2.28), and (2.30) into the Purcell factor (2.31), we obtain:

$$F_P = \frac{3Q(\lambda/n)^3}{4\pi^2 V_0} \tag{2.32}$$

From the Purcell factor (equation (2.32)); we can get the spontaneous emission rate which can be modified by the Q factor of the cavity and the volume of the cavity. If the F_P is greater than one, the spontaneous emission rate is increased. Therefore to increase the speed of the single photon emitter, we need to increase the Q factor of the cavity and

reduce the volume of the cavity. Another parameter effect which affects the Purcell factor is the dipole moment orientation of the atom. Here we will not discuss about it.

2.5 Surface Plasmonics

The single-photon emitter described in this chapter is made of metallic nano-cavity and utilizes surface plasmons for coupling to free space via plasmonic nano-antenna. Therefore it is necessary for us to introduce a phenomenon – surface plasmon. Surface Plasmon is a surface electromagnetic wave propagating along the interface between any two materials where the real part of the dielectric function changes sign across the interface, and is generated by the coherent electron oscillations. Recently, surface plasmons (SPs) have become as a major part of the fascinating field of nanophotonics and are of interest to a wide spectrum of scientists, from physicists, chemists and materials scientists to biologists.

The two main ingredients of plasmonics – surface plasmon polaritons and localized surface plasmons were clearly described as early as 1900. However, surface plasmon polaritons have been rediscovered in a variety of different contexts at the end of 20th century. This “second birth” of SPs and recent rapid development of research in this area [24-26] occurred after scientists realized that SP modes in metallic nanostructures may lead to the localization of light signals far beyond the diffraction limit for an electromagnetic wave in dielectric media. The limits of the SPs waves are only decided by the atomic structure of matter, dissipation and the spatial dispersion of light [27, 28].

Before we discuss SPs, it is necessary to introduce the evanescent wave. Let us consider the phenomenon of total internal reflection. An electromagnetic plane wave that propagates in a medium with refractive index *n* can be described by an electric field *E*:

$$E = E_0 \exp(i\omega i - ik_x x - ik_y y - ik_z z) \tag{2.33}$$

where E_0 is the amplitude of the electric field, ω is the angular frequency, k_x, k_y, and k_z are the wavevector components in *x*, *y* and *z* directions.

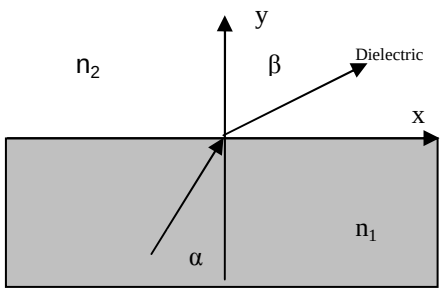

Figure 2.5. Refraction of light at an interface of two materials.

When the electromagnetic plane wave reaches the interface between two media 1 and 2 with refractive indices n_1 and n_2, respectively (Fig. 2.5), we know relationship between n_1 and n_2 from the Snell's law:

$$n_1 \sin\alpha = n_2 \sin\beta \tag{2.34}$$

$$k_{x1} = k_{x2} = k_x \tag{2.35}$$

To calculate k_{y2}, we obtain:

$$k_{y2}^2 = n_1^2 \left(\frac{2\pi}{\lambda}\right)^2 \left(\frac{n_2^2}{n_1^2} - \sin^2\alpha\right) \tag{2.36}$$

When the incidental angle α is greater than the total internal refection angle ($\sin\alpha > n_2 / n_1$), the right part of eq. (2.36) is negative and k_{y2} is imaginary. In this case, the traveling wave in medium 2 is parallel to the interface:

$$E_2 = E_0 \exp(-k_{y2} y)\exp(\mathrm{i}\omega t - \mathrm{i}k_x x) \tag{2.37}$$

From equation (2.37), we can find the amplitude of the electric field exponentially decaying along the y-direction, which the wave propagates along the interface of the two media. This field is denoted as the evanescent field. Surface plasmon is one kind of evanescent field. Now let us take a look at the dispersion relation for the surface plamson. By solving Maxwell's equations for the electromagnetic wave at an interface between two materials with relative dielectric functions ε_1 and ε_2 with the appropriate continuity relation, the boundary conditions are:

$$\frac{k_{y1}}{\varepsilon_1} + \frac{k_{y2}}{\varepsilon_2} = 0 \tag{2.38}$$

And

$$k_x^2 + k_{yi}^2 = \varepsilon_i \left(\frac{\omega}{c}\right)^2 \quad i = 1,2 \tag{2.39}$$

From equations (2.38) and (2.39), we can obtain the dispersion relation for a wave propagating on the surface:

$$k_x = \frac{\omega}{c}\left(\frac{\varepsilon_1 \varepsilon_2}{\varepsilon_1 + \varepsilon_2}\right)^{1/2} \tag{2.40}$$

and

$$k_{yi} = \frac{\omega}{c}\left(\frac{\varepsilon_i^2}{\varepsilon_1 + \varepsilon_2}\right)^{1/2} \quad i = 1,2 \tag{2.41}$$

In the free-electron mode of a metal, the metallic dielectric function is [59]:

$$\varepsilon(\omega) = 1 - \frac{\omega_p^2}{\omega^2} \quad , \tag{2.42}$$

where $\omega_p = \frac{ne^2}{\varepsilon_0 m}$ is the plasmon frequency of the free electron gas. In more sophisticated Drude mode, the dielectric function of the free electron gas:

$$\varepsilon(\omega) = 1 - \frac{\omega_p^2}{\omega^2 + i\gamma\omega} \tag{2.43}$$

where γ is the damping of the conduction electron oscillation.

Combining equation (2.40) and (2.43) and ignoring the damping of the conduction electron oscillation γ, the wave vector k_x goes to infinity as the frequency approaches the surface plasmon frequency:

$$\omega_{sp} = \frac{\omega_p}{\sqrt{1+\varepsilon_2}} \tag{2.44}$$

If the ε_2 =1, then from equation (2.40) and (2.44), we get surface-plasmon polariton dispersion curve compared to the light line shown in red in Fig 2.6 [60].

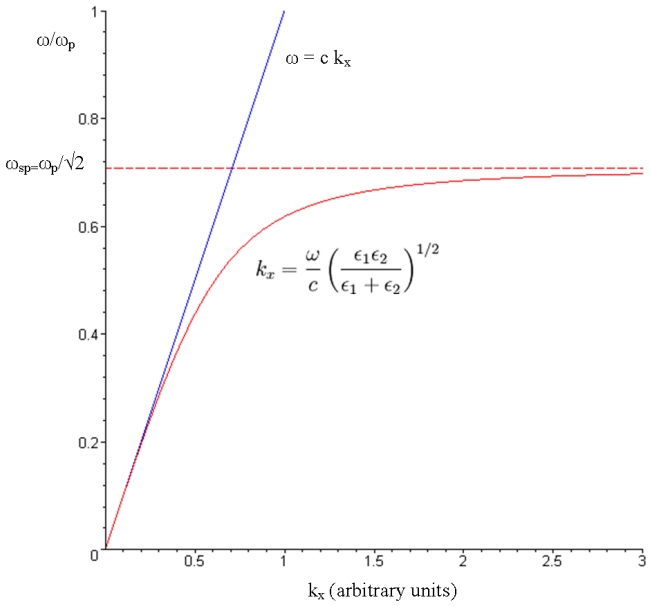

Figure 2.6. Surface-plasmon polariton dispersion curve [60]

From Fig. 2.6, we can find that the dispersion curve for light (blue line) has no point of intersection with the red curve apart from the origin. This implies that in this geometry "normal" light can not generate a surface plasmon directly. For the single angular frequency, the corresponding wavevectors are too much different. To solve this momentum mismatching problem, we can use evanescent coupling of light from a medium with higher dielectric index. Another way is use a metal layer on which a periodic structure is prepared as illustrated in Fig. 2.7. When light with $k = 2\pi/\lambda \cdot n\sin\theta$ falls on a diffraction grating structure, diffraction orders m is generated [61]. The net parallel wavevector can be written as:

$$k_{\parallel,net} = k_{\parallel} + m\frac{2\pi}{\Lambda} \qquad (2.45)$$

where Λ is the periods of the grating. From Eq. (2.45), we see that the grating structure adds a momentum to the incidental light. When net parallel momentum is equal to the momentum of the surface plasmon, the SPs will be generated.

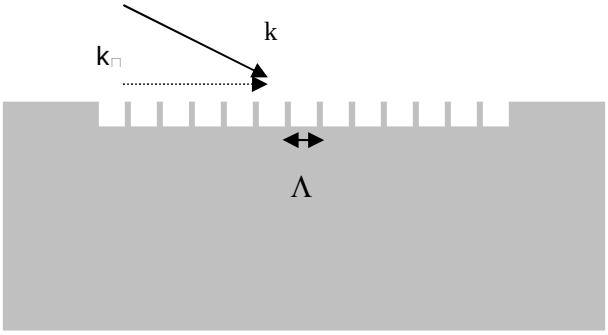

Figure 2.7 Schematic view of a grating couple

As we know, one of the main benefits of surface plasmon is to channel light efficiently into nanometer scale volumes. Various types of metallic nanostructures have been proposed for guiding SP modes including thick metal films [62,63], chains of metal nanoparticles [64, 65], cylindrical metal nanorods and nanoholes [66], nanogaps between metallic media [67-69], slot waveguides [70-71], sharp metal wedges [72-76], nanogrooves in metal substrates [75-82], and hybrid plasmonic waveguides [83]. All of these SPs modes can be used for achieving subwavelength localization of the guided signals. Subwavelength plasmonic structures can also concentrate light energy into nanoscale regions as small as a few nanometers [62, 83-85]. Finally, a plasmonic nano-antenna can use to couple SPs to free-space light modes [29]. For the plasmonic

circuits, active nanoplasmonics is also one important part, which can generate, modulate the field phase or amplitude, and detect output radiation without converting SPs modes to free space. In our single photon emitter device, we used the plasmonic nanoguiding and nano-antenna functions which can convert 2π wide quantum dot emission pattern into a collimated beam.

2.6 Sample Design

By using surface plasmon, light can be coupled to an extremely small volume. With the decreasing of the volume of the cavity, the spontaneous emission rate of the atom inside the cavity will increase, which means the speed of the emitter will be faster. Another advantage of surface plasmon is to control the far field radiation pattern by nanostructures. In 2002, a counter-intuitive phenomenon of narrow-beam emission from a subwavelength nanoaperture surrounded by corrugations was experimentally reported [86]. We integrated single CdSe / ZnS core-shell quantum dot into these subwavelength structures to build a single-photon emitter. The critical issue for such sub-wavelength structures, however, is the efficiency of coupling the light between them and a desired free-space mode without much loss due to scattering into other modes. One example of a subwavelength metal cavity is a narrow slit made in a metal film, which is equivalent to a rectangular box with metal walls. One dimension of such box can be made arbitrarily small [87].

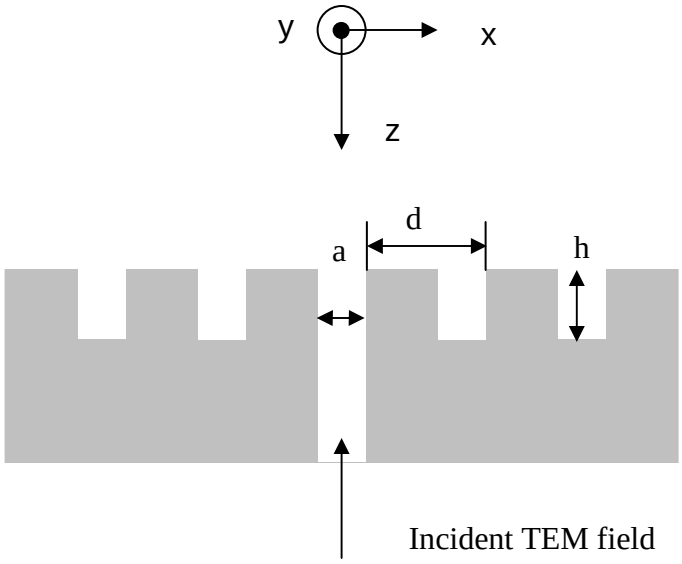

Figure 2.8. TEM wave around metal nanoaperture.

We are specifically concerned with the particular 2D geometry, in which the subwavelength metal slit (nanoaperture) is surrounded by periodic corrugations (grooves) as shown in Fig. 2.8. The problem of diffraction from the corrugated metal-nanoaperture can be treated using scalar diffraction theory [88]. In the structure of Fig. 2.8, the slit and each groove can be considered metal slab waveguides supporting only the fundamental TEM mode. The incident TEM field is exiting a corrugated output face. Then, for the plane z=0, we can obtain:

$$E_{\mathrm{x}}(x) = \frac{\mathrm{i}k}{2}\tan(kh)\int_{-\infty}^{+\infty} H_0^{(1)}(k|x-x'|)E_x(x')\mathrm{d}x' \quad \text{(for grooves)} \quad (2.46)$$

and

$$E_0 = 2A_0 - \frac{k\sqrt{a}}{2}\int_{-\infty}^{+\infty} H_0^{(1)}(k|x-x'|)E_x(x')\mathrm{d}x' \quad \text{(for slit)} \quad (2.47)$$

where *k* is the wavevector, d is the period of corrugations, a is the width of the central slit and h is the depth of grooves in *z*-direction and H_0^1 is a Hankel function describing cylindrical wave from a 2D point source. Eventually, one can obtain the far-field intensity emission pattern as:

$$I(\theta) = \frac{ka}{2\pi}\left[\frac{\sin(k_x a/2)}{k_x a/2}\right]^2 \frac{\left|\sum_\alpha E_\alpha e^{-ik_x \alpha d}\right|}{\left|A_0\right|^2 - \left|A_0 - E_0\right|^2}\ , \tag{2.48}$$

where $I(\theta)$ is the ratio of the power sent per unit angle θ in direction $\hat{r}$ to the total power emitted by the slit.

To compute the electrical and magnetic fields at the output face of a corrugated subwavelength metal nanoaperture, we need to consider the following parameters:

- *N*, number of grooves on either side of the central aperture
- *h*, depth of the groove
- *a*, the width of the slit and groove
- *d*, periods of grooves
- λ, wavelength of the TM-field incident on nanoaperture

For example, if *N*, *h*, *d*, *a* = {10, 160 nm, 500 nm, 40 nm}, the azimuthal intensity emission pattern is shown in Fig. 2.9 [89].

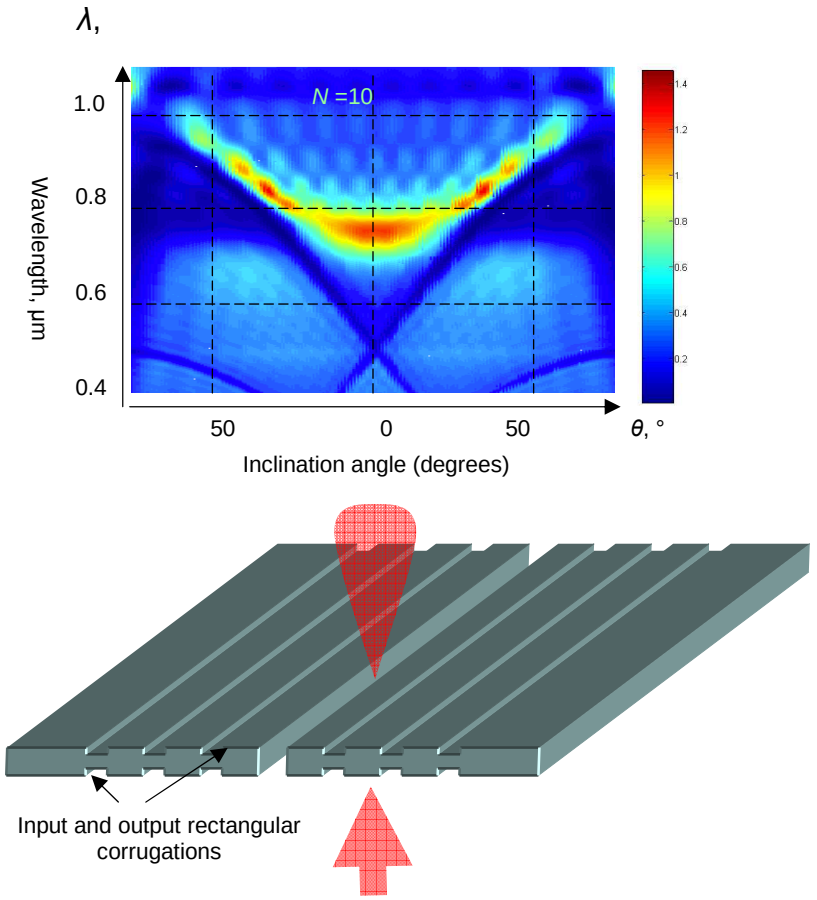

Figure 2.9. Azimuthal intensity emission patterns for various wavelengths, for geometry N, h, d, a = {10, 160 nm, 500 nm, 40 nm}.

2.7 Sample Fabrication

With the fast evolution of integrated circuit fabrication processes, several nano-structure fabrication technologies have been developed. Surface plasmonic nano-structure can be made using existing semiconductor fabrication techniques. Table 2.2 gives an overview of the different process steps that a wafer undergoes during its fabrication in the clean-room. To fabricate the slit surrounded by periodic corrugations plasmonic structures, we semiconductor fabrication processes in green boxes in table

2.2: wafer wet clean, physical vapor deposition, lithography (FIB), etching (FIB) and testing.

Table 2.2 Semiconductor Manufacturing Processes

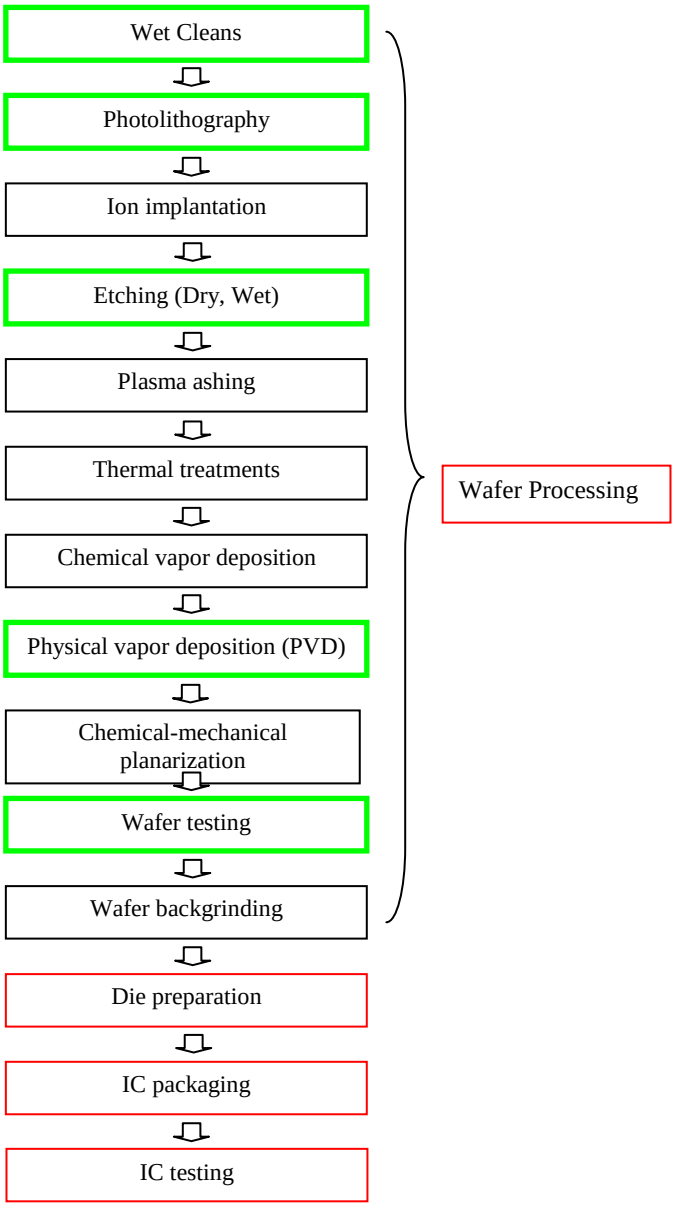

2.7.1 Wafer Cleaning

Our surface plasmonic nano-structures are fabricated on silver thin film which is deposited on microscope cover glass. The wafer cleaning process is very important for semiconductor chip fabrication, and so it is for surface-plasmonic nano-structure fabrication. The RCA clean is a standard set of wafer cleaning steps in semiconductor manufacturing. Here, we transplant the RCA clean process to our nano-structure substrate – cover glass clean process. In 1965, Werner Kern developed the basic procedure while working for RCA (Radio Corporation of America). It involves the following steps:

1. Removal of the organics
2. Removal of thin oxide layer
3. Removal of ionic contamination

For our fabrication processes, we do not need to worry about the removal of oxide layer. Therefore, we skip the step 2 and only use step 1 and 3. The detailed substrate-cover glass cleaning process is shown in table 2.3.

Table 2.3 Cover Glass Substrate Cleaning Process

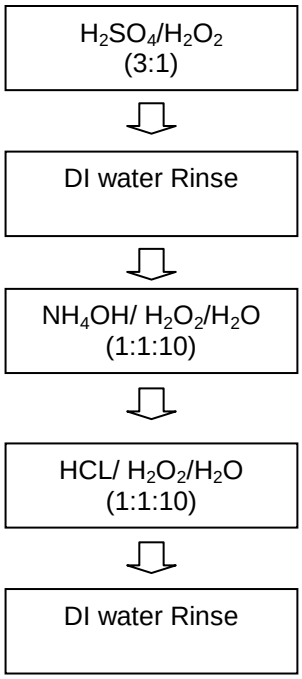

90-110˚C 10min	Strips organics
Room Temperature	
70-90˚C 5-10min	Strips organics Metals and particles
80-90˚C 5-10min	Strips alkali ions and metals
Room Temperature	

2.7.2 Silver Thin Film Deposition

Methods of thin film deposition are usually separated into two main categories: Chemical Vapor Deposition (CVD) and Physical Vapor Deposition (PVD). In each case the wafer is placed in a deposition chamber and constituents of the film are delivered through the gas phase to the surface of the substrate where they form the film. For CVD, the wafer (substrate) is exposed to one or more volatile precursors, which react and/or decompose on the substrate surface to produce the desired deposit. In the case of PVD, physical methods are used to produce the constituent atoms which pass through a low-pressure gas phase and then condense on the substrate. For our silver thin film

deposition, we choose to use PVD method. PVD techniques are generally more versatile than CVD methods, allowing for the deposition of almost any material.

There are a variety of different PVD methods:

- **Thermal Evaporation Deposition**: the source material is placed in a crucible, which is heated by an electric filament, melted metal blasts away some into highly ionized vapor to be deposited onto the substrate.
- **Electron beam physical vapor deposition**: the material to be deposited is heated to a high vapor pressure by electron beam and is transported by diffusion to be deposited by condensation on the substrate.
- **Pulsed laser deposition** a high power laser ablates material from the target into a vapor.
- **Sputter deposition**: a glowing plasma discharge knocks the material from the target and sputters some away as a vapor for subsequent deposition.

The principles of all PVD systems except sputtering are very similar. A schematic of a simple evaporator system is shown in Fig. 2.10. The source material is heated in a vacuum chamber which has initially been pumped down to 10^{-6} torr. Evaporated atoms from the source condense on the surfaces of the wafers. The heater can be of the resistance type, by a tungsten filament heated up when current passes through it (thermal evaporation system). Or an e-beam heater is used, in which a high-energy electron beam is focused onto the source material in a crucible using magnetic

fields (electron beam physical vapor deposition system). Another method is the source heated by a pulsed laser (pulsed laser deposition system). Since the evaporated atoms are transported through a high-vacuum atmosphere, very little gas-phase scattering occurs. Therefore, evaporated particles can travel directly to the substrate.

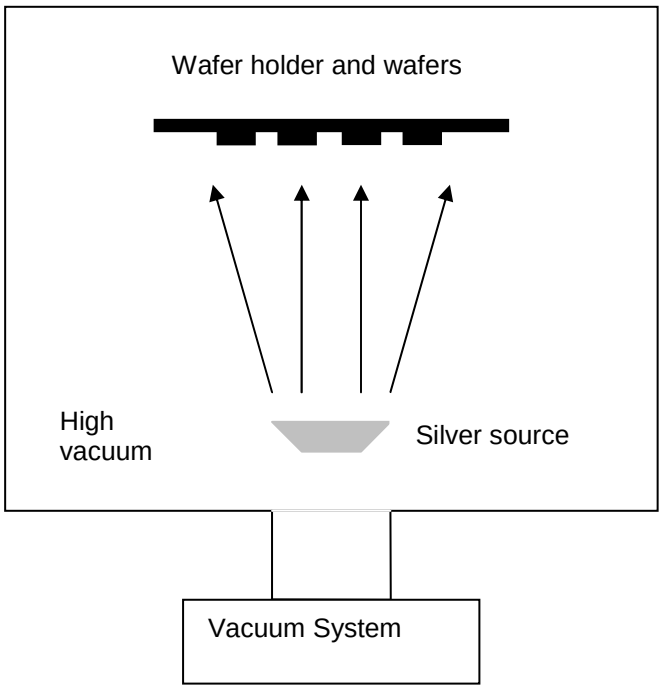

Figure 2.10. Thermal Evaporator Deposition System.

For our experiment, we use thermal evaporator deposition system (AJA ATC orion series). The purity of the deposited film depends on the quality of the vacuum and on the purity of the source material. 99.99% purity silver pellets has been used in the experiment. The deposition thickness resolution of our AJA thermal evaporator deposition system is 0.1 angstrom. At a given vacuum pressure, the purity of the film will be higher at higher deposition rates, but this means uniformity is bad. Therefore, we

use 1 angstrom per second deposition rate, which gives relativly high film purity and good uniformity. To obtain this deposition rate, a 2.9 ampere's of current has been used. Lower vacuum pressure gives higher purity and better uniformity of the thin film. For our experiment, we pump the vacuum pressure to less than 1×10^{-6} torr each time.

2.7.3 Surface Plamsonic Nanostructure Fabrication on the Silver Thin Film

After cleaning the substrate and depositing the silver thin film, we do the lithography and etching on the film. For applications in visible and near-infrared spectral ranges, the plasmonic structures need to be fabricated with a precision on the order of tens of nanometers. Conventional microelectronics fabrication methods, such as visible and UV lithography and broad-beam ion etch, can not control the feature sizes on such scales. There are two main methods for the fabrication of plasmonic nanostructures: electron beam lithography combined with either lift-off or etching process, and direct writing by focused ion beam (FIB). Electron beam lithography is not the most efficient process for plasmonic structures fabrication and requires further processing- lift-off or etching processes before the final device is created. While robust, this process also does not provide sufficient flexibility for quick prototyping.

On the other hand, focused ion beam (FIB) milling is widely accepted as a method of choice for rapid prototyping of electronic and photonic devices which requires critical parameters at the sub-wavelength scale. The FIB fabrication process uses a finely focused beam of ions that can be operated at low beam currents for imaging or high beam currents for site specific sputtering or milling. This process is

similar to the processes that combined lithography and etching. FIB can sputter away bulk material with nanoscale spatial accuracy. The FIB approach offers a simple method to structuring bulk materials, by providing a maskless process that circumvents the pitfalls of resist-based lithography processes. It is an excellent method for fabrication of plasmonic structures on dielectric substrates.

The FIB systems have been commercialized since 1980s, first primarily for the large semiconductor manufacturers. FIB systems operate in a similar way to a scanning electron microscope except, rather than an electrons beam, by using an ion beam (usually Gallium). The most important characteristics and consequences for the sample interaction are: 1) ions are larger than electron: the penetration depth of the ions is much lower than the penetration of electrons of the same energy; 2) ions are heavier than electrons; 3) ions are positive and electrons are negative.

There are basic three usages of FIB: imaging, deposition, and milling [90]. As shown in Fig. 2.11 (a), the gallium ion beam hits the sample surface and sputters a small amount of material. The sputtered material leaves the surface as either secondary ions or neutral atoms. As the primary beam rasters on the sample surface, the signal from the sputtered ions or secondary electrons is collected by a detector and then to form an image. In our experiment, Carl Zeiss crossbeam 1540XB has been used, which is a dual beam (e-beam and ion beam) system. At low primary beam currents, very little material is sputtered and this 1540XB system can easily achieve 5nm imaging resolution (imaging resolution with Ga ions is limited by sputtering and detector efficiency).

However, the disadvantages of FIB image are the difficulties of imaging non-conducting samples (which is also a disadvantage of SEM) and also the damage to the surface of the sample by the ion beam. FIB can also be used for a deposition system by ion beam induced deposition. This deposition process occurs when a gas is introduced to the vacuum chamber and allowed to chemisorb onto the sample as shown in Fig. 2.11 (b). The precursor gas will be decomposed into volatile and non-volatile components by scanning an area with the ion beam. The volatile part will be pumped out by high vacuum pump and the non-volatile component will remain on the surface as a deposition. Another main application of FIB is maskless micro/nano-milling machine. The removal of sample material is achieved using a high ion current beam, which is a physical sputtering process of sample material, as illustrated schematically in Fig. 2.11 (c). By scanning the ion beam over the substrate of the sample, an arbitrary shape can be formed.

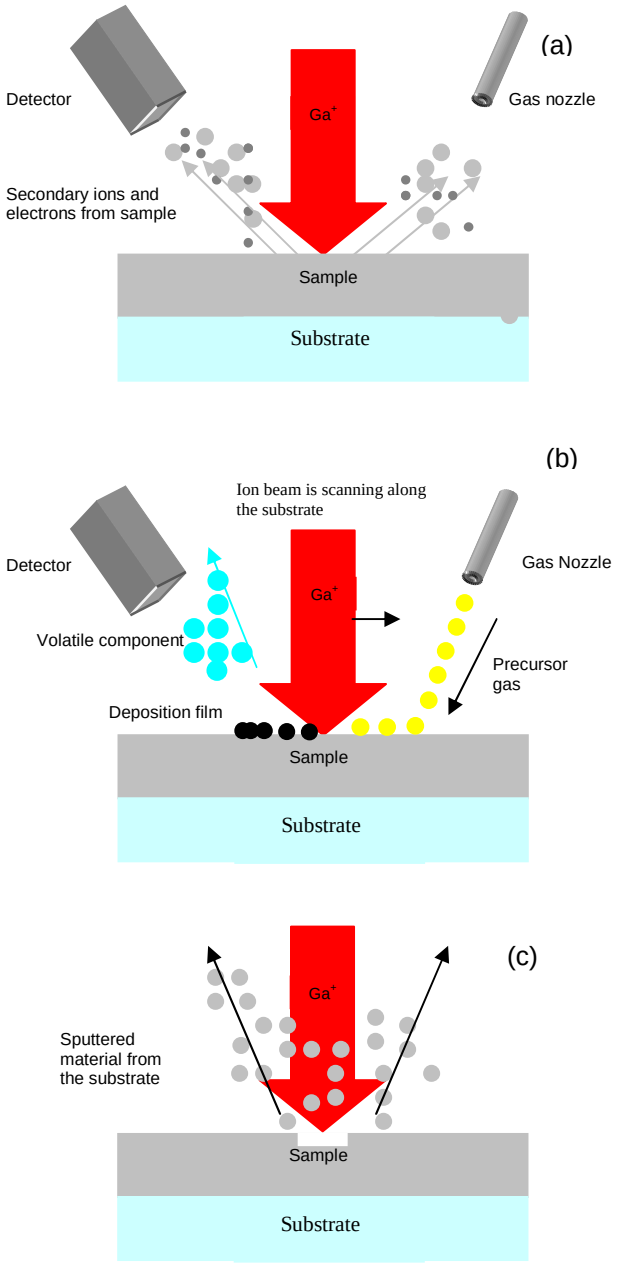

Figure 2.11. Physical principle of focused ion beam
(a) imaging, (b) deposition, and (c) milling.

For our single-photon emitter cavity fabrication, we only use the milling function of the FIB. After we finish the sample fabrication by FIB, we will use the

electron beam to take the images. As we discussed in Chapter 2.4, from Purcell effect we know the smaller the volume, the faster the spontaneous emission rate, therefore, we need to fabricate the cavity as small as possible. For our Carl Zeiss 1540XB FIB system, it is a dual beam system shown in Fig 2.12.

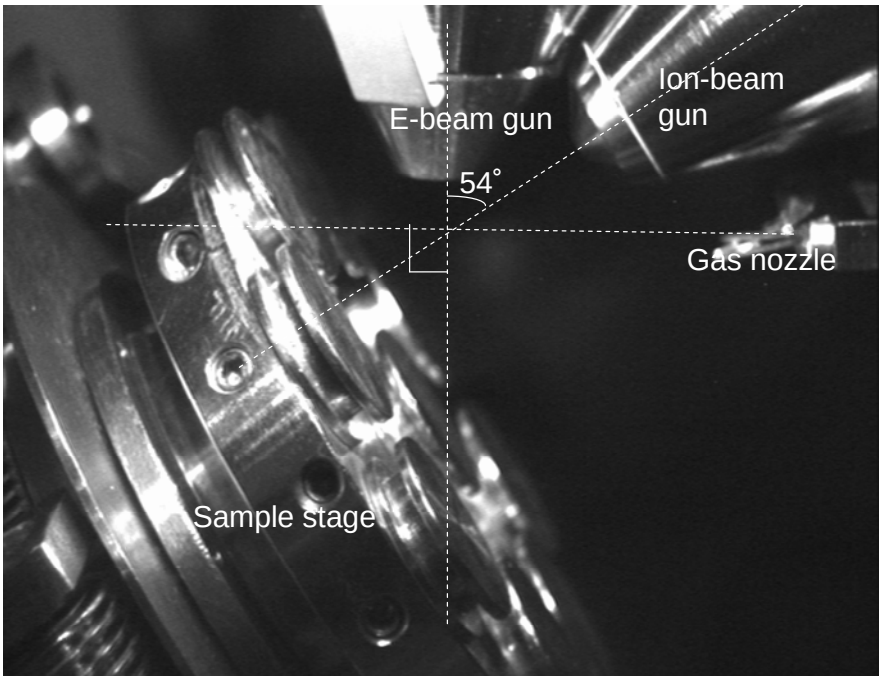

Figure 2.12 Schematic diagram of the Carl Zeiss 1540XB FIB system

The electron beam is vertically illuminated on the surface of the sample and the ion (Gallium) beam is at 54˚ angle with the electron beam. Before using the FIB, we need to optimize the system. The first thing that we need to do is to find the coincident point. The coincident point is defined as the position in the chamber where the SEM and FIB are both focused on, and scanning the same area of the specimen as shown in Fig. 2.12. Once the sample is tilted 54°, it must be raised in the chamber in order to achieve

coincidence between the SEM and the FIB optics. For 1540XB, the coincident working distance is just slightly less than 5mm from the SEM objective lens's bottom. Secondly, similar to e-beam lithography, in order to obtain good pattern, the beam should be well adjusted. There are two main parameters which will affect the beam quality: focus and astigmatism. To optimize the beam, focus and astigmatism correction should be properly adjusted in high magnification. However, as mentioned in the FIB imaging part, to obtain the image by ion beam, the ion beam will scan the surface of the sample, which induces some damage to the sample. This damage can be neglected at lower magnification. With the increasing of the magnification, the scanning area of the ion beam becomes smaller and the damage of the surface of the sample becomes worse. To reduce this milling effect, a fine ion beam (fine spot and low ion current) should be used. But a smaller ion current means the energy and momentum of the ion is smaller, the secondary electrons or secondary ions generated by the ion beam will be less, the signal generated by the detector will be weaker, the image will be not sharp and so it is not easy to correct the focus and astigmatism. On the positive side, the fine ion current provides narrower beam waist, which is perfect for milling a small nano-structure. Again, as the old saying, coin has two sides. Fine ion beam gives narrower beam waist, but also weak beam. If we want to mill to certain depth, it will take very long time by fine ion beam. After long time milling, the sidewall of the structures will be v-shaped instead of the perfect vertical one. The summary of the fine ion beam is shown in table 2.4.

Table 2.4 Advantages and disadvantages of fine ion beam

Fine ion beam (fine current)	Advantages	Disadvantages
Image	No surface damage	Weak signal, not sharp
Milling	Narrower beam waist	Longer milling time, v-shaped sidewall

To use the fine ion beam, we should consider both good and bad sides of it. The 1540XB FIB system provides current channels from 1pA to 50nA. We find 5pA is a good choice for our cavity fabrication. This current dose not damage the surface in high magnification, but provide a sharp image; it does not take too long the mill the cavity, but gives a narrow beam and makes a good straight, vertical sidewall of the cavity. The dose that we use is 100nc / cm. When the current, dose, structure and size of the pattern are chosen, the beam diameter and mill time are fixed. If the beam size and mill time are decided, is there any other factor which can affect the feature of the structure? This question brings us to think about the FIB scanning method. In FIB, milling is performed by a precise pixel-by-pixel movement shown in Fig. 2.13. The distance between the centers of two adjacent pixels is called the pixel spacing and the amount of time that the beam remains on a given target pixel is called the dwell time [90]. The spacing distance should not be too long; otherwise the mill will not be continuous. Also this distance should not be too small; otherwise the mill time will be too long. After optimization, we

find 15nm is a good choice. Now only one factor-the dwell time is not chosen. The dwell time will decide the moving speed of the ion beam. Here we need to introduce a new concept “single pass and multiple passes”. Single pass means the ion beam only mill each pixel once and the moving speed of the beam is slow. Multiple passes means the ion beam can mills each pixel multiple times and the moving speed of the beam is fast. Multiple passes can provide flat channel bottom and vertical sidewalls. Therefore we use multiple passes to fabricate our sample. 6 time passes is a good number for our sample.

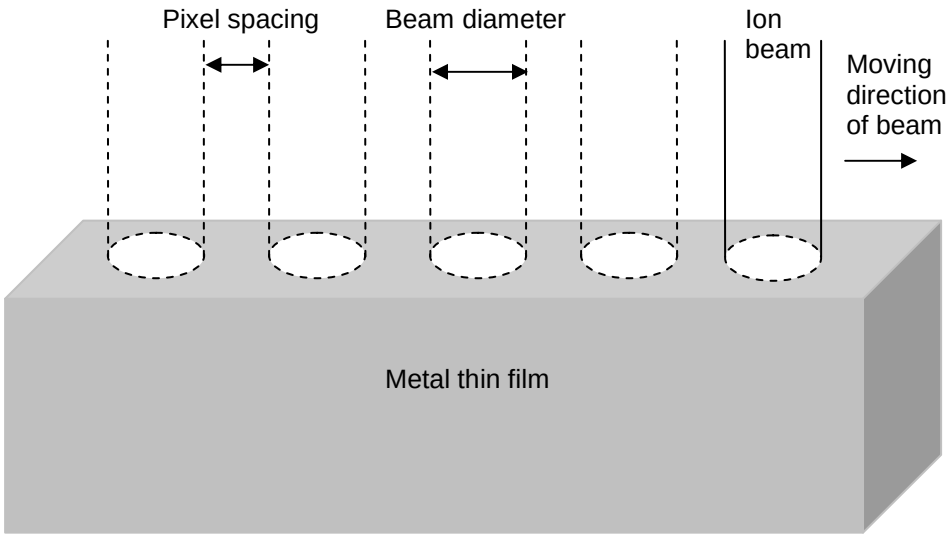

Figure 2.13 Schematic diagram of FIB milling

In order to fabricate a good sample by FIB, here are the fabrication steps and tips:

1. Find the coincident working distance.

2. Find the best milling current. The rule to find the milling current is the milling time is not too long in this current and the FIB image should be sharp enough to correct the focus and astigmatism.
3. Correct the focus and astigmatism. Like in all other microscopes, a standard object needs to be used to do the correction. For SEM, a gold standard (gold nano-particles) is a good choice. However, it can not be used for FIB (the gold standard can be easily damaged by the ion beam). Our suggestion is to mill a circle by FIB, take a sharp SEM picture of this circle and then use this SEM image as a standard to correct the focus and astigmatism for FIB.
4. Choose the dose.
5. Choose the pixel spacing distance and dwell time (the number of the passes)

The sample of a slit nano-aperture surrounded by periodic corrugations is shown in Fig. 2.14. The widths of the central nano-aperture and the corrugations are 60nm and 40nm. The thickness of the silver thin film is 300nm. The central nano-aperture is cutting through the film and depth of each periodic corrugation is about 110nm. The periodicity of grooves is 500nm. The length of the central slit and periodic corrugations is 20 microns. We use a length (in this case 20 microns) that is much larger than the characteristic parameters of the nano-structure in y-direction to make the structure satisfy the 2D situation.

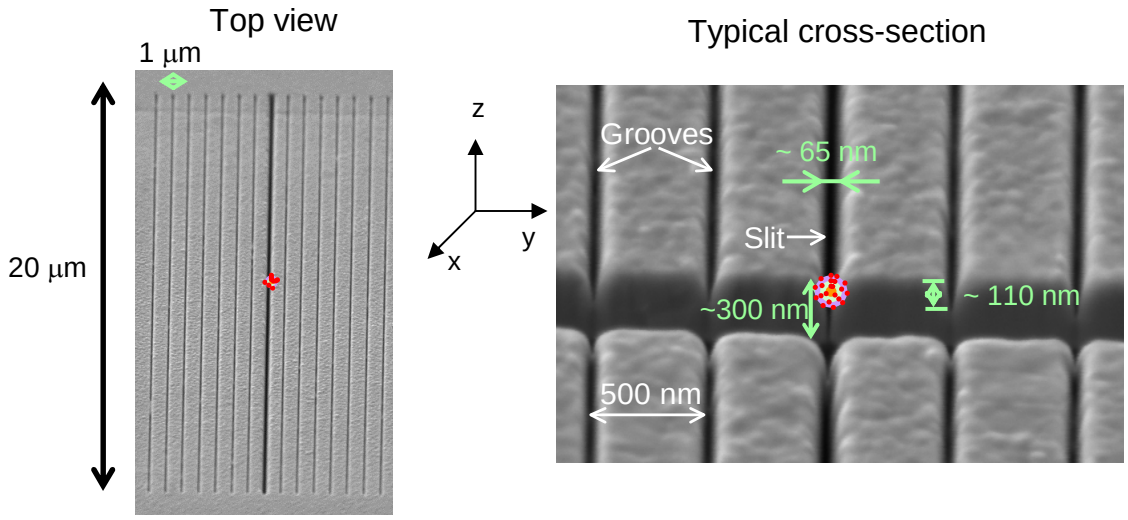

Figure 2.14. Fabrication of a slit nano-aperture surrounded by periodic corrugations.

To make a single-photon emitter, we need to integrate a gain medium (in our experiment, we use a single quantum dot) into the cavity. In the experiments, we use the CdSe/ZnS core/shell quantum dots from Ocean Nanotech with an octadecinine ligand layer, a central wavelength of emission λ_0 = 630 nm, and a spectral width of ~25 nm. These dots are available in powder form, which has longer shelf life than quantum-dot solutions. The typical diameter of the core/shell ligand's structure is 10...15 nm. The absorption and emission spectrum is shown in Fig. 2.15 [91].

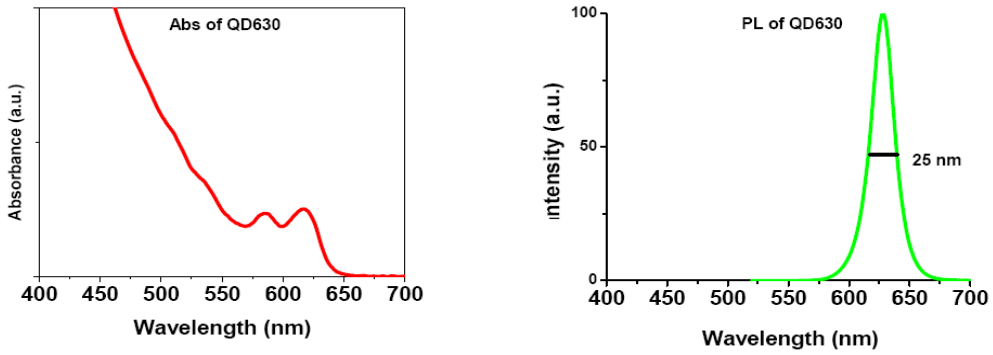

Figure 2.15. Absorption and emission spectra of CdSe / ZnS quantum dot.

To deposit the single CdSe / ZnS quantum dot (QD) into the cavity, we spin toluene solution with QD on the surface of the metal film, as shown in Fig. 2.16. By appropriate choice of dot concentration in the solution and several deposition attempts, one dot can be placed in the area of interest or inside of the slit cavity. Radiation of the neighboring dots is avoided by high-contrast optical selectivity (about 5 microns) of the measurement.

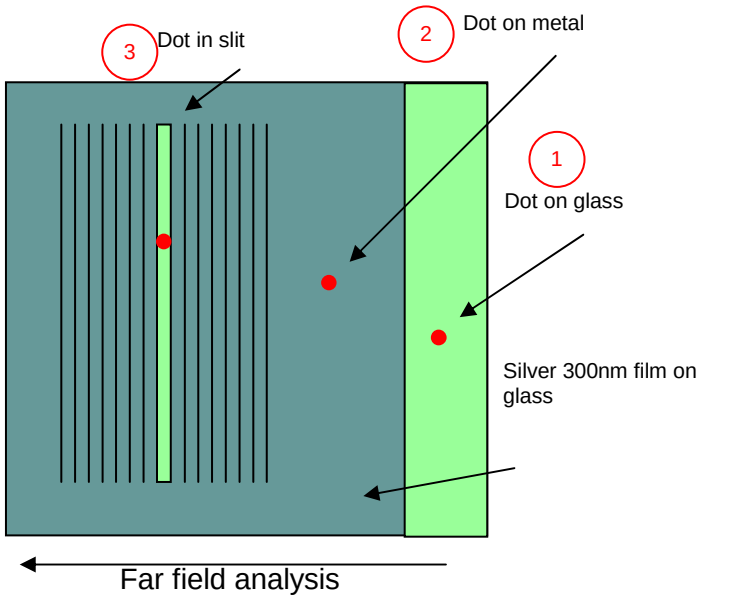

Figure 2.16. Placement of a quantum dot into the cavity.

By assuming quantum efficiency of a dot and it absorption cross-section, and by measuring powers and beam profiles of excitation and fluorescence beams, the number of dots under investigation can be evaluated from these fluorescence measurements.

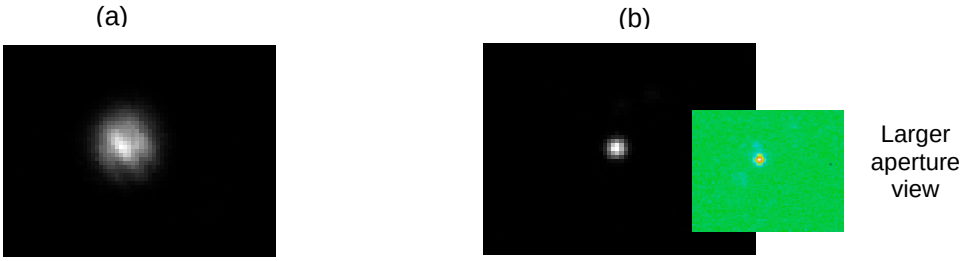

Figure 2.17. (a) Near field image of the green laser beam.
(b) Near field fluorescence of quantum dot.

We use a 532nm pulse laser to illuminate the quantum dot. The power of the green laser is about 1.2 microwatts and the beam profile is shown in Fig. 2.17 (a). Then we use bandpass filter to block the excitation source, and then we can obtain the near-

field fluorescence image of the quantum dot shown in Fig. 2.17 (b). The absorption cross-section of the quantum dot can be found from reference [91]:

$$C_{abs} = \zeta\alpha \frac{4\pi}{3} r_{QDcore}^3 \tag{2.49}$$

The relationship between the excitation power and the fluorescence power is shown in equation (2.50):

$$P_{625\,nm} = \eta \frac{\lambda_{532}}{\lambda_{625}} \frac{NA^2}{4\pi} \underbrace{\zeta\alpha \frac{4\pi}{3} r_{QDcore}^3}_{\text{Abs Cross-section}} \frac{N_{dots}}{A_{532nm\ beam}} P_{532\,nm} \ , \tag{2.50}$$

where $P_{532\,nm}$ and $P_{625\,nm}$ are the powers of the pump laser and the fluorescence from the quantum dot, η is the quantum efficiency of the quantum dot, NA is the numerical aperture of the objective lens and A is the area of the laser beam. From equation (2.49), we can calculate the number of dots N_{dots}, since we know the absorption cross-section of the quantum dot at 532nm. In our sample, we could get the $N_{dot} = 1$ when the fluorescence power is about 1.6×10^{-14} watt.

2.8 Measurement Experiment Set-up and Results

After we fabricate the cavity and integrate the single quantum dot into the cavity, we need to analyze the emitter. The experimental setup for direct spectrally resolved far-field measurement is shown in Fig. 2.18. We analyze the structure by a confocal fluorescence microscope in diascopic (transmission) illumination mode with collecting dry objective with NA=0.85. The collected light is processed by a modified

version of spatially resolving spectrometer [92] placed in the Fourier plane of the objective. This allows us to directly measure angularly resolved emission spectra from the corrugated pattern. After putting a mirror above the image-plane aperture, we can obtain the near-field fluorescence image of the quantum dot by near-field CCD camera.

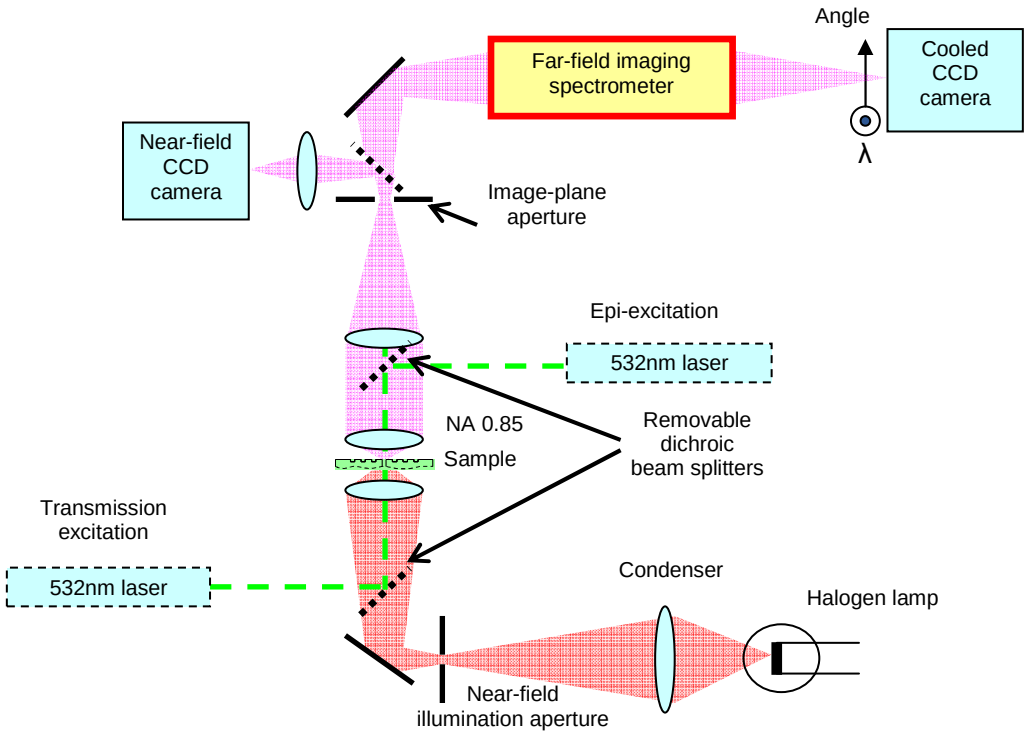

Fig. 2.18. Experimental setup for direct spectrally resolved far-field measurement.

First, we measure the transmission for $60\times80\times300\text{nm}$ waveguides on a cover glass substrate. The structure is shown in Fig 2.19 and the transmission spectrum is shown in Fig 2.20. Quality factor ($f/\Delta f$) is about 10, which is in a good agreement with the propagation loss and reflection coefficient estimations for a silver slit of 80×600×300nm dimensions. Purcell factor of 10 can be expected in such cavity:

$$F_p = \frac{3}{4\pi^2}\frac{(\lambda/n)^3}{V}Q \sim \frac{3}{4\pi^2}\frac{(0.625*1)^3}{0.3*0.08*0.6}10 \sim 12.9. \qquad (2.51)$$

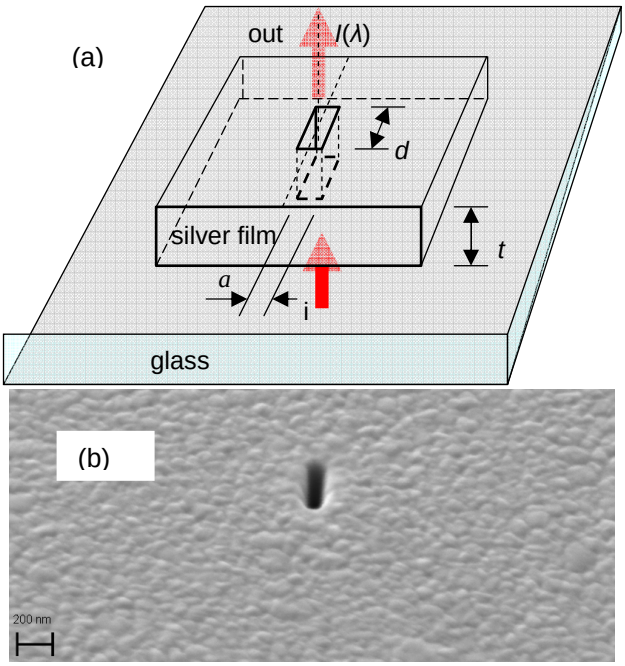

Figure 2.19. (a) Structure of $60\times80\times300nm$ waveguides. (b) SEM image of the waveguide.

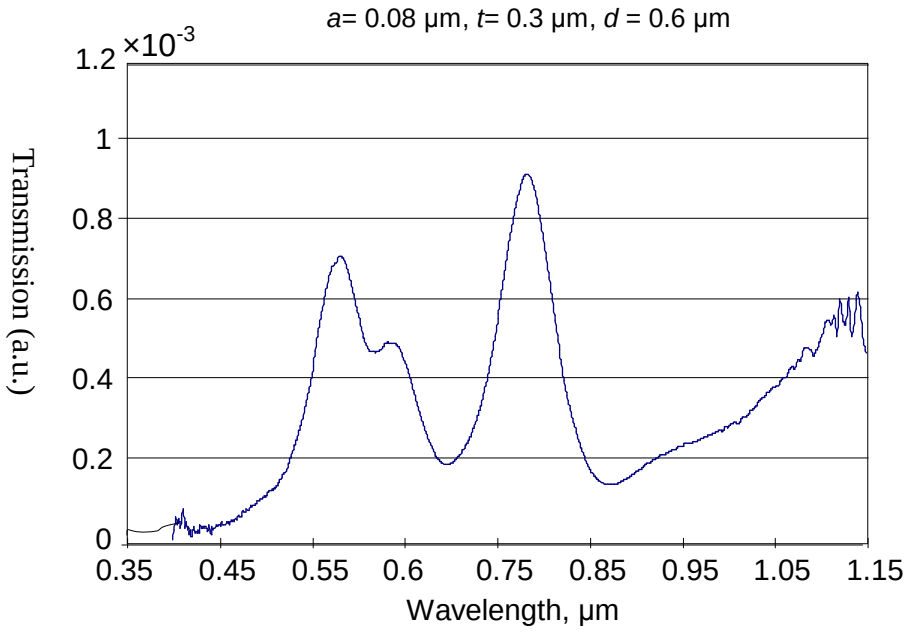

Figure 2.20. Transmission spectra of the $60\times80\times300$nm waveguide.

The spatially resolving spectrometer shown in Fig.2.18 allows us to directly measure angularly resolved transmission and emission spectra from the corrugated pattern; the fabricated structure is shown in Fig. 2.14. Spectrograms of white light transmittance from the nanostructure with N=7 grooves on each side of the slit. h=110 nm depth of the grooves, and d=500 nm groove period are shown in Fig 2.21: the spectrogram in Fig 2.21 (a) is the theoretical prediction, and the spectrogram in Fig. 2.21 (b) is the experimental result. These two results are in a good agreement. As illustrated in Fig. 2.21 (b), the peak of the spectrum is around 600nm, which is matched well with the emission peak of the CdSe / ZnS quantum dot. Also the angular distribution of the transmission spectrum is narrowed down to 20˚.

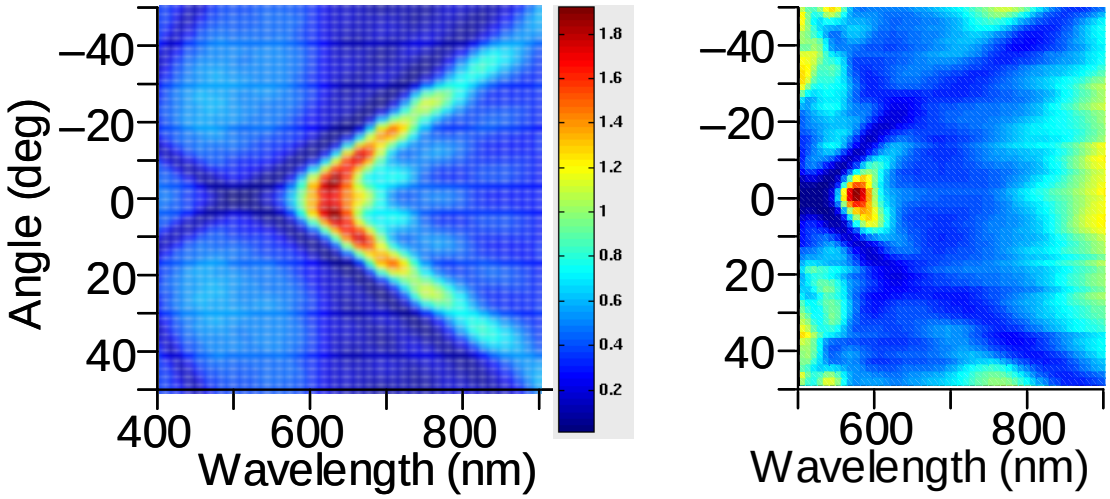

Figure 2.21. (a) Modeling predictions for angular emission pattern from the nanostructure with N=7 grooves on each side of the slit,h=110 nm depth of the grooves, and d=500 nm groove period. (b) Experimentally measured transmission pattern (without quantum dots).

Next, we position several colloidal CdSe/ZnS core-shell quantum dots with average emission peak near 630 nm into the central slit and calculate the number of quantum dots by the method introduced in chapter 2.7.4. Spectrograms of fluorescence from a single Quantum Dot inside the central slit is shown in Fig. 2.22 (b). Fig. 2.22 (a) is the same as rotated Fig. 2.21 (b) and is used to show the region of the spectrogram, magnified in Fig. 2.22 (b). Then we integrate the transmission power of Fig. 2.22 (b) over the angular distribution to obtain Fig. 2.22 (c).

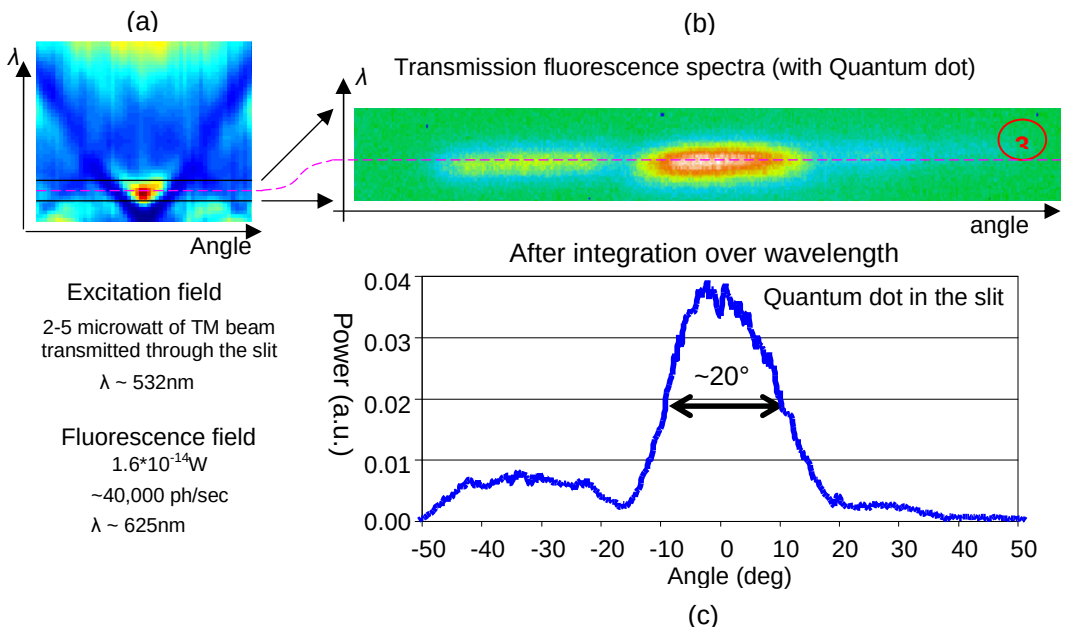

Fig. 2.22. Spectrograms of fluorescence from a single Quantum Dot (a) Angular transmission spectrum without quantum dots for the central slit nanostructure with N=7 grooves on each side of the slit, h=110 nm depth of the grooves (b) Emission spectrum from the same structure with a single QD. (c) Angularly-integrated spectra of fluorescence from the CdSe/ZnS core-shell quantum dot positioned inside the slit nano-aperture.

We also compare the emission pattern of single quantum dot in the slit surrounded by corrugations under 532nm with the spectra and angular patterns obtained from single quantum dots on non-corrugated silver film and on glass, as shown in Fig. 2.23. The emission spectrum and angular pattern are shown in Figs. 2.23 (a) and (b) respectively. We can easily see a drastic reduction in the angular spread of the quantum dot's spontaneous emission in the presence of the corrugated nanostructure [30]. The structure concentrates most of the emission into a single peak compatible with

numerical apertures of common optical fibers, thereby promising a great improvement in the fluorescence collection efficiency for future quantum-optics applications.

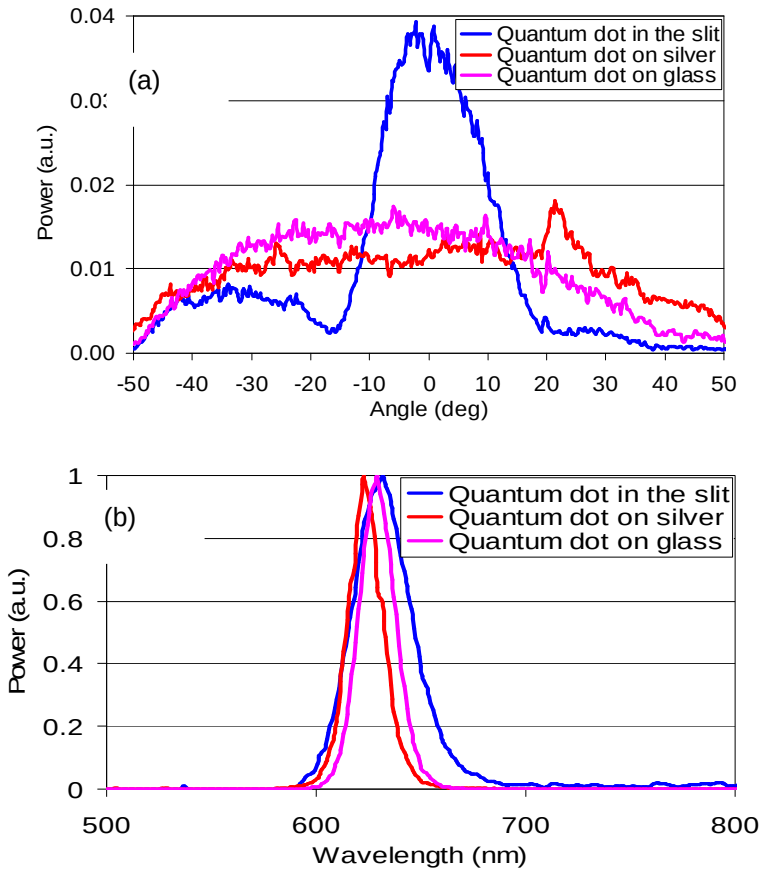

Figure 2.23. (a) Wavelength-integrated spectra of fluorescence from the CdSe/ZnS core-shell quantum dot positioned either inside the slit nanoaperture, or on non-corrugated silver film, or on glass. (b) Angularly-integrated spectra of fluorescence from the CdSe/ZnS core-shell quantum dot positioned either inside the slit nanoaperture, or on non-corrugated silver film, or on glass.

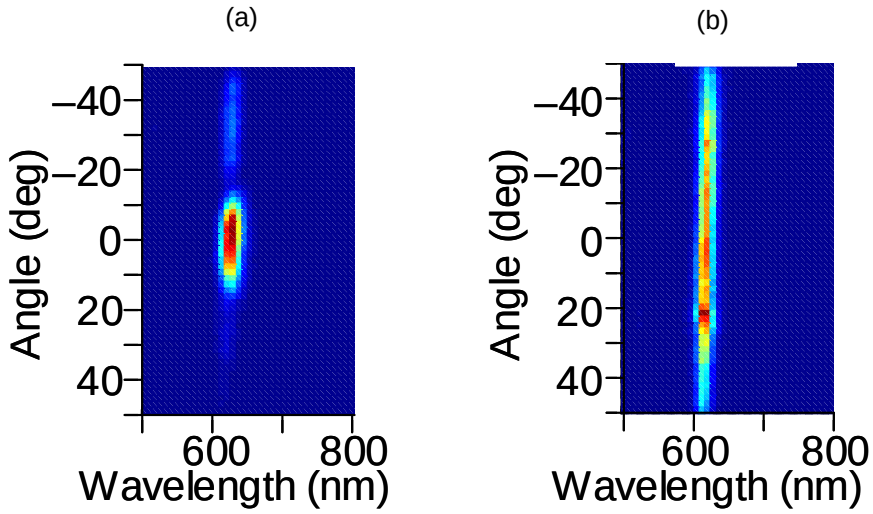

Figure 2.24. (a) Angular emission spectrum with a single quantum dot inside the central slit nanostructure with *N*=7 grooves on each side of the slit. (b) Angular emission spectrum with a single quantum dot on the silver film.

2.9 "Donut" Waveguides

One potential way to reduce the size of the cavity is to fabricate a cylindrical 3D structure. Fig. 2.25 shows our design of "hole" and "donut" waveguides.

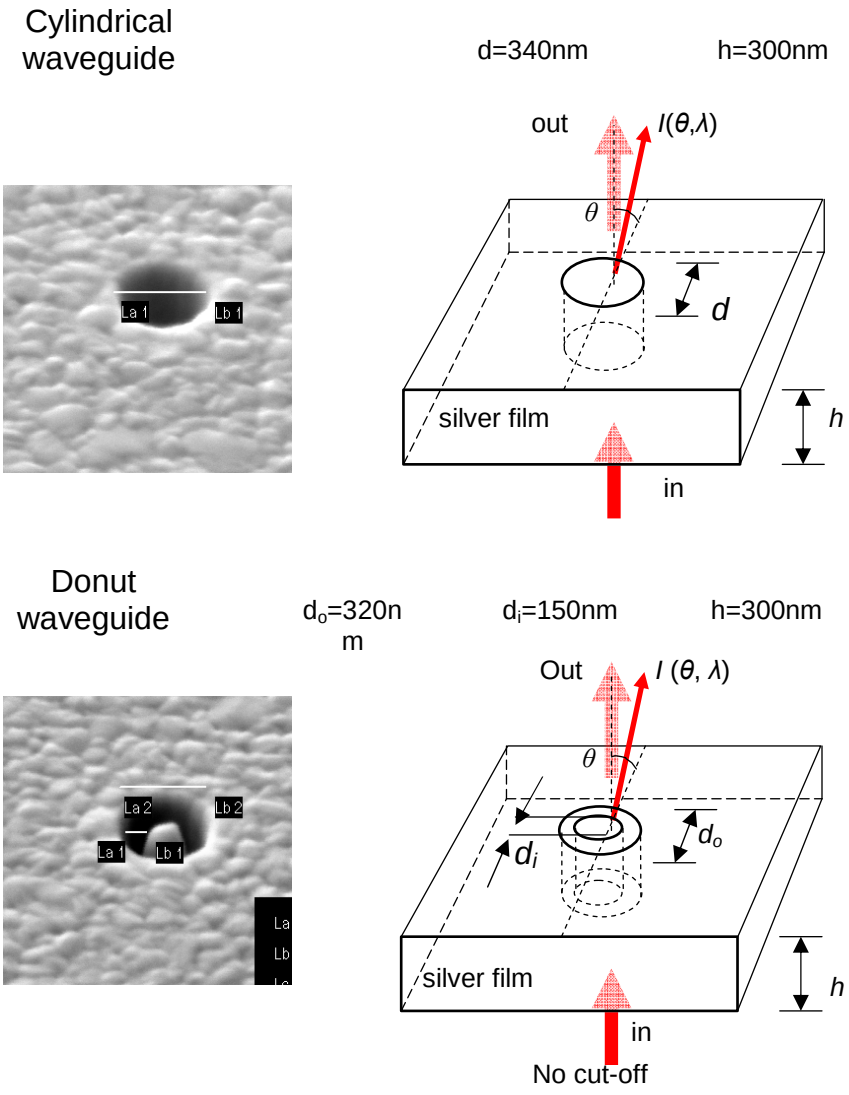

Figure 2.25. Schematic and notation for hole and donut waveguides.

The transmission spectra shown in Fig. 2.26 confirm that the larger transmission through the "donut" waveguide at longer wavelength, owing to the absence of the cutoff frequency in the "donut" waveguide, which is expected from a coaxial cable analogy. We have investigated several designs of nano-apertures in view of their resonant

properties. We found that the most compact and robust to fabrication errors metal waveguides structures are the "donut" waveguides, where $\lambda^3 Q/V$ ratio of 10 can be repeatedly obtained at 600 nm wavelength.

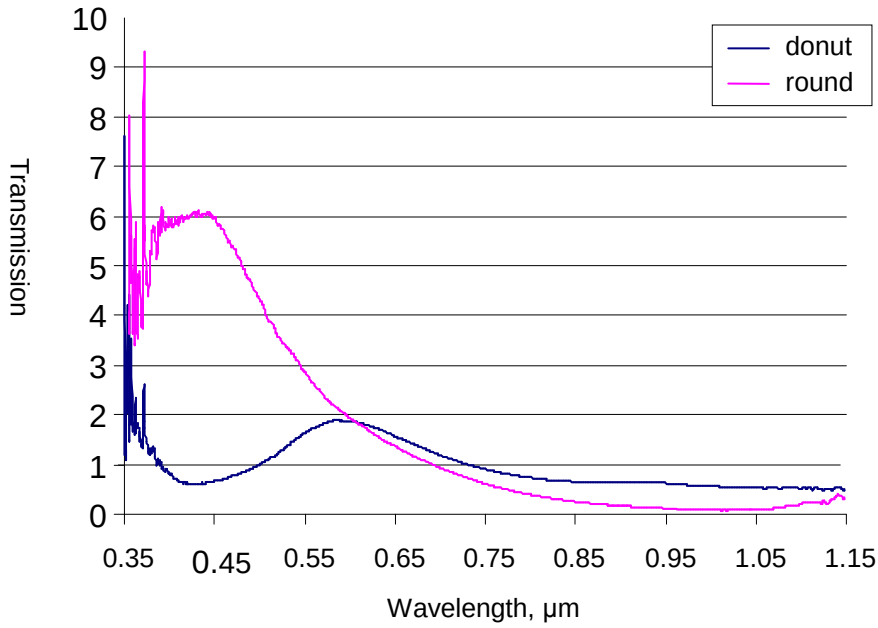

Figure 2.26. Transmission spectra of "donut" and hole waveguides.

2.10 Conclusions

We have demonstrated narrowing of the far-field fluorescence pattern from a quantum dot positioned inside a rectangular (slit) nanoaperture surrounded by periodic corrugations

Most (80%) of the emerging spontaneous emission is concentrated in a beam with angular half-width at half-maximum of ~10°

This indicates the potential for using such a corrugated nanostructure for efficient coupling into and out of the slit metal nanocavities designed for enhancement of nonlinear- and quantum-optical effects

CHAPTER 3

SPONTANEOUS DECAY OF CDSE / ZNS CORE-SHELL QUANTUM DOTS AT THE AIR-DIELECTRIC INTERFACE

As introduced in chapter 2, single-photon sources are important for secure communication lines and linear-optics-based quantum computing. For these applications, the single-photon sources need significant improvements in efficiency and speed. Because of the high internal quantum efficiency of quantum dots, the quantum-dot-based single-photon sources are a promising development direction [94, 95]. However, the nano-scale engineering of such sources has many challenges, including embedding of the quantum dot into an optical medium or a resonator structure without fluorescence quenching [96], as well as dealing with the short-term instabilities (blinking) [97,98], long-term instabilities (chemical degradation) [99], and homogeneous broadening of the dot's radiation spectrum due to interaction with phonons. One promising way of increasing the quantum dots' emission rate (and, hence, the potential speed of quantum communication) is to use the electric field enhancement by metals and metallic resonant structures [100, 101]. However, the presence of a material with free electrons (metals) near the dot also induces a strong non-radiative relaxation [102], which limits the benefits of this approach. In the microcavity-based single-photon sources (e.g., see review [3]), the emission rate increase originates from both resonant enhancement of the local density of states and from the dielectric

properties of the material surrounding the quantum dot. Thus, it is hard to separate and compare the impacts of these two contributions on the total emission rate. While the influence of the nearby metal on the quantum-dot emission has received a lot of attention recently, e.g. [103, 34], the studies of the role of surrounding dielectric in quantum-dot fluorescence have been rather limited. Damped-oscillator-like dependence of the fluorescence decay time on the distance between the quantum dot and silicon substrate was shown in [35] and the reduction of the decay time on glass surface compared to the decay time in free space was shown in [36]. The impact of the interaction within an ensemble of quantum dots on the emission spectra was studied in [37].

In this chapter, we experimentally investigate the effect of the surrounding dielectric material on the reduction of the fluorescence decay time of quantum dots. A dot at the surface of a high-refractive-index dielectric is coupled to the denser vacuum field of the dielectric and thus experiences a faster decay. We derive simple theoretical expressions that predict up to one order of magnitude improvement in the decay rate. We analyze experimentally the lifetime of long-wavelength ($\lambda \approx 630$ nm) CdSe / ZnS core-shell quantum dots either deposited in different ways on a surface of four dielectric media or dissolved in the liquids of reference, toluene and hexane. The experimental data measured for low-index dielectrics ($n < 2$) match well with the model of a dipole equally shared between two interfacing media, while for high-index dielectrics ($n > 2$),

such as silicon, the correction factors due to reflections and evanescent-field coupling are required.

3.1 Background

The spontaneous emission rate of an atom in free space is given by [104]:

$$\gamma_{\text{free-space}} = \frac{1}{\tau} \approx \frac{8\pi^2}{3} e^2 \langle d \rangle^2 \frac{1}{\eta \varepsilon_0 \lambda_0^3} \tag{3.1}$$

where $e<d>$ is the dipole moment of the transition, $\hbar$ is the Plank's constant, λ_0 is the emission wavelength in vacuum, and ε_0 is the permittivity of vacuum.

When the electric field interacts with an atom, it is very easy just to consider the field is the average macroscopic electric field. However, at a microscopic level we would clearly expect E to vary with position so an actual dipole within the material may well experience a rather different electric field! How can we improve the model to get a more reliable connection between macroscopic measurements and microscopic models? This is done by taking into account local field effects. We assume that the actual E - field seen by a dipole, its local field, E_{local}, is given by the sum:

$$E_{\text{local}} = E_{\text{a}} + E_{\text{lor}} + E_{\text{sph}} \tag{3.2}$$

where E_{a} is the average macroscopic field, E_{lor} is the Lorentz field due to polarization charge and E_{sph} is the contribution from the material inside the "removed" sphere but excluding the central dipole. By symmetry, One third of the intracavity field arises due

to fields that are perpendicular to the interfaces while two thirds are associated with tangential fields, the Lorentz field is:

$$E_{\text{lor}} = \frac{P}{3\varepsilon_0} \tag{3.3}$$

For a cubic system because of the high symmetry, we have $E_{sph} = 0$.

Finally, we end up with the result:

$$E_{\text{local}} = E + \frac{P}{3\varepsilon_0} \tag{3.4}$$

where $P = \varepsilon_0 \chi E$, the express of the local field becomes:

$$E_{\text{local}} = \frac{(\varepsilon + 2)}{3} E \tag{3.5}$$

By considering the local field correction, the spontaneous emission rate for an atom in a dielectric host medium with dielectric permittivity $\varepsilon_{\text{medium}}$ is [102]:

$$\gamma_{\text{atom}}^{\text{medium}} \approx \gamma_{\text{free-space}} \sqrt{\varepsilon_{\text{medium}}} \left(\frac{\varepsilon_{\text{mediium}} + 2}{3} \right)^2 \tag{3.6}$$

The atom transitions are initiated by the interference of vacuum fields coming from different modes. Each mode contains vacuum noise with zero-point energy of one half of a photon. The density of modes in the dielectric is n^3 times higher than in free space, but the vacuum field variance is n^2 times lower. Therefore, the probability of the atom "ignition" is increased n times [factor with the square root of $\varepsilon_{\text{medium}}$ in Eq. (3.6)]. Equation (3.6) also considers that atom is contained in a small (less than the average

inter-atomic distance) empty virtual spherical cavity formed inside the continuous dielectric medium. The atom sees a higher local field than the average macroscopic field [the former can be expressed as the latter multiplied by a factor (ε_{medium}+2) / 3 coming from Lorentz-Lorenz, or Clausius-Mossotti, equation, as illustrated in Fig. 3.1(a)], and the resulting radiative decay is faster than that in free space.

The optical transition of a quantum dot can be approximated as a two-level atom with a large electron orbit and, therefore, with a large dipole moment $e\langle d\rangle$. The background vacuum field interacts with this dipole moment and induces the spontaneous emission. In contrast to the atom, the quantum-dot electron levels are spread over thousands of atoms and, therefore, interact with average *macroscopic* vacuum field. There is no Clausius-Mossotti factor in conventional understanding. Instead, the difference between the dielectric constants of the quantum-dot material ε_{dot} and the medium ε_{medium}, where typically $\varepsilon_{dot} > \varepsilon_{medium}$, *reduces* the field inside the dot by a factor (ε_{medium}+2) / (ε_{dot}+2). This factor comes from considering a spherical cavity filled by material of permittivity ε_{dot}, formed inside the continuous dielectric medium of permittivity ε_{medium}, i.e. Clausius-Mossotti relation acts in the opposite direction: the dielectric constant of the dot reduces the vacuum field of the outside medium and hence slows down the decay. The decay rate of a quantum dot in vacuum is

$$\gamma_{dot}^{\text{free-space}} = \gamma_{\text{free-space}} \left(\frac{3}{\varepsilon_{dot} + 2} \right)^2 \qquad (3.7)$$

where $\gamma_{free-space}$ is the decay rate in vacuum of a two-level system with the same large dipole moment as that of the quantum dot ("*big-atom*" with the refractive index of 1). The expression for the quantum-dot decay rate in the dielectric medium is:

$$\gamma_{\text{dot}}^{\text{medium}} = \gamma_{\text{free-space}} \sqrt{\varepsilon_{\text{medium}}} \left(\frac{\varepsilon_{\text{medium}} + 2}{\varepsilon_{\text{dot}} + 2} \right)^2 \tag{3.8}$$

After normalization to the quantum-dot's free-space decay rate of Eq. (3.7), the factor $\varepsilon_{\text{dot}} + 2$ in Eqs. (3.7), (3.8) cancels out, yielding the following expression:

$$\gamma_{\text{dot}}^{\text{medium}} = \gamma_{\text{dot}}^{\text{free-space}} \sqrt{\varepsilon_{\text{medium}}} \left(\frac{\varepsilon_{\text{medium}} + 2}{3} \right)^2 \tag{3.9}$$

This expression no longer depends on the refractive index of the quantum-dot material. This result can also be obtained from Eq. (3.6) by noting that $\gamma_{free-space}$ in Eq. (3.7) is a fictitious non-observable quantity, and the inverse Clausius-Mossotti factor in Eq. (3.7) can be incorporated into $\gamma_{free-space}$ by simply redefining the dipole moment of the quantum dot in Eq. (3.1).

The real core/shell quantum dots have a complex structure (core-shell-ligands) which practically do not affect the coupling with vacuum fields. For the sake of simplicity, the quantum dot can be considered to be a concentric two-sphere structure (core-ligands) with a core diameter much smaller than that of the ligands. In this case, the local-field correction factor stays the same:

$$\frac{\varepsilon_{\text{medium}} + 2}{\varepsilon_{\text{dot}} + 2} \text{ is replaced by } \frac{\varepsilon_{\text{medium}} + 2}{\varepsilon_{\text{ligands}} + 2} \frac{\varepsilon_{\text{ligands}} + 2}{\varepsilon_{\text{dot}} + 2} = \frac{\varepsilon_{\text{medium}} + 2}{\varepsilon_{\text{dot}} + 2} \tag{3.10}$$

This means that Eqs. (3.8), (3.9) are also applicable to the core-shell quantum dots. Thus, the dependence of the quantum-dot decay rate on the dielectric constant of the host medium (3.9) is similar to Eq. (3.6) for an atom, and is applicable to dots completely immersed into the host dielectric. The typical situation described by this formula is the dot immersed in a liquid.

Another typical situation is the dot attached to a dielectric surface (e.g. glass, sapphire or silicon). If the center of the dot is assumed to be placed exactly at the dielectric interface, this situation can be approximated analytically in a simple way [105]. The resulting decay rate is the sum of the half-rate into the air and the half-rate into the dielectric. Using Eq. (3.9), we obtain such experimentally observable rate as

$$\gamma_{\mathrm{dot}}^{\mathrm{interface}} \approx \frac{\gamma_{\mathrm{dot}}^{\text{free-space}} + \gamma_{\mathrm{dot}}^{\mathrm{medium}}}{2} \approx \frac{\gamma_{\mathrm{dot}}^{\text{free-space}}}{2}\left[1+\sqrt{\varepsilon_{\mathrm{medium}}}\left(\frac{\varepsilon_{\mathrm{medium}}+2}{3}\right)^2\right] \qquad (3.11)$$

Figure 3.1(b) illustrates the dependence of the decay rates of a dot on the medium's refractive index $\mathrm{n} = \sqrt{\varepsilon_{\mathrm{medium}}}$ for the cases of complete immersion [solid blue line, Eq. (3.9)] and air-dielectric interface [solid red line, Eq. (3.11)]. We see that, for high-index dielectrics, the rate enhancement in the bulk host scales as $\sim n^5/9$ (dashed purple line) and can exceed 100, whereas the enhancement at the interface is about one half of that in the bulk dielectric.

In particular, for a dot embedded in silicon ($n \approx 3.5$), the decay enhancement factor can reach the value of 80. However, the high-index dielectrics and semiconductors often demonstrate optical losses. The near-field longitudinal component

of the dot's radiating field gets absorbed and contributes to the non-radiative losses. The total decay time of the dot in the dielectric host is the inverse of the sum of radiative and non-radiative decay:

$$\tau = 1/\gamma_{dot}^{total} = 1/\gamma_{dot}^{radiatve} + 1/\gamma_{dot}^{non-radiatve} \tag{3.12}$$

For the dot embedded into the high-index dielectric or semiconductor such as silicon, the radiative decay time can be reduced down to several nanoseconds; however, the non-radiative part of the decay, if significant, may degrade the efficiency.

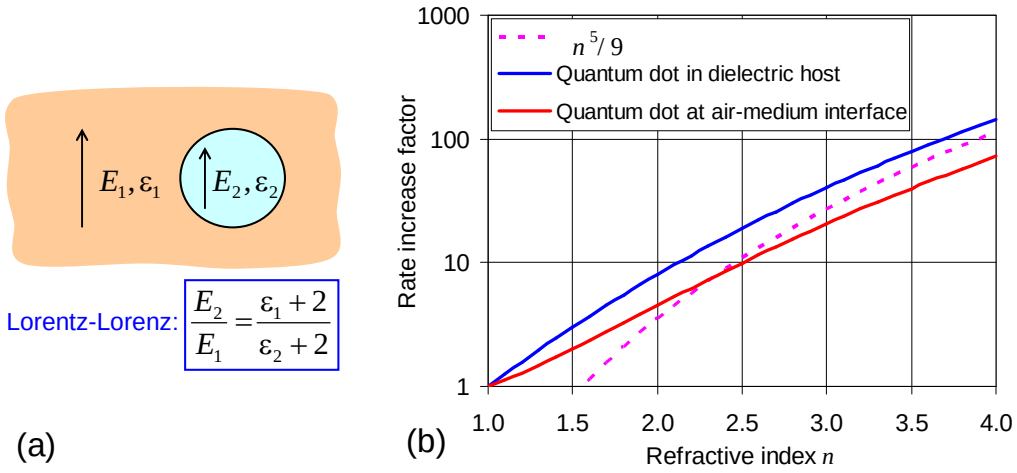

Figure 3.1. (a) Illustration of Lorentz-Lorenz / Clausius-Mossotti relationship between the macroscopic electric field E_1 and the local field E_2 seen by the atom ($\varepsilon_2 = 1$) or quantum dot ($\varepsilon_2 = \varepsilon_{dot}$). (b) Enhancement of the radiative decay rate, compared to the rate in free space, by the refractive index n of the dielectric surrounding the quantum dot. The solid blue line corresponds to the case of complete embedding of the quantum dot into the dielectric host [Eq. (3.10)]. The solid red line corresponds to the quantum dot positioned at the air-dielectric interface [Eq. (3.11)]. The dashed purple line shows the asymptotic dependence $n^5/9$.

3.2 Samples Fabrication and Experimental Setup

In the experiments, we use the CdSe/ZnS core/shell quantum dots with octadecinine ligand layer (Ocean Nanotech), which are the same as the ones used in chapter 2. Our measurements of the fluorescence intensity have confirmed the manufacturer-specified quantum efficiency of the fluorescence in toluene solution of about 50%.

The measurements are performed using avalanche photon counting module, start-stop counter (PicoHarp 300 from Picoquant GmbH), two Inverter and Attenuator Modules (SIA 400 from Picoquant GmbH), function generator, laser driver and a home-made pulsed blue laser system arranged in a configuration shown in Fig. 3.2.

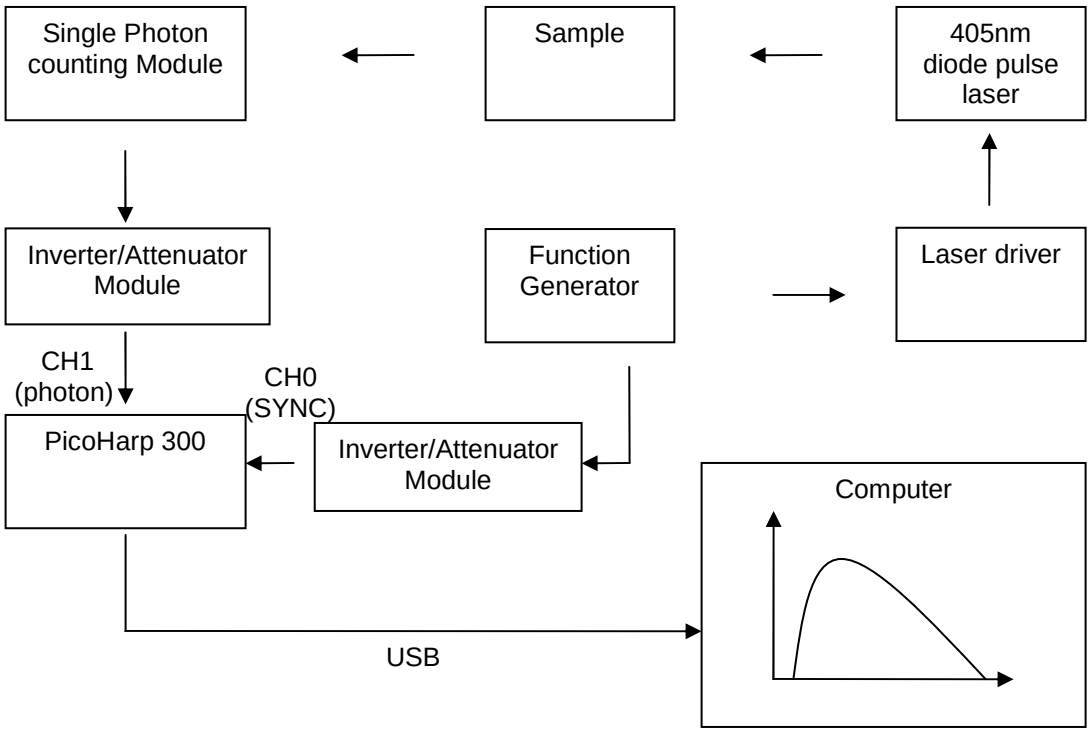

Figure 3.2. Schematic picture of the measurement system.

Data from the PicoHarp 300 are transmitted to the computer and analyzed for time delay probability distribution. Usually this measurement system is called time-correlated single photon counting (TCSPC) system, which means repetitive measurements of the time interval between an excitation pulse and the first detected fluorescence photon [106].

The principle of time correlated single photon counting is the detection of single photons and the measurement of their arrival times in respect to a reference signal, usually the light source. Time correlated single photon counting is a statistical method and a repetitive light source is needed to accumulate a sufficient number of photon events for a required statistical data precision. The probability of registering more than one photon per cycle is very low; the histogram of photon arrivals per time bin represents the time decay one would have obtained from a time-resolved analog recording. Fig. 3.3 illustrates how the histogram is formed. Pulsed laser is used to excite the fluorescence. The time difference between excitation and emission is measured by electronic device (in our experiment, we use PicoHarp 300). Since the PicoHarp 300 input channels are designed electrically identical, both can handle an input voltage range of 0 to -1 V. Therefore, the excitation and emission pulses are connected to the PicoHarp 300 through the pulse inverter with attenuation (SIA 400) as shown in Fig. 3.2. In some cycles, there will actually be no photons. The occurrence of a photon or an

empty cycle is entirely random and it only depends on the efficiency of the emitter (assuming there is no loss in the collection of the signal).

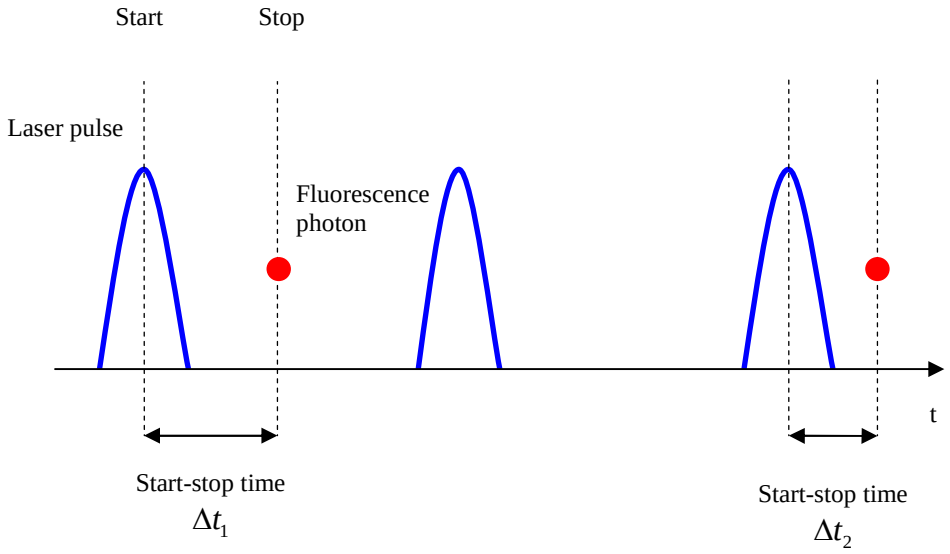

Figure 3.3. Physical principle of TCSPC system.

The histogram is collected in a block of memory, where one memory holds one time bin. These time bins are referred to as time channels. After many time bins have been collected, a histogram counts versus channels will represent the fluorescence intensity versus time.

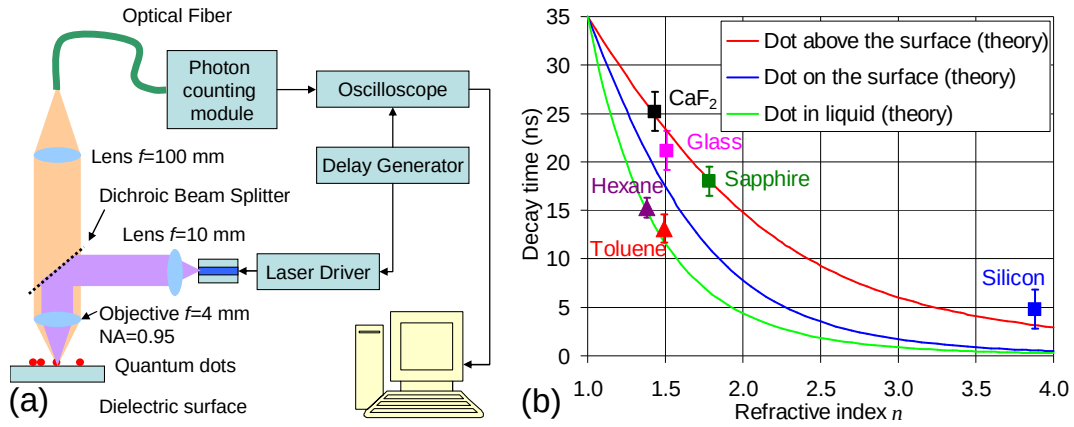

Figure 3.4. (a) Experimental setup. Quantum dots deposited on the dielectric are positioned on a 3D piezo-electric translation stage with 50 nm resolution. (b) Spontaneous decay time as a function of refractive index of the dielectric host or interface. The theoretical curves are Eq. (3.11) and Eq. (3.9) for the air-dielectric interface (blue) and liquid (green), respectively. Data for low-index dielectrics fit acceptably with the simple dipole-on-the-surface model of Eq. (3.11). However, the silicon sample shows considerably slower decay compared to the predicted values and requires a more complicated model of Eq. (3.13) (red), accounting for the distance between the quantum dot and the surface.

Our TCSPC experiment set-up is shown in Fig. 3.4 (a). In our experiment, a home-made pulse generator sent a rate of ~30 kHz electrical pulse to the blue diode laser. At the same time, an 30 kHz electrical timing reference signal (sync) from the function generator as a “start” signal is sent to the start-stop counter (PicoHarp 300 from Picoquant GmbH). The pump excitation pulses at wavelength 405 nm coming at a rate of ~30 kHz from the diode laser are reflected by the dichroic beam splitter and then through a numerical aperture NA = 0.95 objective lens illuminate on the quantum dot. For each measurement of the time decay, between 40,000 and 300,000 time-delay samples are taken. The fluorescence is collected by a single-mode fiber from the image

plane of a dot formed by a 1:40 telescope. The single-dot measurements have a strongly pronounced blinking behavior [97]. To avoid the distortion of lifetime data by the parasitic surface-state fluorescence, we discard all photon counting events occurring during the dark state of the quantum dot ("off" state of blinking). The resulting fluorescence decay times, shown in Fig. 3.4 (b), are obtained by averaging several individual measurements, examples of which are presented in Fig. 3.5 (a). In addition to the dependence on the refractive index of the host medium, the decay time is also a function of the dot concentration, of the state of the dielectric surface, and of the deposition method. Two methods are used in our experiments: spin-on of the quantum dots dissolved in toluene and spin-on from the solution in toluene with PMMA [107]. The first method brings high repeatability in the measurements of decay time; the second brings a higher chemical long-term stability of fluorescence efficiency but with less reliable results in terms of the decay time. Both deposition procedures are performed as follows. The quantum dots are stored in a powder form. Prior to the sample preparation, a small piece of quantum-dot powder (typical size ~ 100–150 μm) is diluted in toluene to reach the concentration of 3×10^{11} dots/cm^3. Then solution is quickly spun-on to the desired surface. In the case of the second method, the weight percentage of PMMA in toluene is chosen to be around 1% to form a 10–20 nm film over the surface. A typical scanning electron microscope image of the quantum dots deposited on a silicon substrate is shown in Fig. 3.5 (b). The experimental setup shown in Fig. 3.4 (a) has a confocal scanning capability for visualizing and measuring the

spatial distribution of the fluorescence. Figure 3(c) shows a typical placement of dots at the surface of a glass as observed by the confocal fluorescence setup prior to the time-decay measurements. To eliminate the impact of closely spaced quantum dots (clusters) on the lifetime data, we select for the measurements only the isolated dots with the average intensity and small size in the observed confocal fluorescence image. Similar pictures are obtained for the three other dielectrics. The fluorescence count rates decrease as the refractive index of the dielectric increases: count rates from the quantum dots on the surface of silicon are almost an order of magnitude smaller than those at the surface of CaF_2. This reduction agrees with the reduction in the collection efficiency by a factor $\gamma_{dot}^{free\text{-}space}/(2\gamma_{dot}^{interface})$, arising from the fact that most of the light emitted by the dot goes into the high-index dielectric and is not collected by the objective on the free-space side of the interface. Hence, there is no indication of change in the intrinsic 50-% fluorescence efficiency of the quantum dot with the refractive index of the interface.

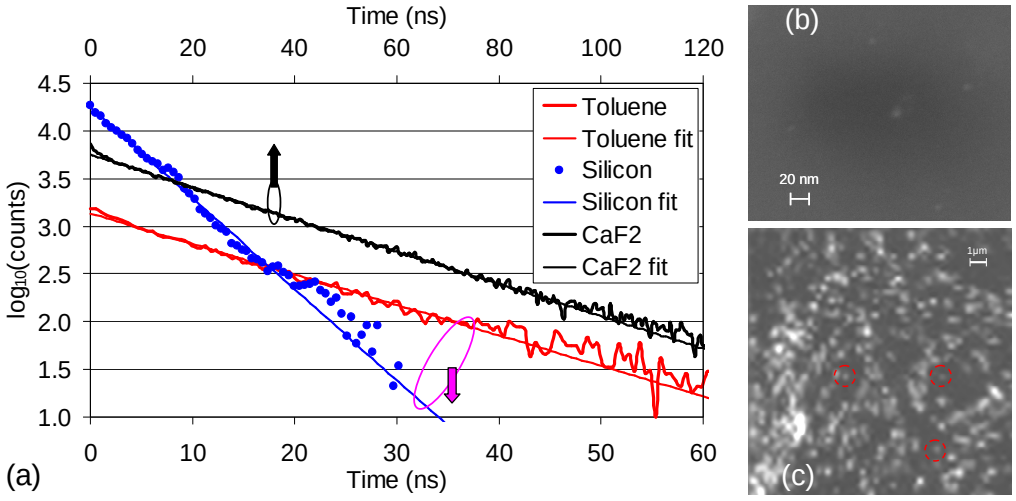

Figure 3.5. (a) Examples of the raw individual time-decay measurements used in generating the data points in Fig. 3.4 (b). The straight lines are the exponential fits yielding τ = 13.6, 4.6, and 25.6 ns for toluene, silicon, and CaF_2, respectively. (b) Scanning electron microscope image of quantum dots deposited on a silicon substrate. (c) The confocal fluorescence image of quantum dots deposited on a glass substrate. Red circles show the single dots selected for measurements after image analysis. These three dots satisfy the three important criteria: the brightness and the dot size correspond to a single dot particle, and these dots have largest mean square average distance from the neighbors (the typical distance is larger than λ_0).

The time decay of individual dots strongly fluctuates from one dot to another. This is most likely due to the following factors: the dot size diversity, as well as the variations in the orientation of the dots at the boundary and in the distance between the dots and the interface. Accurate measurement of the decay requires averaging the data from several dots. Points for dielectric interfaces in Fig. 3.4 (b) are averaged over 5–9 single-dot measurements. Points for liquids are averaged over 3–4 measurements with various concentrations. The quantum dots without PMMA show fast degradation of the fluorescence efficiency. For example, in toluene or hexane solution the typical long-

term decay time of fluorescence count rate is about 3–6 hours, while the long-term decay time for the dots on the surface of dielectric without PMMA varies between 1 and 10 hours. Additional verification measurements have shown that the long-term decline of the fluorescence count rate did not affect the fluorescence decay time for a given dot.

3.3 Results and Discussion

Measurements of the decay time for quantum dots on the surface of a dielectric and for dots in toluene and hexane are presented in Fig. 3.4(b). The data are in a good agreement with theory. With the increase of the refractive index, the time decay of the dot becomes consistently shorter. The results for liquids fit Eq. (3.9) well, with only one fitting parameter — decay time in free space $\tau = 1/\gamma_{\text{dot}}^{\text{free-space}}$ = 35 ns. The dots on the dielectric interfaces, on the other hand, do not follow the simple equally-shared-dipole model: although the data for $n < 2$ are in a reasonable agreement with the theory, the measured decay time for high-index material (silicon) is significantly longer than that predicted by Eq. (3.11).

The reason for this discrepancy is that the simple model (3.11) of a dipole equally shared between the two intefacing media is not well suited for high-index dielectric. Position of the dot is inherently asymmetric with respect to the surface boundary (dot is not centered on the interface, but is positioned slightly above it instead). In the case of a high-index dielectric, the characteristic penetration length of the evanescent vacuum field from the dielectric becomes comparable with the real distance between the dot and

the surface, and hence the ratio of the dot's coupling to the two media's continua of modes changes significantly. For the high-index case, the solid angle of propagating modes from the dielectric half-space (light cone) coupled to the dot becomes much less than 2π, and the main contribution on the dielectric side comes from the evanescent field. On the air side, the density of states is modified by a strong reflected field. Without attempting an exact analytical solution, we have phenomenologically modified Eq. (3.11) to account for the contributions of the evanescent and reflected fields at small distances from the interface by introducing an exponential coupling factor [108, 109]:

$$\gamma_{\text{dot}}^{\text{over interface}} \approx \gamma_{\text{dot}}^{\text{free-space}} \left\{ 1 + \frac{1}{2} e^{-\frac{3\pi^2}{4\lambda} a \sqrt{\varepsilon_{\text{medium}}} \left[\sqrt{\varepsilon_{\text{medium}}} \left(\frac{\varepsilon_{\text{medium}} + 2}{3} \right)^2 - 1 \right]} \right\}. \qquad (3.13)$$

Equation (3.13) fits well the ensemble of the obtained data, using the distance parameter a = 40 nm and $\tau = 1/\gamma_{\text{dot}}^{\text{free-space}}$ = 35 ns. *A posteriori* measurements of the surface of silicon revealed the presence of 25-nm-thick thermal oxide, which, along with 10...15 nm quantum-dot size estimate, justifies the non-zero value of the parameter a used in the fitting.

In our model, we have not considered the presence of the non-zero imaginary part of the refractive index. This imaginary part exists only in silicon case, where the energy of the emitted photons exceeds the bandgap, and may lead to increase in the non-radiative recombination rate. Even though our data do not indicate any decrease in the quantum dot emission efficiency for silicon, we are planning to conduct a separate study with a different type of quantum dots whose emission energy is below the silicon

bandgap to verify this.

The obtained results confirm the model's prediction of the significant decay rate increase at the surface of a dielectric: decay time decreases from 35 ns in free space to ~5 ns on silicon surface. Complete embedding of the quantum dot into a high-index material is expected to reduce the decay time to a sub-nanosecond scale. By designing the high-index dielectric in a shape of a semi-sphere, for example, one can efficiently collect the fluorescent photons on the dielectric side. Additionally, this purely dielectric broadband mechanism of the decay time reduction can be combined with the dielectric resonant cavity design. Such structure can modify the emission spectra of the quantum dot and allow the generation of photons-on-demand in a single-mode regime.

3.4 Conclusion and Outlook

We have analyzed the theoretical dependence of the decay rate on the refractive index for a quantum dot either in a dielectric medium or at the boundary of two media. Theory predicts up to 80-times increase in the spontaneous emission rate for the dots embedded into a high-index dielectric. The experiments conducted with CdSe/ZnS core-shell quantum dots show a reasonable agreement with the theory. This indicates that one can expect to design and fabricate the colloidal-quantum-dot-based single-photon emitters with near-nanosecond or even sub-nanosecond decay times and high fluorescence efficiency.

CHAPTER 4

SINGLE MODE FIBER-BASED SURFACE PLASMONIC OPTICAL TWEEZERS

The ability of plasmonic nano-structures to concentrate light to sub-micron volumes opens up the possibility of their use in optical trapping of particles (optical tweezers).

4.1 Optical Tweezers

4.1.1 Brownian Motion

For the optical trapping, Brownian motion of the particles is the one of the main enemies that need to be defeated. Particles suspended in a fluid are always moving. Diffusion is a common phenomenon observed from the movement of particles. Apart from diffusion, there is another interesting phenomenon that can be observed. It is called the Brownian motion. This phenomenon is discovered by a well-known botanist Robert Brown. In 1827, when he used a simple microscope to study the action of particles contained in the grains of pollens [110], he noticed the pollen jiggles around. However, he could not find what caused the motion at that time. Many explanations have been given to explain this phenomenon; however, none of them could convince the scientists. There are two key characteristics of Brownian motion: persistence and randomness. In 1905, Einstein published paper to theoretically analyze the Brownian

motion. His theory has two parts: first, he used the diffusion equation for Brownian particles, in which the diffusion coefficient is related to the mean square displacement of a Brownian particle; second, he related the diffusion coefficient to measurable physical quantities. Einstein showed that by measuring this quantity, one could prove that “the kinetic energy of the motion of the centre of gravity of a particle is independent of the size and nature of the particle and independent of the nature of its environment" [111].

However, only after the kinetic energy of molecules was understood, scientists realized that the Brownian motion is caused by the kinetic energy of the molecules suspended in liquid or gas. The main physical principle of Brownian motion is that the mean kinetic energy of any molecule of a liquid or gas is equal to the mean kinetic energy of a particle suspended in this ambience [112]. The mean kinetic energy of the motion can be written as:

$$\langle E \rangle = \frac{3}{2} kT \tag{4.1}$$

where k is the Boltzman constant and T is the temperature. From equation (4.1), we can see that the mean kinetic energy of Brownian motion is proportional to the temperature and just as Einstein said, this energy is not related to the size of the particle. Therefore, in order to trap a particle stably, the potential well generated by the optical tweezers should be significantly larger than the mean energy of the particles; we will detail this well depth in chapter 4.1.2.

4.1.2 Physical principle of optical tweezers

Back to 1873, James C. Maxwell theoretically deduced the radiation pressure of light based on his electromagnetic theory [113]. However, before the invention of the laser, the force generated by the light radiation was very weak and had almost no application. In 1970, Arthur Ashkin, a scientist working at Bell Labs, published a seminal paper [114] reporting that focused laser beams can be used to accelerate and trap micrometer-sized transparent particles. In 1986, Ashkin and colleagues reported the first observation of optical tweezers pheromone: a focus laser beam capable of holding microscopic particles stable in three dimensions [115]. The laser radiation pressure soon has been used to cool and trap atoms [116, 117]. Due to the picoNewton and nanometer ranges of force and distance, optical traps have been used for studying biological systems [118]. Throughout the 1990s and afterwards, scientists used optical trap force to investigate structural properties of biological polymers such as DNA [119, 120], whole cells [121], and microtubules [122].

4.1.2.1 Ray-optics approximation

If the size of particle is much larger than the trapping wavelength (usually more than ten times larger), the trapping phenomenon can be explained by ray optics.

Usually an optical trap is formed by tightly focusing a laser beam with an objective lens of high numerical aperture (NA). The dielectric particle near the focus will be trapped by the force due to the transfer of momentum from the scattering of incident photons. These optical forces can be separated into two types: first, a scattering

force, in the direction of light propagation; second, a gradient force, in the direction of spatial light gradient. As shown in Fig. 4.1 (a), a transparent particle is illuminated by a collimated beam with an intensity gradient. When a transparent particle is displaced from the laser beam center and moves to the left of the focus, the larger momentum change of the more intense rays cause a net force to push the particle back to the focus spot (the center of the beam). When the particle stays in the center of the beam, the resulting lateral force is zero as shown in Fig 4.1 (b).

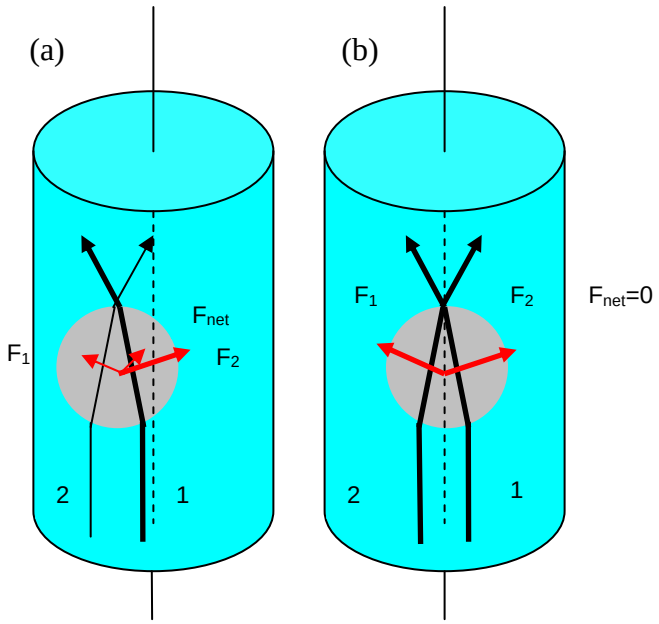

Figure 4.1. Schematic diagram of optical trapping by gradient force (a) When the bead is displaced from the beam center, the larger momentum change of the more intense rays causes a net force to be applied back toward the center of the laser. (b) When the bead is in the center of the laser, the net force works on the bead is zero and the bead is stable.

In addition to keeping the particle in the intensity center of the laser beam, a focused laser also keeps the particle in a fixed axial position. The momentum change of

the focused rays by the scattering light causes a force towards the laser focus shown in Fig. 4.2. In Fig. 4.2 (a), the particle is below the focus point. The scattering force generated by the laser beam will push the particle back to the focus point. Eventually, the particle will stay slightly above the focus spot shown in Fig. 4.2 (b). In this location, the net force of the scattering force compensates to the weight of the particle. All the above discussions, we neglect the surface reflection and absorption from the particle. The force working on the particle at a particular displacement from the focal spot is linearly proportional to the total laser power.

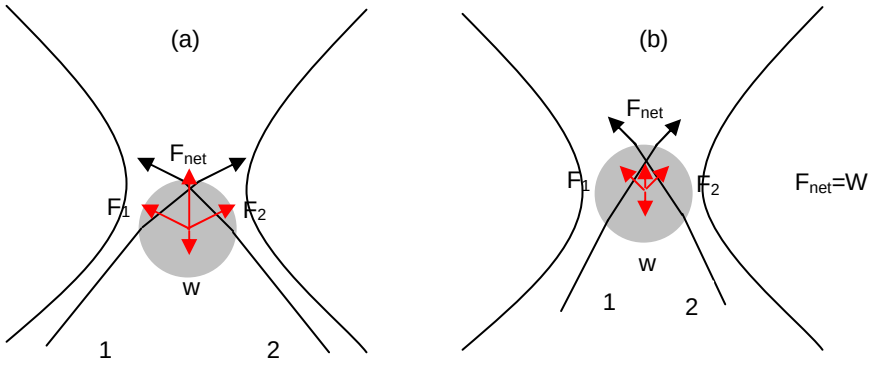

Figure 4.2. Schematic diagram of optical trapping by scattering force. (a) When the bead is displaced from focus of the laser, the momentum change of the focused rays causes a force towards the laser focus (b) When the bead is in the focal spot, the scattering force and the weight of the bead is balanced.

In reality, it is impossible to neglect the effect of the surface reflection. The momentum change by the light reflected back from the surface of the particle will generate a force to push the particle forward. For a stable trap, this force is cancelled by the scattering force. If the pushing force is larger than the scattering force, the particle

will be pushed away from the focus and thus can not be stably trapped. The reflectance depends on the ratio $m = n_{particle} / n_{medium}$ between the relative refractive index of the microsphere and the surrounding medium. Larger *m* implies more surface refection, larger pushing force and thus more difficulty in trapping. To increase the scattering force, higher numerical aperture lens should be used.

4.1.2.2 Rayleigh Approximation

When the trapped particle is much smaller than the wavelength of the trapping laser, the conditions for Raleigh scattering are satisfied and the particle can be treated as a dipole. In this regime, the scattering and gradient forces are separated. The optical forces can be calculated analytically with Rayleigh scattering theory [115, 123]. The scattering force is due to absorption and radiation of light by the dipole. We consider a nano-particle with radius *r* and a relative index *m* ($m = n_{particle} / n_{medium}$). The force is

$$\vec{F}_{\text{scat}} = \frac{128\pi^5 r^6}{3c\lambda_0^4}\left(\frac{m^2-1}{m^2+2}\right)^2 n_{\text{medium}}^5 \vec{I} \tag{4.2}$$

where $\vec{I}$ is the intensity of the incident light, c is the speed of light in vacuum, λ_0 is the wavelength of the trapping laser. From the Eq. (4.2), we can find that the scattering force is in the direction of the propagation of the incident light and is proportional to the intensity. The time average gradient force on the particle:

$$\vec{F}_{\text{grad}} = (\vec{p}\cdot\nabla)\vec{E} = \frac{2\pi n_{\text{medium}} r^3}{c}\left(\frac{m^2-1}{m^2+1}\right)\nabla I \tag{4.3}$$

where $\vec{p}$ is the induced dipole of the particle.

From equation (4.2), we can obtain the trapping potential formed by the gradient force:

$$V = -\frac{2\pi n_{\text{medium}} r^3}{c}\left(\frac{m^2 - 1}{m^2 + 1}\right) I \tag{4.4}$$

Therefore, the total force generated by the light on the particle is the sum of scattering force and the gradient force. When the particle is stably trapping at the focus, the net force is zero. To form a stable trap, the net force and the displacement of the particle from the focus should have opposite signs. From equation (4.2) and (4.3), we could find the scattering force is proportional to r^6 while the gradient force is proportional to r^3. The scattering force decreases much faster than the gradient force with the decreasing of the size of the particle.

The stability condition on the dominance of the backward axial gradient force is independent of power and therefore there is another condition for Rayleigh trapping. Another trapping condition is that the potential well depth should be at least ten times larger than the average kinetic energy of the particles [115]. As was previously point out, the particles have Brownian motion because of the kinetic energy. To stably trap a particle, the time to pull a particle into the trap should be much less than the time for the particle to diffuse out of the trap by Brownian motion. Due to the fact that the kinetic energy of a particle follows the Maxwell Boltzmann distribution at thermal equilibrium, the particle has a probability that its instantaneous kinetic energy is much larger than its average kinetic energy. Only if the potential well depth is much larger than the kinetic energy of the particle, we have large chance to pull the particle to the trapping spot.

Also the kinetic energy of particle is independent of the size, but the potential is proportional to r^3. Therefore it is very hard to trap small size particles.

4.3 Surface Plasmonic Tweezers

To increase the potential well depth, we can simply increase the power of the laser. However, this method will not increase the gradient force at all; also too much power may damage the particle. In order to trap small size particles tightly, two factors should be considered: first, there should be enough power work on the particle (potential well depth ten times larger than kinetic energy of the particle); second, the "shape" of this potential well which determines the gradient force should be sharp. As introduced in chapter 2, surface plasmon has two main characters: surface field localization and local field enhancement, which is perfect for small particle trapping.

In the early 1990s, people have proposed to use evanescent fields for optical trapping [124-128]. Experimental research on surface plasmon-based trapping was started by two pioneering experiments which study the enhanced force field at a homogeneous gold and water interface. In 2006, Garcés Chávez et al. reported the micron size dielectric beads were trapped on the region of a gold surface where the surface plasmon was generated [129]. In the same year, Volpe et al. probed the SP force field and measured the force magnitude by using photonic force microscopy [130].

The first experimental implementation of SP-based trapping was demonstrated by micro-sized gold disks coated on glass substrate [131, 132]. In the experiment, a

basic SP-structure has been used and the surface plasmon has been generated by Kretschmann configuration. There are no flow and convention in the polystyrene solution. The polystyrene beads have been pushed forward by the evanescent wave along the incident direction of the laser beam at the glass-water interface [131]. When the beams come to the position where SP field has maximum intensity, they get trapped. Similar to conventional optical trapping, this SP tweezers also generate scattering force and gradient force. When these two forces get balanced, the beads could be trapped stably. In this type of SP-trapping, both forces depend on the illumination direction and polarization of the laser beam. The magnitude of the scattering force increases as the angle decreases, meanwhile the gradient force is also controlled by the incident angle. Therefore, the trapping properties can be easily modified by changing the balance between the two forces. Another advantage of this SP-trapping is the trapping times of up to several hours can be achieved for an incident laser intensity of 10^7 W/m^2, which is about two orders smaller than the intensity required by the conventional optical tweezers.

Although this simple Kretschmann configuration golden disks based surface plasmon tweezers has advantages: easy to control the trapping properties and lower incident laser power, it is very difficult to trap the beams whose size are smaller than 1 micron for the limits of the localized surface plasmon intensity and symmetry of this structure. Much higher control of surface plamonic fields can be achieved through plasmonic antenna structure. Due to the high localized and intense hot spots within the

gap region generated by the gap antenna, scientists recently have paid much attention for it. Grigorenko et al. first used gap antennas to assist conventional optical tweezers [133]. In the experiment, they used 1064 nm laser beam to illuminate the gold cylinders and 200 nm polystyrene beads have been trapped in the antenna hot spot. The trapping volume is beyond the diffraction.

After the work of Grigorenko et al., different surface plasmonic antennas were designed and used for optical tweezers. However, the SP resonances lead to local heating of the metal and heat dissipation to the surrounding fluid. These thermal effects will result in convection, thermophoresis and even higher intensity may cause heat damage to the trapping specimen. Therefore more trapping mechanisms need to be exploited. The power of conventional optical tweezers is usually dependent on the average kinetic energy of the particle and no modifications are applied to the potential well during the trapping process. Although the average kinetic energy of the particle within the trap is given by $3/2kT$, the instantaneous velocity follows a Maxwell–Boltzmann distribution, in which the energy can occasionally significantly exceed the average value. Therefore the potential depths usually are ten times higher than the average kinetic energy of the particle to compensate for the occasionally high energy events. Without the high energy cases, a depth of $3/2kT$ well will be enough to hold the particle. If a feedback system is introduced to recognize and reconfigure the potential well to compensate the high energy events, the power of the tweezers will be significantly reduced. Theoretically, the feedback system is used to control the trapping

potential by adjusting the laser intensity or the trap position. In practice, the feedback system can increase the effective stiffness of the trap [134], producing a force clamp [135] and allowing the object to be further confined by adding an external source of damping [136]. In order to trap single gold nanoparticles within the gap of a gold antenna, a feedback system has been used to control the potential by monitoring the antenna resonance shift. This work is reported done by Zhang and co-workers [137].

Owing to the advantage in small size particles trapping, SP tweezers have a lot of application in bioscience. Also SP tweezers may play a key role in the development of future integrated analytical platforms. In atom physics and quantum information, SP tweezers could be an important tool and strong benefit the research based on cold neutral atoms.

4.4 Sample Design

The principle of fiber optical trap is the same as free space optical trapping, but with the Gaussian laser beam delivered through an optical fiber. If a spatial phase mask (for example) lens is mounded on the end of the optical fiber, the Gaussian beam will be focused at some distance from the fiber tip. Since the size of the single mode fiber core is very small (usually less than 10 microns, depends on the wavelength), it is very difficult to fabricate the high numerical aperture micro-lens and integrated on the fiber tip. Therefore, it is very difficult to make a full 3D optical trap by a single mode optical fiber.

As we introduced in chapter 2, Surface plasmon polaritons are electromagnetic surface waves formed through strong interaction between electromagnetic field and free electron oscillations at a metal-dielectric interface. One unique property of the SPPs is their high confinement near the interface and intrinsically localized in a small volume. SPs focusing becomes one main application. This plasmon nanofocusing is typically achieved using tapered metallic guiding nanostructures such as tapered metal rods [138, 139], sharp metal wedges [140, 141] and the tapered nanogap between two metallic media [142]. Beyond these, conventional Fresnel zone plate (FZP) structures also have been used for nanofocusing: by fabricating a well designed Fresnel zone plate on the top of the fiber tip, and then a high numerical aperture micro-lens with a fiber can be made.

A conventional optical binary amplitude FZP consists of a series of concentric opaque and transparent ring-like zones, which can be used as either a lens or a reflector as illustrated in Fig. 4.3.

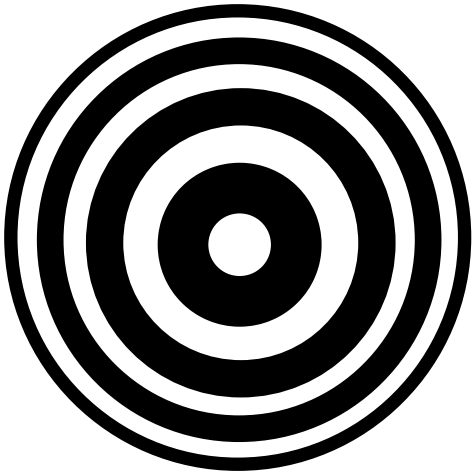

Figure 4.3 Illustration of a circular Fresnel zone plate

When used for lens, the energy collection is performed by the transparent zones for the transmission zoneplate. For our optical tweezers design, we used this function of the FZP. And the opaque zones can be used as the reflection zoneplate. But unlike lenses or reflection mirrors, FZP uses diffraction instead of refraction or reflection. Light illuminated on the zone plates will diffract from the opaque zones. The schematic of FZP is shown in Fig. 4.4. Constructive interference of SP fields is obtained at a focal distance f from the FZP when Fresnel zone radii ρ_m satisfy:

$$\rho_m = \sqrt{\frac{m^2\lambda^2}{4n^2} + \frac{m\lambda f}{n}} \tag{4.5}$$

where m is an integer (also called Fresnel zone number), λ is the wavelength of the light to be focused; f is the distance from the center of the zone plate to the focus, and n is the refractive index of the surrounding material.

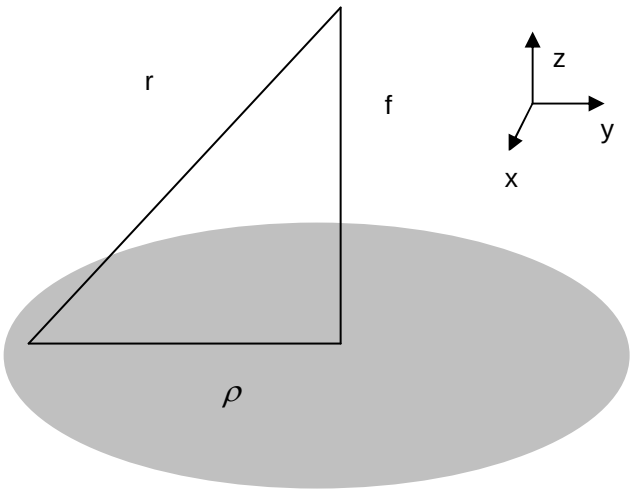

Figure 4.4. Schematic diagram of Fresnel zone plate.

Unlike the conventional zone plates made by metal film of Cr, Al or Ni, the plasmonic FZP is a device consisting of a quartz substrate coated with silver thin film. Our plasmonic FZP is made of single-mode fiber tip coated with silver thin film which is embedded with a zone plate structure. We use Corning SMF-28^{TM} 1550nm fiber to fabricate the optical tweezers. Since diameter of the core of this fiber is only 8.2 microns and the mode-field diameter is only about 10 microns [143], we can only fabricate two transparent Fresnel zones on the fiber tip.

The radii of the Fresnel zones designed for different surrounding materials are shown in Table 4.1. The focal length of this design is 2 microns.

Table 4.1. Parameters of our Fresnel Zone Plate Design in Water and Toluene.

ρ (μm) / m	Water (n=1.32)	Toluene (n=1.49)
1	1.64	1.53
2	2.46	2.29
3	3.19	2.95
4	3.86	3.56
5	4.51	4.14

First, we design a conventional Fresnel zone plate- alternative opaque and transparent half-wave zones. The structure of the design is shown in Fig. 4.4. The numerical computational analysis of the electromagnetic field is carried out using finite-difference and time-domain (FDTD) algorithm.

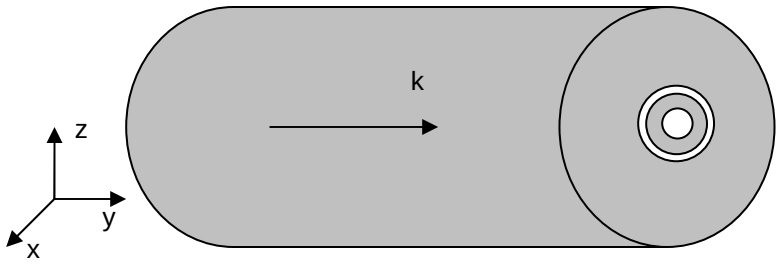

Figure 4.5. The first design of single mode fiber optical tweezers
by conventional Fresnel zone plate.

For our simulation, we use the commercial FDTD module named Fullwave (from Rsoft Company). A 350-nm-thick silver film is deposited on the end of the single-mode fiber. The core of the single mode fiber is 8 microns. The light propagates along z direction as shown in Fig. 4.5. The incident wave is circularly polarized and wavelength is 1550nm. Fig. 4.6 (a) and (b) show the refractive index profile of our plasmonic optical-tweezers design. The power of the incidental light is set to 1. In our 3D FDTD simulation, the time step and mesh size are 0.01fs and 50nm respectively. We also used non-uniform grid in the simulation. The perfectly matched layer boundary condition was applied at the computing domain boundaries.

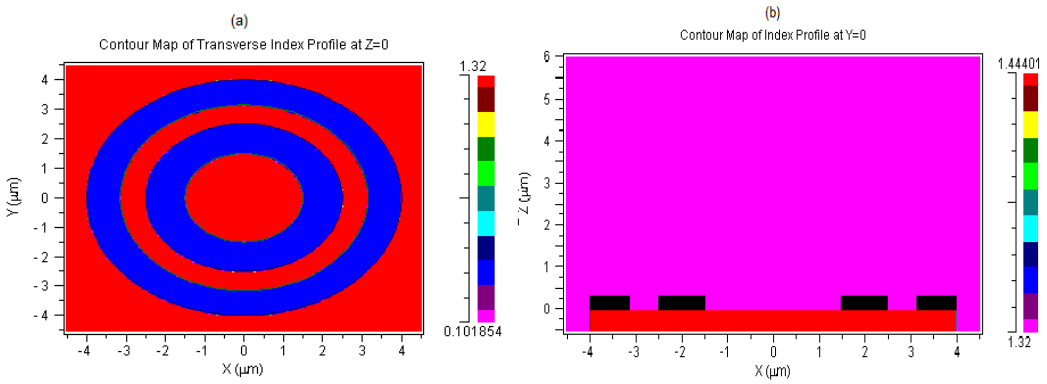

Figure 4.6. (a) Refractive index profile of the first design of plasmonic optical-tweezers in x-y plane. (b) Refractive index profile of the first design of plasmonic optical-tweezers in x-z plane.

Simulated intensity distribution of the first design of the Fresnel zone plate is shown in Fig. 4.7. In Fig. 4.7 (a), the simulation result shows the focal length of the tweezers is 2 μm, which is identical to our desired design. The maximum intensity is in the focus spot, which is about 7.35. The full wave half maximum (FWHM) of the intensity of the focal spot in x-direction is about 800nm and is close to the diffraction limit, whereas the FWHM of the intensity of the focal spot in z-direction is about 1.84 microns as illustrated in Fig. 4.7 (d). Therefore, the particle trapped by this optical tweezers should be more stable in x- and y-direction than in z-direction and displacements of the trapped particles in x and y-direction should be smaller than in z-direction.

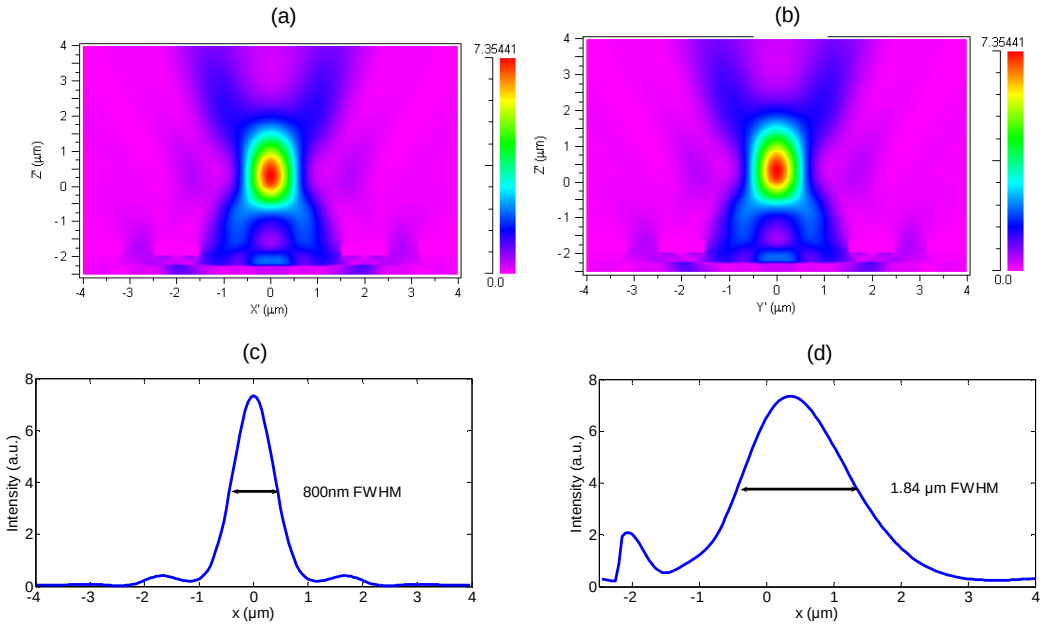

Figure 4.7. Intensity distributions of the first design. (a) in x-z plane (b) design in y-z plane, (c) The intensity profile of the focus spot in x-direction, (d) The intensity profile of the focus spot in z-direction.

Second, from the intensity distribution in Fig. 4.7, we notice that the light is well focused. Therefore, the potential well is formed for the particle to overcome the kinetic energy. However, to design an optical tweezers which can trap particle very stably and tightly, two factors should be considered and good potential well is only one of them. Another factor is the gradient force working on the particle should be larger than the scattering force. In our design, single mode optical fiber has been used. The light in the fiber is a Gaussian beam, and then most of the scattering force working on the particle should from the center of the first Fresnel zone (where intensity is higher). Therefore,

our second design is to block the central part of the Fresnel zone and reduce the scattering force, which is shown in Fig. 4.8.

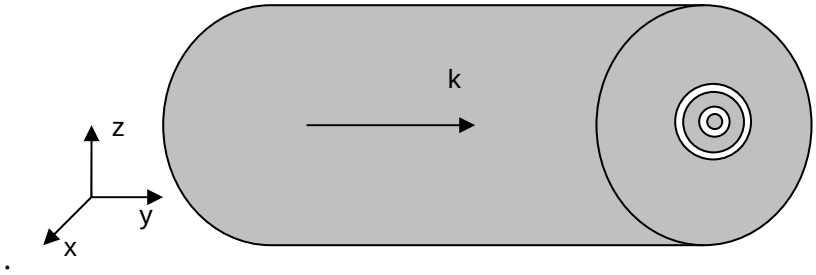

Figure 4.8. The second design of single mode fiber optical tweezers
by conventional Fresnel zone plate.

Simulated intensity distribution of the second design of the Fresnel zone plate is shown in Fig. 4.9. In Fig. 4.9 (a), the simulation result shows the focal length of the tweezers to be $2\,\mu m$, which is identical to our desired design. The maximum intensity is in the focal spot, which is about 7.96. The full wave half maximum (FWHM) of the intensity of the focal spot in x-direction is about 800nm and is close to the diffraction limit whereas the FWHM of the intensity of the focal spot in z-direction is about 2.15 microns. The intensity distribution of the second design is very similar to the first one. Surprisingly, the maximum intensity in the focal spot is even higher.

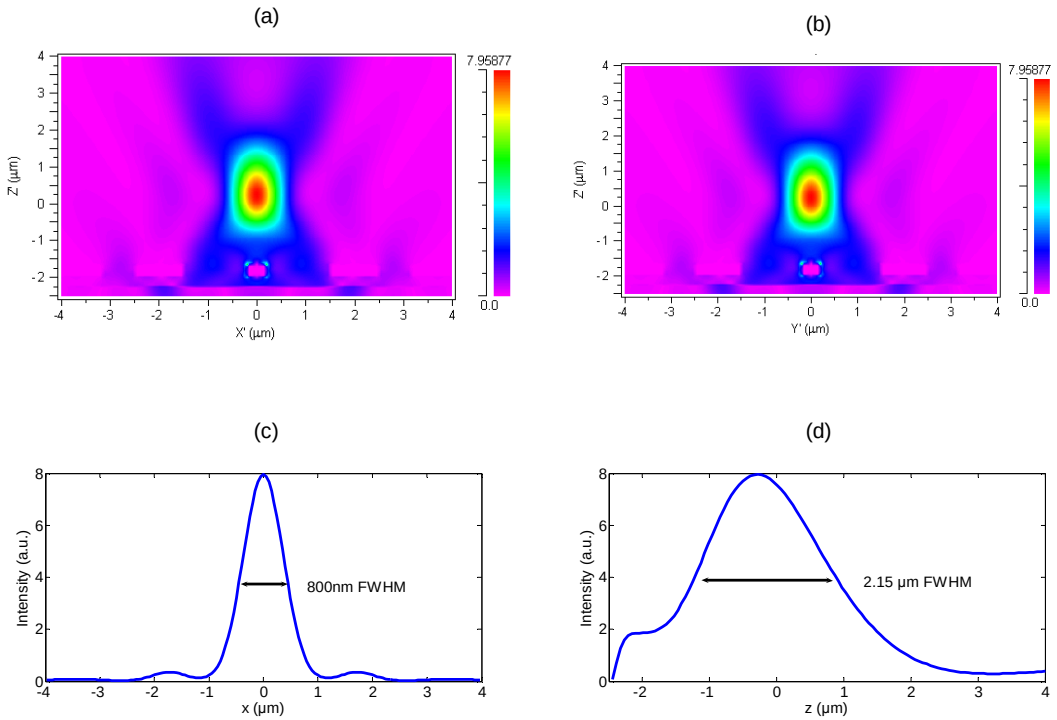

Figure 4.9. Intensity distribution of the second design. (a) in x-z plane, (b) in y-z plane. (c) The intensity profile of the focal spot in x-direction, (d) The intensity profile of the focal spot in z-direction.

Although the simple Fresnel zone plate antenna with alternative opaque and transparent half-wave zones is easy to fabricate, there are some issues of this simple design that we found in the measurement. First of all, it is hard for the particles to reach the focal spot because of the scattering light from the second transparent ring (the third Fresnel zone). Secondly, some particles will be trapped in the second transparent ring (details can be found in the measurement part). To avoid these issues, we design the third structure by the subzone technique. The essence of the subzone technique is to divide each full wave zone into several finer subzones. Our design is eight cutting-through concentric rings, whose refractive index contour images are shown in Fig. 4.10.

The first five rings are location in the first Fresnel zone (m=1), and the sixth, seventh and eighth rings are located in the third Fresnel zone (m=3).

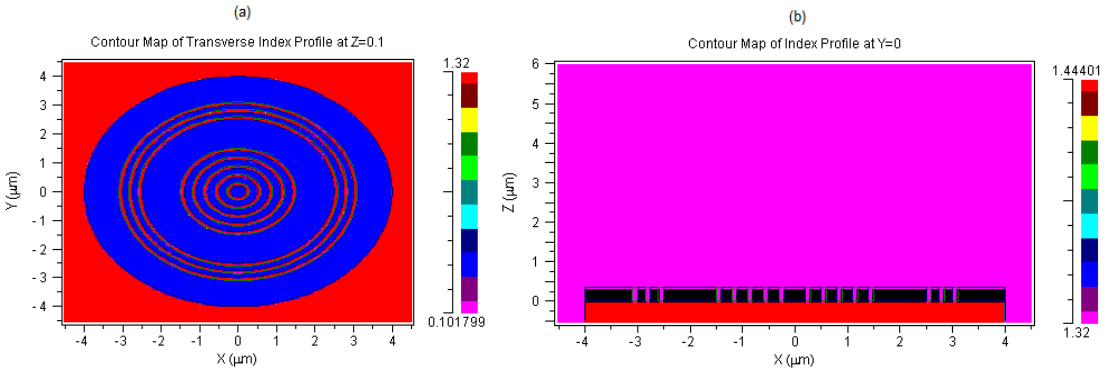

Figure 4.10. (a) Refractive index profile of the subzone design of plasmonic optical-tweezers in x-y plane. (b) Refractive index profile of the subzone design of plasmonic optical-tweezers in x-z plane.

Simulated intensity distribution of our subzone design of the Fresnel zone plate is shown in Fig. 4.11. Compared to the first two designs, the maximum intensity is much lower in the focal spot, which is about 1.25. The full wave half maximum (FWHM) of the intensity of the focal spot in x-direction is about 800nm and is close to the diffraction limit, whereas and the FWHM of the intensity of the focal spot in z-direction is about 1.6 microns.

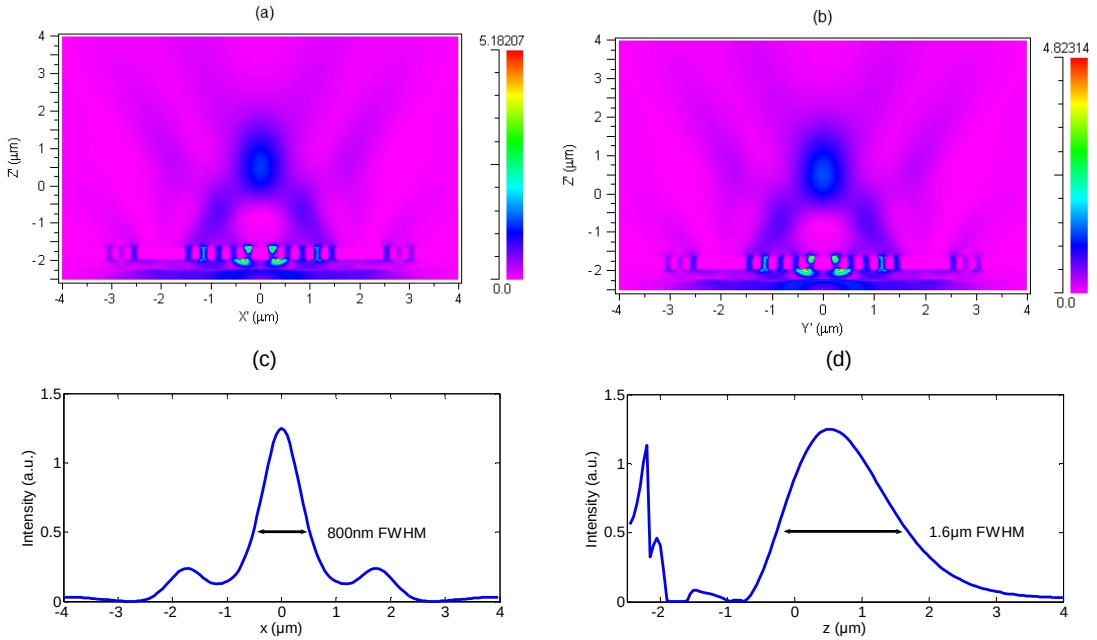

Figure 4.11. Intensity distribution of the subzone design (a) in x-z plane, (b) in y-z plane. (c) the intensity profile of the focus spot in x-direction, (d) the intensity profile of the focus spot in z-direction.

4.5 Sample Fabrication and Experimental Setup

The single-mode-fiber based plasmonic optical tweezers fabrication processes are shown in Table 4.2.

Table 4.2 Fabrication Processes of the Single Mode Fiber based Plasmonic Optical Tweezers

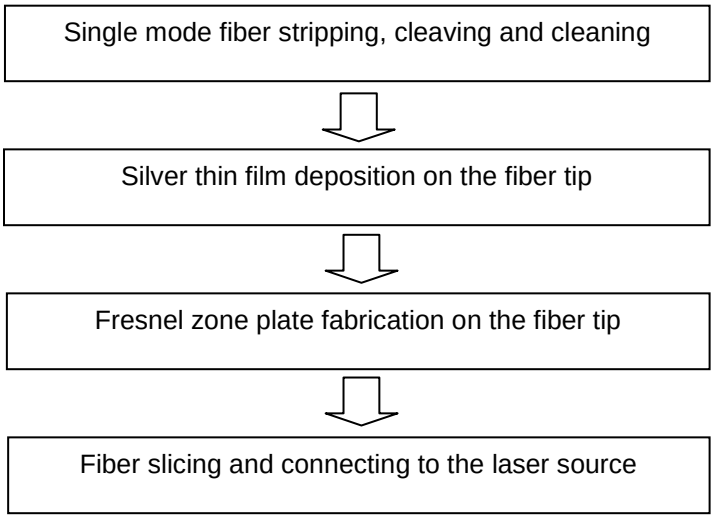

- Step 1: Optical fiber stripping, cleaving and cleaning.

Stripping and cleaving are the standard fiber

- Step 2: Silver thin film deposition on the fiber tip

We used thermal evaporator system to deposit the thin film on the tip of fiber. The fiber is taped on the surface of the holder by vacuum tape, and the tip is facing to the source shown in Fig. 4.12. To make the film uniform, we rotate the substrate. One needs to pay attention to is the fact that the value read from the thickness monitor is not accurate, because the distance between the fiber tip and the source is different from the one between the holder and the source. The fiber tip is closer to the silver bowl.

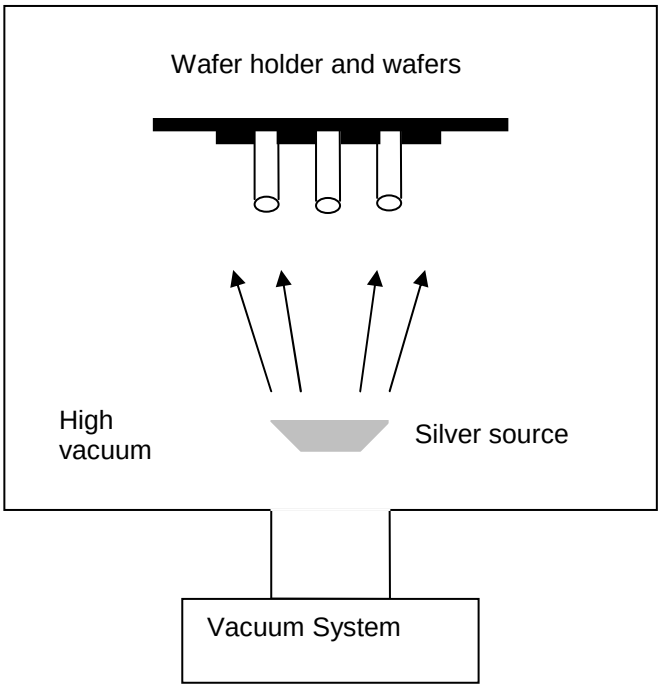

Figure 4.12. Thermal evaporation system for the silver thin film deposition on the fiber tip.

- Step 3: Fresnel zone plate fabrication on the fiber tip

The zone plate fabrication is done by the FIB. There are two main differences from the regular sample fabrication by FIB. First of all, the optical fiber needs to be taped on the stage very tightly. Second, in order to fabricate the structure exactly on the core of the fiber, the marks are needed.

To make the fiber tip coaxial with to the ion beam, we use the SEM tape to fix the fiber on a 45-degree tilt sample stage and then tilt the stage 9 degree as illustrated in Fig. 4.13. After the fiber is taped on the stage, the SEM tape is pressed by tweezers multiple times to make the fiber and tape contact tightly. This press

process will make the fiber tip very stable, with no shaking and moving during FIB milling.

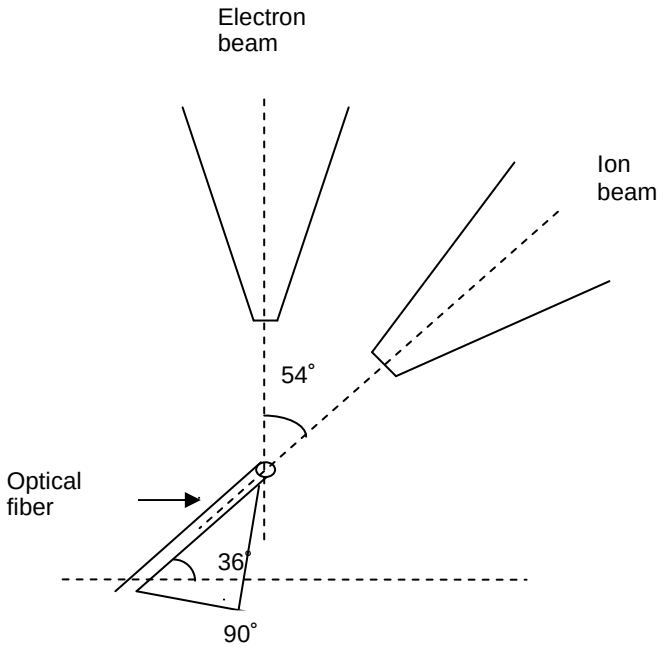

Figure 4.13. Schematic diagram of the fiber in FIB camber.

In order to fabricate the structure on the core of the fiber, we mill two marks which are 7 microns away from the center point of the fiber shown in Fig. 4.14. The reason to choose 7 microns is: 7 microns is bigger than the radius 4 microns of the core of the single mode optical fiber, but not too far away from the center point. Therefore the marks will not be on the core of the fiber and then they will not affect the light radiation pattern; and also they are not far away from the center point which will provide a high accuracy of the alignment.

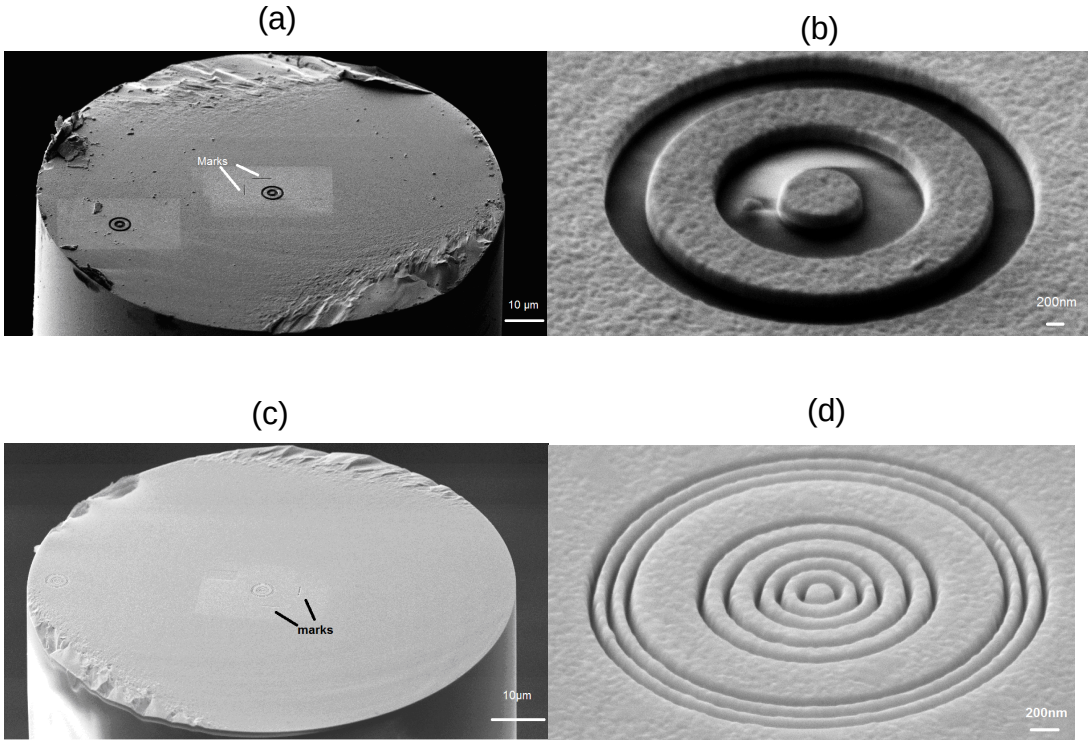

Figure 4.14. SEM images of the second design and third design.
(a) and (b) SEM images of the second design
(c) and (d) SEM images of the third design

- Step 4: Fiber slicing and connecting to the laser source

We splice the sample and an APC-connectorized patch cord, and then connect it to a laser source. This laser system has a semiconductor laser, a circulator and a high-power EDFA as shown in Fig. 4.15. Since there is a strong reflection in our design, we put an optical circulator to protect the EDFA and the laser. The reflected light that comes back to the circulator will be absorbed by a 30dB attenuator.

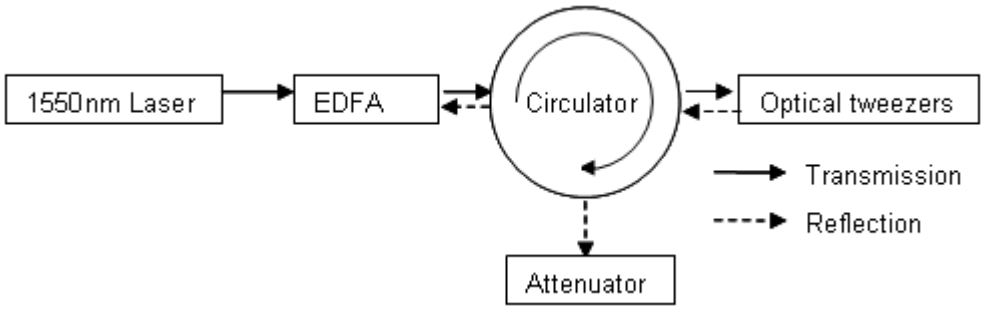

Figure 4.15. Schematic of the optical tweezers and the laser system.

To demonstrate the action of nanometric optical tweezers, solid silicon dioxide beads are used as shown in Fig. 4.16 (a). In the experiments, 1 micron size silicon dioxide spheres are diluted into perfusion chambers made by assembling two coverslips with vacuum grease shown in Fig. 4.16 (b).

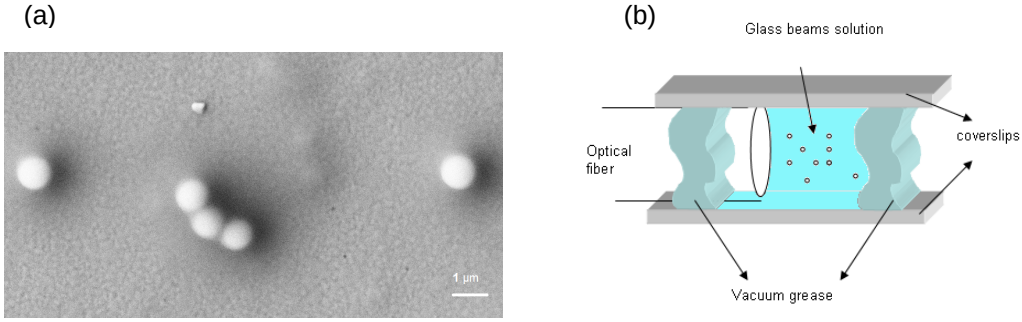

Figure 4.16. (a) SEM image of the 1 micron silicon dioxide beads on a silver thin film. (b) Cross section of the optical tweezers in the chamber filled with micro-beams water solution.

The experimental set-up is shown in Fig. 4.17. In our experiment, the optical tweezers sample is mounted on a three-dimensional mechanical translation stage. The HBO 100 illuminator (from Carl Zeiss) is used to illuminate the sample.

The light is collected by a Carl Zeiss N-Achroplan 63x/0.95 dry objective lens. The trapping action images and videos are studied by a Canon EOS 5D II camera.

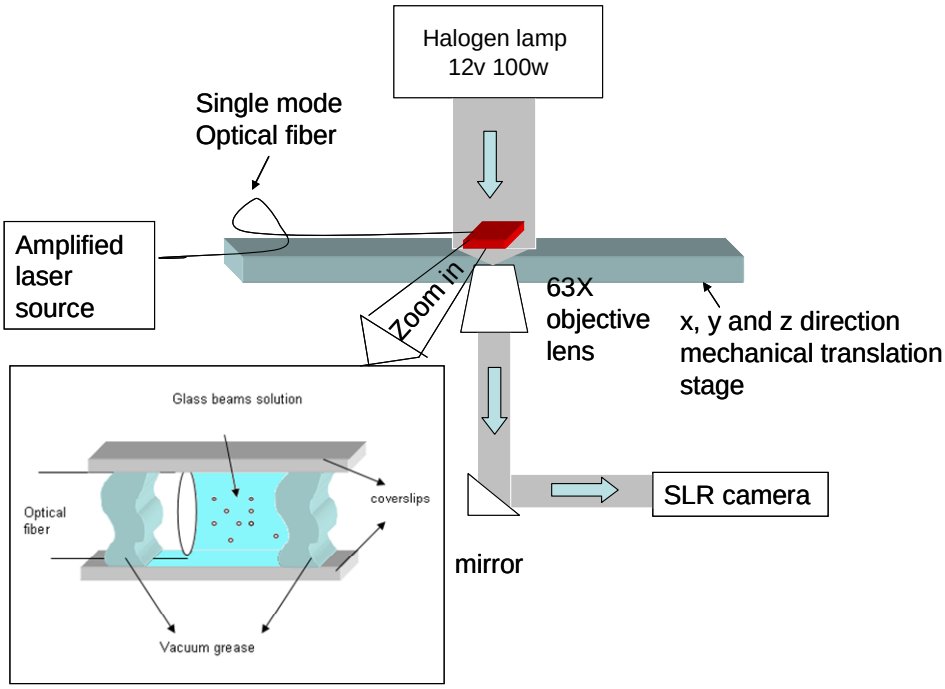

Figure 4.17. Experimental set-up.

To analyze the optical trapping properties, it is necessary to measure displacements of objects in the optical trap, and then some position detectors will need to be used. There are several methods to do this displacement detection.

- Imaging methods

The most intuitive detection methods simply use the image of the trapped bead. These methods use conventional bright-field or phase microscopy to produce an image that is cast onto an electronic detector. The output of this detector is then processed to produce a position signal in two dimensions. The chief difference between methods lies in the type of detector used. This can be a “scanning” type of

sensor such as a CCD in which pixels or image elements are accessed sequentially to produce a video; or it may be a multi-segment or position-sensitive photodiode type of sensor where a continuous analogue signal is produced. The latter type of detector generally provides higher bandwidth. A compromise type of detector could be the linear array type of CCD or photodiode which might be ideal for multiple bead applications.

- Quadrant photodiode detector

In this method, multi-element (quad cell) photodiodes are used, which consist of several separate active areas. Within a certain range of light intensities, the output voltage of a photodiode scales linearly with the intensity of light incident upon the diode. The light incident upon each quadrant in the QPD generates a voltage. The analog circuitry then outputs a voltage V_x and V_y which are proportional to the actual x and y position of the incident beam. As the light scatters in a predictable way off of the spherical beads, this information can be used to recover actual bead position within a narrow range around the center of the trap. With nothing in the trap (or a trapped bead exactly centered in the trap), the laser beam is tightly focused on the center of the QPD, giving V_x and V_y signals of zero. When a trapped bead moves slightly away from the trapping center, the laser spot moves on the QPD causing V_x and V_y to vary accordingly.

Although Quadrant photodiode detector provides fast detecting speed and high accuracy, it is very hard to do the alignment for your design because of the

reflection and scattering from the fiber tip. We selected the imaging method with a CMOS video camera to exploit the displacement of the trapping particles. In our experiment, the image size of the video is 1920□1080 and the frame rate is 30Hz. First, we record the video and then convert the video into images (30 images per second). After we obtain the images, we track the locations of the trapping particle for each image by imaging processing method. From the distributions of the displacements, we can evaluate the trapping length scale.

4.6 Results and Discussion

In this section, we present our experimental implementations of the single-mode-fiber based plasmonic optical trapping by the second design. Fig. 4.18 shows the main experimental result of this chapter-optical trapping of 1 micron beads near the surface of single mode fiber tip in three dimensions. The threshold of trapping power of the laser is 60mw. At t=0s, the bead shown in Fig. 4.18 (a) is trapped in the center of the core of the fiber end. It seems as if a pair of beads is trapped, however, the one on left side is the bead which is trapped and the right one is the reflection of the bead from the silver thin film on the end of the fiber. At t=10s when we turn off the laser, the bead is released from the trapping as shown in Fig. 4.18 (b). Several seconds later, we turn on the laser and then another bead is coming to the focus spot of the Fresnel zone plate as shown in Fig. 4.18 (c). At t=24s, this bead is trapped by the laser as illustrated in Fig. 4.18 (d).

(a)

(b)

(c)

(d)

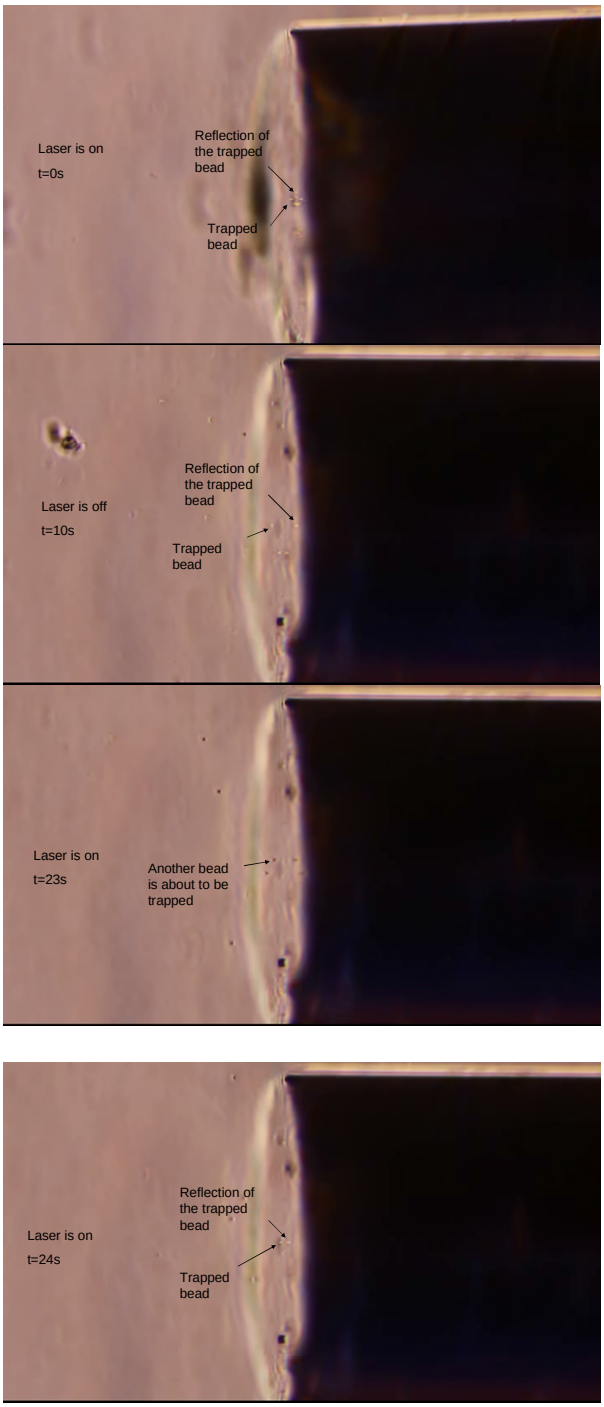

Figure 4.18. Time lapse frames of beads sorting by trapping and releasing.

In Fig. 4.19 (a), the image illustrates the position of a bead trapped by 120mw laser measured at different times with a 30 frames per second video. Fig. 4.19 (b) and (c) are the histograms of particle displacement for the trapping bead. The FWHM of the Gaussian distribution of displacements of the bead at this power in x-direction is 600nm and in z-direction is about 300nm, which are in agreement with our simulation design. Our simulation results show that the FWHM of the power of the focal spot in z-direction is about twice as big as the spot in x-direction. Therefore, the confinement of the tweezers in z-direction should be much weaker than in x-direction.

(a)

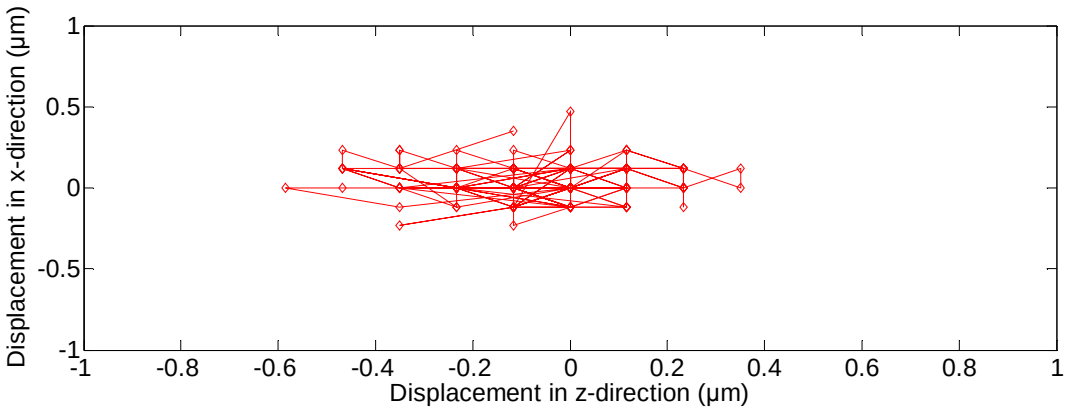

(b)

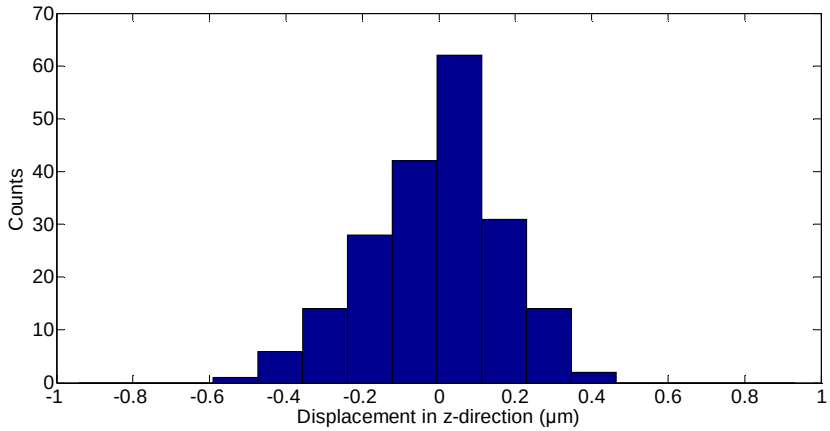

(c)

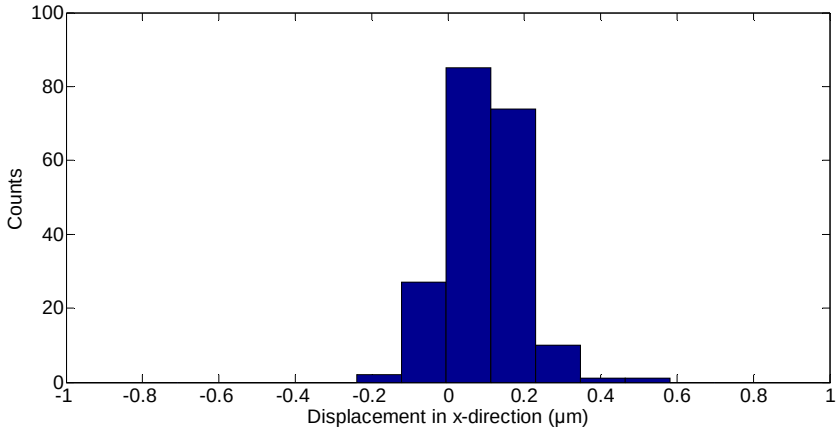

Figure 4.19. Displacements of the bead trapped under 120mw power. (a) The position of a 1-micron trapped bead in the first 200 frames, (b) histogram of the trapped bead displacement in x-direction, (c) histogram of the trapped bead displacement in z-direction.

4.7 Conclusion and Outlook

In this chapter, we have demonstrated a subwavelength optical trapping by single-mode optical-fiber-based plasmonic tweezers system. The proposed tweezers provide a subwavelength trapping volume for the trapping nanoparticles and open new exciting possibilities in different fields of physics and bioscience. This system could be easily operated and integrated with other experiments.

The future work of this tweezers system is to exploit the trapping limit and find the smallest-size particle that could be trapped. Beyond the 3D trapping, this system has potentials to also rotate the particle by using orbital angular momentum of light.

CHAPTER 5

CONCLUSION AND PROSPECTS

Conclusion

The main achievements of this thesis can be summarized as follows:

- Shaping spontaneous emission pattern by plasmonic nanocavity

We have demonstrated narrowing of the far-field fluorescence pattern from a quantum dot positioned inside a rectangular (slit) nanoaperture surrounded by periodic corrugations. Most (80%) of the emerging spontaneous emission is concentrated in a beam with angular half-width at half-maximum of ~10°. This indicates the potential for using such a corrugated nanostructure for efficient coupling into and out of the slit metal nanocavities designed for enhancement of nonlinear- and quantum-optical effects

- Spontaneous decay of CdSe / ZnS core-shell quantum dots at the air-dielectric interface

We have demonstrated that the spontaneous emission lifetime of a quantum dot can be significantly reduced by placing it at the interface between air and a dielectric medium. Higher refractive index of the dielectric leads to shorter lifetimes. The distance from the quantum dot to the interface plays an important role in limiting the amount of

this reduction at high refractive indices. With proper placing of the quantum dot with respect to the dielectric, sub-nanosecond lifetimes could be achieved.

- Single mode fiber-based surface plasmonic optical tweezers

We designed a new type of optical tweezers □□□ single-mode-fiber-based surface plasmonic optical tweezers. The subwavelength three dimension optical trapping has been achieved using one standard single-mode optical fiber for the first time to our knowledge. The threshold trapping power of the laser is 60mw.

Future prospects

The main issue of the single-photon emitter made by integrating single quantum dot into a plasmonic nano-cavity is the huge loss, which will decrease the efficiency of the emitter. However, the small volume and radiation direction control are two great advantages of such an emitter. The design of plasmonic nano-cavity structures with low loss (high Q) is therefore an important future direction.

In the long term, we want to develop a full quantum network system made of single quantum dot in plasmonic nano-cavity, communicating via the exchange of single photons through optical fiber.

Conventional optical tweezers can trap a single quantum dot. We hope that, with some enhancements our single-mode-fiber-based plasmonic tweezers can trap single quantum dot. This fiber-based optical tweezers are easy to operate, which opens this

technology to other fields, in particular, more applications in bioscience should be exploited.

REFERENCES

[1] Gilbert N. Lewis, “The conservation of photons,” Nature. 118, 874–875 (1926).

[2] S. Wiesner, “Conjugate coding,” ACM SIGACT news, 15, 78-88 (1983)

[3] C. H. Bennet, F. Bessette, G. Brassard, L. Salvail and J. Smolin, “Experimental Quantum Cryptography,” J. Cryptology, 5, 3-28 (1992)

[4] Andrew. J. Shields, “Semiconductor quantum light sources,” Nature Photon. 1, 215 (2007).

[5] J. Kim, O. Benson, H. Kan, and Y. Yamamoto, “A single-photon turnstile device,” Nature 397, 500-503 (1999).

[6] F. D. Martini, G. D. Giuseppe, and M. Marrocco, “Single-mode generation of quantum photon states by excited single molecules in a microcavity trap”Phys. Rev. Lett. 76, 900 (1996).

[7] C. Brunel, B. Lounis, P. Tamarat, and M. Orrit, “Triggered source of single photons based on controlled single molecule fluorescence,” Phys. Rev. Lett. 83, 2722 (1999).

[8] B. Lounis and W. E. Moerner, “Single photons on demand from a single molecule at room temperature,” Nature, 407, 491 (2000).

[9] A. Kuhn, M. Hennrich, and G. Rempe, “Deterministic single-photon source for distributed quantum networking,” Phys. Rev. Lett. 89, 067901 (2002).

[10] B. B. Blinov, D. L. Moehring, L.-M. Duan, and C. Monroe, "Observation of entanglement between a single trapped atom and a single photon,"Nature, 428, 153 (2004).

[11] C. Kurtsiefer, S. Mayer, P. Zarda, and H. Weinfurter, "Stable solid-state source of single photons," Phys. Rev. Lett. 85, 290 (2000).

[12] A. Beveratos, R. Brouri, T. Gacoin, J.-P. Poizat, and P. Grangier, "Nonclassical radiation from diamond nanocrystals," Phys. Rev. A 64, 061802 (2001).

[13] B. Lounis and M. Orrit, "Single-photon sources," Rep. Prog. Phys. 68, 1129 (2005).

[14] E. Moreau, I. Robert, J. M. Gérard, I. Abram, L. Manin, and V. Thierry-Mieg, "Single-mode solid-state single photon sources based on isolated quantum dots in pillar microcavities," Appl. Phys. Lett. 79, 2865–2867 (2001).

[15] Solomon, G. S., Pelton, M. & Yamamoto, Y. "Single-mode spontaneous emission from a single quantum dot in a three-dimensional microcavity," Phys. Rev. Lett. 86, 3903–3906 (2001).

[16] C. Santori, D. Fattal, J. Vuckovic´, G. S. Solomon, and Y. Yamamoto, "Indistinguishable photons from a single-photon device," Nature, 419, 594-597, (2002).

[17] M. A. Reed, J. N. Randall, R. J. Aggarwal, R. J. Matyi, T. M. Moore and A. E. Wetsel, "Observation of discrete electronic states in a zero-dimensional semiconductor nanostructure," Phys Rev Lett 60, 535–537 (1988).

[18] C. B. Murray, C. R. Kagan and M. G. Bawendi, “Synthesis and Characterization of Monodisperse Nancrystals and Close-packed Nanocrystals Assemblies,” Annual Review of Materials Science, 30, 545-610 (2000)

[19] E. M. Purcell, H. C. Torrey and R. V. Pound, “Resonance Absorption by Nuclear Magnetic Moments in a Solid” Phys. Rev. 69, 37-38 (1946).

[20] M. Pelton, C. Santori, J. Vuckovic, B. Zhang, G. Solomon, J. Plant, and Y. Yamamoto, “Efficient Source of Single Photons: A Single Quantum Dot in a Micropost Microcavity,” Phys. Rev. Lett. 89, 233602 (2002).

[21] A. Kress, F. Hofbauer, N. Reinelt, M. Kaniber, H. Krenner, R. Meyer, G. Bohm, and J. Finley, “Manipulation of the spontaneous emission dynamics of quantum dots in two-dimensional photonic crystals,” Phys. Rev. B 71, 241304(R) (2005).

[22] D. K. Armani, T. J. Kippenberg, S. M. Spillane and K. J. Vahala “Ultra-high-Q toroid microcavity on a chip,” nature, 421, 925-929, (2003).

[23] D. Press, S. Goetzinger, S. Reitzenstein, C. Hofmann, A. Loeffler, M. Kamp, A. Forchel, and Y. Yamamoto, “Photon antibunching from a single quantum-dot-microcavity system in the strong coupling regime,” Phys. Rev. Lett. 98, 117402 (2007).

[24] S. A. Maier, and H. A. Atwater, “Plasmonics: Localization and guiding of electromagnetic energy in metal/dielectric structures,” J. Appl. Phys. 98, 011101 (2005).

[25] W. L. Barnes, “Surface plasmon–polariton length scales: A route to subwavelength optics,” J. Opt. A, 8, 87–93 (2006).

[26] T. W. Ebbesen, C. Genet, and S. I. Bozhevolnyi, “Surface-plasmon circuitry,” Phys. Today 61, 44–50 (2008).

[27] A. Liebsch, “Screening properties of a metal surface at low frequencies and finite wave vectors,” Phys. Rev. Lett. 54, 67–70 (1985).

[28] I. A. Larkin, M. I. Stockman, M. Achermann, and V. I. Klimov, “Dipolar emitters at nanoscale proximity of metal surfaces: Giant enhancement of relaxation in microscopic theory,” Phys. Rev B 69, 121403 (2004).

[29] T. SΦndergaard, and S. Bozhevolnyi, “Slow-plasmon resonant nanostructures: Scattering and field enhancements,” Phys. Rev. B 75, 073402 (2007).

[30] L. Zhu, M. Annamalai, N. Stelmakh, and M. Vasilyev, “Shaping spontaneous emission from a single quantum dot into a narrow beam pattern,” International Quantum Electronics Conference, Baltimore, MD, May 31–June 5, 2009, post-deadline paper IPDB4.

[31] L. Zhu, S. Samudrala, N. M. Stelmakh, and M. Vasilyev, “Transmission Characteristics of Silver Nano-Apertures,” Frontiers in Optics / Laser Science XXVI conference, October 24–28, 2010, Rochester, NY, paper JWA34.

[32] A. J. Shields, “Semiconductor quantum light sources,” Nat. Photonics 1(4), 215–223 (2007).

[33] M. D. Leistikow, J. Johansen, A. J. Kettelarij, P. Lodahl, and W. L. Vos, “Size-dependent oscillator strength and quantum efficiency of CdSe quantum dots controlled via the local density of states,” Phys. Rev. B 79(4), 045301 (2009).

[34] Y. C. Jun, R. Pala, and M. L. Brongersma, “Strong modification of quantum dot spontaneous emission via gap plasmon coupling in metal nanoslits,” J. Phys. Chem. C 114(16), 7269–7273 (2010).

[35] J.-Y. Zhang, X.-Y. Wang, and M. Xiao, “Modification of spontaneous emission from CdSe/CdS quantum dots in the presence of a semiconductor interface,” Opt. Lett. 27(14), 1253–1255 (2002).

[36] X. Brokmann, L. Coolen, M. Dahan, and J. P. Hermier, “Measurement of the radiative and nonradiative decay rates of single CdSe nanocrystals through a controlled modification of their spontaneous emission,” Phys. Rev. Lett. 93(10), 107403 (2004).

[37] K. Liu, T. A. Schmedake, K. Daneshvar, and R. Tsu, “Interaction of CdSe/ZnS quantum dots: among themselves and with matrices,” Microelectron. J. 38(6-7), 700–705 (2007).

[38] L. Zhu, S. Samudrala, N. Stelmakh, and M. Vasilyev, “Spontaneous decay of CdSe / ZnS core-shell quantum dots at the air-dielectric interface,” Opt. Express 20, pp. 3144–3151 (2012)

[39] Martin J. Klein, ‘‘Max Planck and the beginnings of the quantum theory,’’ Archive for History of Exact Sciences 1, 459–479 (1962),

[40] G.N. Lewis, "The conservation of photons," Nature 118 (2981): 874–875 (1926).

[41] R. Hanbury Brown and R. Q. Twiss, "A Test of a New Type of Stellar Interferometer on Sirius," Nature 178 (4541): 1046–1048 (1956).

[42] Roy J. Glauber, “The quantum theory of optical coherence,” Phys. Rev. 130, 2529–2539 (1963)

[43] H. J. Kimble, M. Dagenais, and L. Mandel “Photon antibunching in resonance fluorescence,” Phys. Rev. Lett. 39, 691–695 (1977)

[44] R. E. Slusher, L. W. Hollberg, B. Yurke, J. C. Mertz and J. F. Valley, “Observation of Squeezed States Generated by Four-Wave Mixing in an Optical Cavity,” Phys. Rev. Lett. 55, 2409–2412 (1985)

[45] Hong, C. K.; Ou, Z. Y. and Mandel, L. "Measurement of subpicosecond time intervals between two photons by interference," Phys. Rev. Lett. 59, 2044–2046 (1987).

[46] M. A. Rowe, D. Kielpinski, V. Meyer, C. A. Sackett, W. M. Itano, C. Monroe and D. J. Wineland, “Experimental violation of a bell’s inequality with efficient detection,” Nature, 409, 791-794, (2000)

[47] C. Bennett , F. Bessette , G. Brassard , L. Salvail and John Smolin “Experimental quantum cryptography,” Journal of Cryptology 5, 3-28, (1992)

[48] Q. A. Turchette, C. J. Hood, W. Lange, H. Mabuchi, and H. J. Kimble, “Measurement of conditional phase shifts for quantum logic,” Phys. Rev. Lett. 75, 4710–4713 (1995)

[49] M. H. Anderson, J. R. Ensher, M. R. Matthews, C. E. Wieman and E. A. Cornell, “Observation of Bose–Einstein Condensation in a Dilute Atomic Vapor,” Science 269, 198–201 (1995)

[50] C. Cohen-Tannoudji, J. Dupont-Roc, and G. Grynberg, “Photons and Atoms: Introduction to Quantum Electrodynamics” Wiley-Interscience, New York, (1997).

[51] "Technical Report on Quantum Cryptography Technology Experts Panel," Advanced Research and Development Activity (ARDA), 2004, see http://qist.lanl.gov.

[52] A. Ekert, N. Gisin, B. Huttner, H. Inamori, and H. Weinfurter, "The Physics of Quantum Information", edited by D. Bouwmeester, A. Ekert,and A. Zeilinger (Springer, Berlin, 2000).

[53] R. J. Glauber, "Coherent and incoherent states of the radiation field," Phys. Rev. 131, 2766 (1963).

[54] M. Fox, "quantum optics: an introduction," Oxford University Press (2006)

[55] D. Leonard, M. Krishnamurthy, C. M. Reaves, S. P. Denbaars, and P. M. Petroff, "Direct formation of quantum – sized dots from uniform coherent islands of InGaAs on GaAs surface," Appl. Phys. Lett. 63, 3203 (1993).

[56] H. Takesue, Y. Tokura, H. Fukuda, T. Tsuchizawa, T. Watanabe, K. Yamada, and S.I. Itabashi, Appl. Phys. Lett. 91, 201108 (2007).

[57] D. J. Norris, "Electronic structure in semiconductor nanocrystals: optical experiment" Chapter 2 in "nanocrystal quantum dots, second edition" editor: Victor I. Klimov, CRC Press (2009)

[58] B. O. Dabbousi, J. Rodriguez-Viejo, F. V. Mikulec, J. R. Heine, H. Mattoussi, R. Ober, K. F. Jensen, and M. G. Bawendi, "(CdSe)ZnS core-shell Quantum Dots: synthesis and characterization of a size series of Highly

Luminescent Nanocrystallites," The Journal of Physical Chemistry B, 101 9463-9475 (1997).

[59] Kittel, Charles, "Introduction to Solid State Physics (8th ed.)," Hoboken, NJ: John Wiley and Sons. ISBN 0-471-41526-X. (1996).

[60] http://en.wikipedia.org/wiki/File:Dispersion_Relationship.png

[61] E. Hecht, "Optics," Addison-Wesley, New York, (2002)

[62] J. Takahara, S. Yamagishi, H. Taki, A. Morimoto, and T. Kobayashi, "Guiding of a one-dimensional optical beam with nanometer diameter," Opt. Lett. 22, 475–477 (1997).

[63] K. V. Nerkararyan, "Superfocusing of a surface polariton in a wedge-like structure," Phys. Lett. A 237, 103–105 (1997).

[64] E. N. Economou, "Surface plasmons in thin films," Phys. Rev. 182, 539–554 (1969).

[65] J. J. Burke, G. I. Stegeman, and T. Tamir, "Surface-polariton-like waves guided by thin, lossy metal films," Phys. Rev B 33, 5186–5201 (1986).

[66] M. Quinten, A. Leitner, J. R. Krenn, and F. R. Aussenegg, "Electromagnetic energy transport via linear chains of silver nanoparticles," Opt. Lett. 23, 1331–1333 (1998).

[67] K. Tanaka, and M. Tanaka, "Simulations of nanometric optical circuits based on surface plasmon polariton gap waveguide," Appl. Phys. Lett. 82, 1158–1160 (2003).

[68] B. Wang, and G. P. Wang, “Surface plasmon polariton propagation in nanoscale metal gap waveguides,” Opt. Lett. 29, 1992–1994 (2004).

[69] K. Tanaka, M. Tanaka, and T. Sugiyama, “Simulation of practical nanometric optical circuits based on surface plasmon polariton gap waveguides,” Opt. Express 13, 256 266 (2005).

[70] L. Liu, Z. Han, and S. He, “Novel surface plasmon waveguide for high integration,” Opt. Express 13, 6645–6650 (2005).

[71] G. Veronis, and S. Fan, “Guided subwavelength plasmonic mode supported by a slot in a thin metal film,” Opt. Lett. 30, 3359–3361 (2005).

[72] D. F. P. Pile, T. Ogawa, D. K. Gramotnev, Y. Matsuzaki, K. C. Vernon, K. Yamaguchi, T. Okamoto, M. Haraguchi, and M. Fukui ”Two-dimensionally localized modes of a nanoscale gap plasmon waveguide,” Appl. Phys. Lett. 87, 261114 (2005).

[73] D. F. P. Pile, D. K. Gramotnev, R. F. Oulton, and X. Zhang, “On long-range plasmonic modes in metallic gaps,” Opt. Express 15, 13669–13674 (2007).

[74] A. D. Boardman, G. C. Aers, and R. Teshima, “Retarded edge modes of a parabolic wedge,” Phys. Rev. B 24, 5703–5712 (1981).

[75] D. F. P. Pile, T. Ogaw, D. K. Gramotnev, T. Okamoto, M. Haraguchi, M. Fukui, and S. Matsuo, “Theoretical and experimental investigation of strongly

localized plasmons on triangular metal wedges for subwavelength waveguiding," Appl. Phys. Lett. 87, 061106 (2005).

[76] A. Boltasseva, V. S. Volkov, R. B. Nielsen, E. Moreno, S. G. Rodrigo, and S. I. Bozhevolnyi, "Triangular metal wedges for subwavelength plasmon–polariton guiding at telecom wavelengths," Opt. Express 16, 5252–5260 (2008).

[77] E. Moreno, F. J. Garcia-Vidal, S. G. Rodrigo, L. Martin-Moreno and S. I Bozhevolnyi,. "Channel plasmon-polaritons: Modal shape, dispersion, and losses," Opt. Lett. 31, 3447–3449 (2006).

[78] M. Yan, and M. Qiu, "Guided plasmon polariton at 2D metal corners," J. Opt. Soc. Am. B 24, 2333–2342 (2007).

[79] I. V. Novikov and A. A. Maradudin, "Channel polaritons," Phys. Rev. B 66, 035403 (2002).

[80] D. F. P. Pile and D. K. Gramotnev, "Channel plasmon–polariton in a triangular groove on a metal surface," Opt. Lett. 29, 1069–1071 (2004).

[81] D. K. Gramotnev and D. F. P. Pile, "Single-mode subwavelength waveguide with channel plasmon–polaritons in triangular grooves on a metal surface," Appl. Phys. Lett. 85, 6323–6325 (2004).

[82] S. I. Bozhevolyni, V. S. Volkov, E. Devaux, and T. W. Ebbesen, "Channel plasmon–polariton guiding by subwavelength metal grooves," Phys. Rev. Lett. 95, 046802 (2005).

[83] R. F. Oulton, V. J. Sorger, D. A. Genov, D. F. P. Pile and X. Zhang, “A hybrid plasmonic waveguide for subwavelength confinement and long-range propagation,” Nature Photon. 2, 496–500 (2008).

[84] E. Verhagen, A. Polman, and L. K. Kuipers, “Nanofocusing in laterally tapered plasmonic waveguides,” Opt. Express 16, 45–57 (2008).

[85] D. K. Gramotnev, “Adiabatic nanofocusing of plasmons by sharp metallic grooves: Geometrical optics approach,” J. Appl. Phys. 98, 104302 (2005).

[86] H. J. Lezec, A. Degiron, E. Devaux, R. A. Linke, L. Martin-Moreno, F. J. Garcia-Vidal, T. W. Ebbesen, “Beaming Light from a Subwavelength Aperture,” Science, 297 820-822 (2002)

[87] S. Ramo, J. R. Whinnery, and T. Van Duzer, “Fields and waves in communication electronics,” 2nd ed., John Wiley & Sons, New York, 1984.

[88] L. Martín-Moreno, F. J. García-Vidal, H. J. Lezec, A. Degiron, and T. W. Ebbesen, “Theory of highly directional emission from a single subwavelength aperture surrounded by surface corrugations,” Phys. Rev. Lett. 90, 167401 (2003)

[89] M. Annamalai, “optimization of coupling from a sub-wavelength metal nanoaperture to a gaussian mode” Master thesis

[90] S. Reyntjens and R. Puers, “A review of focused ion beam applications in microsystem technology,” J. Micromech. Microeng. 11 287–300 (2001)

[91] Technical Specification of Quantum Dot Powder from ocean nanotech

[92] C. A. Leatherdale, W.-K. Woo, F. V. Mikulec, and M. G. Bawendi, “On the Absorption Cross Section of CdSe Nanocrystal Quantum Dots,” J. Phys. Chem. B, 106, 7619-7622 (2002)

[93] N. Stelmakh, “Harnessing multimode broad-Area laser-diode emission into a single-lobe diffraction-limited spot,” IEEE Photon. Technol. Lett. 19, 1392 (2007).

[94] Ch. Santori, M. Pelton, G. Solomon, Y. Dale, and Y. Yamamoto, “Triggered single photons from a quantum dot,” Phys. Rev. Lett. **86**, 1502 (2001).

[95] Ph. Grangier, B. Sanders, and J. Vuckovic, Eds., special issue “Focus on single photons on demand,” New J. Phys. **6**, issue 1, July 2004.

[96] S. G. Lukishova, L. J. Bissell, C. R. Stroud, and R. W. Boyd, “Room-temperature single photon sources with definite circular and linear polarizations,” Opt. and Spectroscopy **108**, 417 (2010).

[97] A. Efros, “Fine structure and polarization properties of band-edge excitons in semiconductor nanocrystals,” Ch. 3, *Nanocrystal Quantum Dots*, CRC press, 2e, (2010).

[98] X. Wang, X. Ren, K. Kahen, M. A. Hahn, M. Rajeswaran, S. Maccagnano-Zacher, J. Silcox, G. E. Cragg, A. L. Efros, and T. D. Krauss, “Non-blinking semiconductor nanocrystals,” Nature, **459**, 686 (2009).

[99] J. Hollingsworth and V. Klimov, "Soft chemical synthesis and manipulation of semiconductor nanocrystals," Ch. 1, *Nanocrystal Quantum Dots*, CRC press, 2e, (2010).

[100] Z. Jacob, I. Smolyaninov, and E. E. Narimanov, “Single photon gun: radiative decay engineering with metamaterials,” *International Quantum Electronics Conference*, Baltimore, MD, May 31–June 5, 2009, post-deadline paper IPDB2.

[101] Z. Jacob, J. Y. Kim, G. V. Naik, A. Boltasseva, E. E. Narimanov, and V. M. Shalaev, “Engineering photonic density of states using metamaterials,” Appl. Phys. B **100**, 215 (2010).

[102] S. M. Barnett, B. Huttner, R. Loudon, and R. Matloob, “Decay of exited atoms in absorbing dielectrics,” J. Phys. B **29**, 3763 (1996).

[103] M. D. Leistikow, J. Johansen, A. J. Kettelarij, P. Lodahl, and W. L. Vos, “Size-dependent oscillator strength and quantum efficiency of CdSe quantum dots controlled via the local density of states,” Phys. Rev. B **79**, 045301 (2009).

[104] The Quantum Theory of the Emission and Absorption of radiation P.A.M. Dirac Proc. R. Soc. Lond. A 114, 243-265 (1927)

[105] E. Yablonovich, T. J. Gmitter, and R. Bhat, “Inhibited and enhanced spontaneous emission from optically thin AlGaAs/GaAs double heterostuctures,” Phys. Rev. Lett. **61**, 2546 (1988).

[106] PicoHarp 300 user manual

[107] Ch. B. Walsh and E. I. Franses, “Ultrathin PMMA films spin-coated from toluene solutions,” Thin Solid Films, **429**, 71 (2003).

[108] W. Lukosz and R. E. Kunz, “Light emission by magnetic and electric dipoles close to a plane interface. I. Total radiated power,” J. Opt. Soc. Am. **67**, 1607 (1977).

[109] W. Lukosz and R. E. Kunz, “Fluorescence lifetime of magnetic and electric dipoles near a dielectric interface,” Opt. Commun. **20**, 195 (1977).

[110] R. Brown. A brief account of microscopical observations made in the months of June, July and August, 1827, on the particles containded in the pollen of plants; and on the general existence of active molecules in organic and inorganic bodies. Phil. Mag., 4:161, (1828).

[111] A. Einstein, “Investigations on the theory of the Brownian movement,” R. Fourth, Ed., A. D. Cowper, Transl. Methuen, London, 63-67, (1926).

[112] Jean Perrin, "Mouvement brownien et réalité moléculaire," Annales de Chimie et de Physique, 8^{e} Série **18**: 1–114 (1909). Extract in English, translation by Frederick Soddy.

[113] J. C. Maxwell, “A treatise on electricity and magnetism,” 1st ed., 2:391, Oxford, (1873).

[114] A. Ashkin. “Acceleration and trapping of particles by radiation pressure,” Phys. Rev. Lett. 24:156, (1970).

[115] A. Ashkin, J. M. Dziedzic, J. E. Bjorkholm and S. Chu, "Observation of a single-beam gradient force optical trap for dielectric particles," Opt. Lett. 11, 288–290, (1986).

[116] A. Ashkin. “Trapping of atoms by resonance radiation pressure,” Phys. Rev. Lett. 40:729, (1978).

[117] D. J. Wineland, R. E. Drullinger, and F. L. Walls. “Radiation-pressure cooling of bound resonant absorbers,” Phys. Rev. Lett. 40, 1639, (1978).

[118] A. Ashkin, J. M. Dziedzic "Optical trapping and manipulation of viruses and bacteria," Science 235 (4795), 1517–1520, (1987).

[119] C. Bouchiat, M. D. Wang, J. Allemand, T. Strick, S. M. Block, and V. Croquette. “Estimating the persistence length of a worm-like chain molecule from force-extension measurements,” Biophys J. 76, 409, (1999).

[120] M. D. Wang, H. Yin, R. Landick, J. Gelles, and S. M. Block, “Stretching dna with optical tweezers,” Biophys J. 72(3), 1335–46, (1997).

[121] A. Ashkin, J. M. Dziedzic, and T. Yamane. “Optical trapping and manipulation of single cells using infrared laser beams,” Nature, 330(6150), 769–771, (1987).

[122] J. W. J. Kerssemakers, M. E. Janson, A. van der Horst, and M. Dogterom. “Optical trap measuring microtubule pushing forces,” Applied Physics Letters, 83(21), 4441–4443, (2003).

[123] Y. Harada and T. Asakura, “Radiation forces on a dielectric sphere in the rayleigh scattering regime,” Optics Comm. 124, 529, (1996).

[124] S. Kawata, and T. Sugiura, “Movement of micrometer-sized particles in the evanescent field of a laser beam,” Opt. Lett. 17**,** 772–774 (1992).

[125] C. Girard, A. Dereux, and O. J. F. Martin, “Theoretical analysis of light-inductive forces in scanning probe microscopy,” Phys. Rev. B 49, 13872–13881 (1994).

[126] A. Dereux, C. Girard, O. J. F. Martin and M. Devel, “Optical binding in scanning probe microscopy,” Europhys. Lett. 26**,** 37–42 (1994).

[127] S. Kawata, and T. Tani, “Optically driven Mie particles in an evanescent field along a channelled waveguide,” Opt. Lett. 21**,** 1768–1770 (1996).

[128] L. Novotny, R. X. Bian, and X. S. Xie, “Theory of nanometric optical tweezers,” Phys. Rev. Lett. 79**,** 645–648 (1997).

[129] V. Garcés-Chávez, R. Quidant, P. J. Reece, G. Badenes, L. Torner, and K. Dholakia, “Extended organization of colloidal microparticles by surface plasmon polariton excitation,” Phys. Rev. B 73**,** 085417 (2006).

[130] G. Volpe, R. Quidant, G. Badenes, & D. Petrov, “Surface plasmon radiation forces,” Phys Rev Lett. 96, 238101, (2006).

[131] M. Righini, A. S. Zelenina, C. Girard, and R. Quidant, “Parallel and selective trapping in a patterned plasmonic landscape,” Nature Phys. **3,** 477–480, (2007).

[132] M. Righini, G. Volpe, C. Girard, D. Petrov, and R. Quidant, “Surface plasmon optical tweezers: tunable optical manipulation in the femtonewton range,” Phys. Rev. Lett. 100**,** 183604, (2008).

[133] A. N. Grigorenko, N. W. Roberts, M. R. Dickinson, and Y. Zhang, “Nanometric optical tweezers based on nanostructured substrates,” Nature Photon. 2**,** 365–370 (2008).

[134] A. E. Wallin, H. Ojala, E. Hæggström, & R. Tuma, “Stiffer optical tweezers through real-time feedback control,” Appl. Phys. Lett. 92**,** 224104 (2008).

[135] R. M. Simmons, J. T. Finer, S. Chu, and J. A. Spudich, “Quantitative measurements of force and displacement using an optical trap,” Biophys. J. 70**,** 1813–1822 (1996).

[136] A. Ashkin, and J. M. Dziedzic, “Feedback stabilization of optically levitated particles,” Appl. Phys. Lett. **30,** 202–204 (1977).

[137] W. Zhang, L. Huang, C. Santschi, and O. J. F. Martin, “Trapping and sensing 10 nm metal nanoparticles using plasmonic dipole antennas,” Nano Lett. 10**,** 1006–1011 (2010).

[138] N. A. Issa, and R. Guckenberger, “Optical nanofocusing on tapered metallic

Waveguides,” Plasmonics 2**,** 31–37 (2007).

[139] D. K., Gramotnev, M. W. Vogel, and M. I. Stockman, “Optimized nonadiabatic nanofocusing of plasmons by tapered metal rods,” J. Appl. Phys. 104**,** 034311 (2008).

[140] M. Durach, A. Rusina, M. I. Stockman, and K. Nelson, “Toward full spatiotemporal control on the nanoscale,” Nano Lett. 7**,** 3145–3149 (2007).

[141] K. Kurihara, K. Yamamoto, J. Takahara, and A. Otomo, “Superfocusing modes of surface plasmon polaritons in a wedge-shaped geometry obtained by quasiseparation of variables,” J. Phys. A 41**,** 295401–295500 (2008).

[142] D. F. P. Pile, and D. K. Gramotnev, “Adiabatic and nonadiabatic nanofocusing of plasmons by tapered gap plasmon waveguides,” Appl. Phys. Lett. 89, 041111 (2006).

[143] Corning SMF-28 optical fiber product information

BIOGRAPHICAL INFORMATION

Lei Zhu was born in Anshan, Liaoning Province, China. He completed the high school education from Anshan No. 1 senior middle school in 2000. In 2004, he received Bachelor of Science degree in Physics from Dalian University of Technology. Then he joined the graduate school and obtained Master of Science degree in Physics from Dalian University of Technology in 2007. In the same year, he entered graduate school in University of Texas at Arlington. In 2008, he joined Prof. Michael Vasilyev's group in Electrical Engineer in 2008.

During the Ph.D. program, he finished three projects: Shaping spontaneous emission pattern by plasmonic nanocavity, Spontaneous emission lifetimes of CdSe / ZnS core-shell quantum dots at air-material interface and Single-mode fiber-based plasmonic optical tweezers.

His research interests are surface plasmonic, silicon photonics, quantum optics and optical tweezers. In the future, he would like to become a researcher in optics field. He believes that optics will never die.